



A numerical analysis of the hydrodynamic mixing characteristics of a rectangular versus a cylindrical mixing crystallizer tank for a membrane distillation apparatus

by

Everhardus Johannes Smith

Dissertation submitted in fulfilment of the requirements for the degree

Master of Technology: Mechanical Engineering

in the Faculty of Engineering

at the Cape Peninsula University of Technology

**Supervisor:** Prof G. Oliver (Cape Peninsula University of Technology)

**Co-supervisor:** J. Nathoo (NuWater Global)

Bellville

October 2018

CPUT copyright information

The dissertation may not be published either in part (in scholarly, scientific or technical journals), or as a whole (as a monograph), unless permission has been obtained from the University

## DECLARATION

I, Everhardus Johannes Smith, declare that the contents of this dissertation represent my own unaided work, and that the dissertation has not previously been submitted for academic examination towards any qualification. Furthermore, it represents my own opinions and not necessarily those of the Cape Peninsula University of Technology or NuWater.

---

---

## ABSTRACT

A membrane distillation crystallization (MDC) experimental setup was designed, constructed and commissioned with rectangular mixing crystallizer tanks. The advantages and disadvantages of a rectangular mixing tank are compared to the traditional cylindrical mixing tank with baffling by means of a computational fluid dynamic (CFD) analysis in Ansys Fluent.

The effect of tank configuration and geometry on the hydrodynamic and mixing characteristics for efficient momentum, solid suspension, heat and mass transfer were investigated. The hydrodynamic conditions in a crystallizer-mixing tank determine the quality of fluid mixing essential for optimal crystallization. Forty-five degree pitched blade turbines (PBT) were used to provide the agitation in the stainless steel rectangular jacketed tanks.

Clear polycarbonate replicas of the rectangular tanks were manufactured to visually observe the mixing process in the tanks. Silica particles were used to represent the calcium carbonate crystals in the experiment. The data gathered from these experiments showed that the tanks should be operated between 600 to 750 rpm in the CFD simulations to simulate partial to complete suspension.

In the numerical simulations a rectangular tank was compared to a cylindrical tank with baffling of the same volume. The partial differential equations solved in the numerical simulation were the conservation of mass (continuity), conservation of momentum and additional turbulence equations. In order to solve the turbulent fluid flow characteristics, the industry standard two-equation model, namely the K-epsilon model was used. This model was refined by the addition of the Wen-Yu drag model, the Simonin turbulent dissipation and the Simonin et al. turbulence interaction models. The RANS based RNG ( $k-\epsilon$ ), derived from the instantaneous Navier-Stokes equation was selected as the preferred model to analyse the hydrodynamic flow fields in the tanks. The 3D sliding mesh method was used to compute a time accurate solution.

The Eulerian-granular multiphase model was used to predict the degree of solids suspension in the tanks. The efficiency of mixing within the tank was measured by the tank's ability to keep the crystals in suspension and preventing any particle from settling at the bottom for more than 1-2 second(s). The mixing tanks were initially loaded with 5% v/v, which equates to a loaded height of approximately 10 mm. The simulations were done with the use of the volume fraction function to visually observe the cloud height and gauge the homogeneity and distribution of the particulates within the fluid flow fields.

The results from the experimental setup were compared to the CFD simulations to qualify the use of CFD simulations for the comparison of the geometrically different tanks. Lastly, the findings from the CFD simulations were used to compare the tanks and determine if the rectangular tank built for the MDC experiment perform satisfactorily to replace a standard cylindrical tank with baffling for this application.

Based on the results of this study, the following conclusions could be drawn:

- I. The rectangular tank was less expensive and simpler to manufacture, compared to a cylindrical tank with baffling.
- II. The hydrodynamic mixing characteristics in the rectangular tank were comparable to the mixing characteristics in the traditional cylindrical tank.
- III. Excessive horizontal velocities have a negative impact on the mixing characteristics because they initiate rotational swirl and subsequently vortexing, reducing the efficiency of particle suspension.
- IV. The rectangular tank's corners are not as effective as baffling in preventing rotational swirl.
- V. The upward axial velocity needs to be sufficient in the horizontal cross-sectional plane to keep the solids in suspension.
- VI. The cylindrical tank showed superior solid suspension and overall homogeneity at lower rotational velocities.
- VII. The flat bottoms of the tanks adversely affected the solid suspension. Weak flows were seen in the bottom corners.
- VIII. The CFD analysis correctly predicted the off-bottom solid suspension and cloud height suspension of the rectangular tank, based on what was observed in experiments.

## **ACKNOWLEDGEMENT**

I would like to thank all people involved in the writing of this dissertation. First, I would like to thank J. Nathoo who motivated me to write this dissertation and who also agreed to be the co-supervisor.

Professor G. Oliver who agreed to supervise this dissertation at the Cape Peninsula University of Technology and for not losing confidence during the quiet times when not much progress was being made due to other responsibilities.

The Water Research Commission of South Africa for providing the funding for the construction of the experimental DCMD apparatus and making this research a reality.

NuWater Global for using their resources in the construction of the experimental equipment and for the personnel whom without, it would have been a great deal harder. A special thank you to J. Hendricks, JP Lombard and C. Watkins, who were always willing to assist.

To E. Jelsma at Flow Motion for guiding me in the setup of the Ansys Fluent models for this specific application. Without his expert guidance, the CFD setup would have taken considerably longer.

To my family, in particular, my parents for their support during my initial studies. Lastly, I would like to thank my wife Lianda for all her emotional support for the duration of this dissertation.

## TABLE OF CONTENTS

<b>CHAPTER 1: Introduction &amp; Background</b> .....	<b>2</b>
<b>1.1 Background</b> .....	<b>2</b>
1.1.1 Brine handling methods.....	2
1.1.2 Membrane distillation crystallisation (MDC) .....	3
<b>1.2 Overall aims and objectives</b> .....	<b>8</b>
<b>CHAPTER 2: Literature review</b> .....	<b>9</b>
<b>2.1 Multiphase turbulence modelling</b> .....	<b>9</b>
<b>2.2 Solid suspension</b> .....	<b>16</b>
<b>2.3 Tank configuration and geometry</b> .....	<b>22</b>
<b>CHAPTER 3: Membrane Distillation Experiment</b> .....	<b>25</b>
<b>3.1 Process design</b> .....	<b>25</b>
<b>3.2 Control philosophy</b> .....	<b>26</b>
<b>3.3 Process equipment &amp; instrumentation</b> .....	<b>26</b>
<b>3.4 Manufacturing of equipment</b> .....	<b>27</b>
3.4.1 Jacketed tanks.....	29
3.4.2 Impeller.....	30
3.4.3 Frame.....	31
3.4.4 Membrane holder .....	31
3.4.5 Electrical installation .....	31
<b>3.5 Commissioning of experimental equipment</b> .....	<b>33</b>
3.5.1 Electrical check.....	33
3.5.2 Mechanical check .....	34
3.5.3 Functionality check .....	34
<b>CHAPTER 4: Solid suspension experiment</b> .....	<b>35</b>
<b>4.1 Construction</b> .....	<b>35</b>
<b>4.2 Experimental results</b> .....	<b>36</b>
4.2.1 Experiment - 600 RPM .....	36
4.2.2 Experiment – 750 RPM.....	36
<b>CHAPTER 5: Numerical simulation</b> .....	<b>38</b>
<b>5.1 Computational fluid dynamics</b> .....	<b>38</b>
5.1.1 Fluent governing equations.....	39
<b>5.2 Geometry</b> .....	<b>44</b>

5.2.1	Dimensions.....	44
5.2.2	Named selections .....	46
<b>5.3</b>	<b>Meshing.....</b>	<b>47</b>
5.3.1	Meshing quality.....	47
5.3.2	Effect of cell size.....	50
<b>5.4</b>	<b>Fluent model setup.....</b>	<b>54</b>
5.4.1	General.....	54
5.4.2	Models.....	54
5.4.3	Materials and phases.....	54
5.4.4	Cell Zone Conditions .....	55
5.4.5	Boundary Conditions .....	55
5.4.6	Interface .....	55
5.4.7	Solution initialization .....	55
5.4.8	Solution methods and the calculation .....	56
<b>CHAPTER 6:</b>	<b>Results and discussions .....</b>	<b>58</b>
<b>6.1</b>	<b>CFD vs experimental results.....</b>	<b>58</b>
6.1.1	Simulations 600 RPM .....	58
6.1.2	Simulation 750 RPM.....	64
6.1.3	Experimental findings .....	66
<b>6.2</b>	<b>CFD comparison of the rectangular vs round mixing tank.....</b>	<b>67</b>
6.2.1	Mean velocity.....	67
6.2.2	Axial velocity.....	68
6.2.3	Radial velocity .....	70
6.2.4	Tangential velocity .....	71
6.2.5	Velocity vectors .....	71
<b>6.3</b>	<b>Contours of turbulence .....</b>	<b>74</b>
6.3.1	Turbulent kinetic energy (K).....	74
6.3.2	Turbulent energy dissipation rate ( $\epsilon$ ).....	74
6.3.3	Turbulent viscosity (eddy viscosity).....	75
<b>6.4</b>	<b>Solids suspension.....</b>	<b>76</b>
6.4.1	Solids distribution volume render .....	77
<b>CHAPTER 7:</b>	<b>Conclusion.....</b>	<b>79</b>
<b>7.1</b>	<b>Flow fields.....</b>	<b>79</b>
<b>7.2</b>	<b>Off-bottom suspension and cloud height .....</b>	<b>80</b>
7.2.1	Experimental results .....	80
7.2.2	CFD results .....	80

<b>7.3 Overall performance</b> .....	<b>81</b>
7.3.1 Advantages of a rectangular mixing tank .....	81
7.3.2 Disadvantages of a rectangular mixing tank .....	81
<b>CHAPTER 8: Recommendations</b> .....	<b>82</b>
<b>CHAPTER 9: References</b> .....	<b>83</b>
<b>APPENDIX A - PLC selection</b>	
<b>APPENDIX B – Manufacturing drawings</b>	
<b>APPENDIX C – Experimental data</b>	



## LIST OF FIGURES

Figure 1: MD distillation setups. (Onsekizoglu, 2012).....	4
Figure 2: Local volume fraction (Cokljat et al., 2006) .....	10
Figure 3: Tetrahedral meshes of model (Vakili et al., 2008) .....	11
Figure 4: Flow field of 390 micron particles (Bakker et al., 2002) .....	17
Figure 5: CFD meshes for impeller setups (Gohel et al., 2012).....	19
Figure 6: Velocity vectors of systems 200RPM (Gohel et al., 2012) .....	20
Figure 7: Solids suspension of systems 200RPM (Gohel et al., 2012) .....	20
Figure 8: Effect of TDF on solid suspension (Gohel et al., 2012) .....	21
Figure 9: DCMD Piping and instrumentation diagram (Smith, 2015) .....	25
Figure 10: CAD model of experimental rig .....	28
Figure 11: Photograph of the experimental rig (Nathoo, 2015).....	29
Figure 12: Rectangular jacketed tanks (Smith, 2014).....	30
Figure 13: Pitched blade turbine (Smith, 2014) .....	30
Figure 14: Stainless steel Frame (Smith, 2014) .....	31
Figure 15: Electrical cabinet and VSD's (Smith, 2014) .....	32
Figure 16: Experimental setup (Smith, 2018) .....	35
Figure 17: Vortex and flow field at 600RPM, 15s (Smith, 2018) .....	36
Figure 18: Vortex and flow field at 750RPM, 15s (Smith, 2018) .....	37
Figure 19: Cylindrical mixing tank with baffles.....	45
Figure 20: Rectangular mixing tank without baffles .....	45
Figure 21: Rectangular mixing tank named selections .....	46
Figure 22: Rectangular tank mesh quality .....	49
Figure 23: Cylindrical tank mesh quality.....	49
Figure 24: Meshing (Section view, XY=0) .....	50
Figure 25: Meshing inflation (Section view, XY=0) .....	50
Figure 26: Rectangular tank refined mesh .....	51
Figure 27: Rectangular tank actual mesh.....	51
Figure 28: Cylindrical tank refined mesh .....	51
Figure 29: Cylindrical tank actual mesh .....	51
Figure 30: Rectangular tank mean vel. refined.....	52
Figure 31: Rectangular tank mean vel. actual .....	52
Figure 32: Rectangular tank turbulent kinetic energy refined.....	52
Figure 33: Rectangular tank turbulent kinetic energy actual.....	52
Figure 34: Cylindrical tank mean vel. refined .....	52
Figure 35: Cylindrical tank mean vel. actual.....	52
Figure 36: Cylindrical tank turbulent kinetic energy refined .....	53
Figure 37: Cylindrical tank turbulent kinetic energy actual.....	53
Figure 38: Solids loading (Section, XY=0).....	56
Figure 39: Experiment - 0s.....	58
Figure 40: CFD 600 RPM – 0s.....	58
Figure 41: Experiment - 2s.....	59
Figure 42: CFD 600 RPM – 2s.....	59
Figure 43: Experiment – 4s.....	59
Figure 44: CFD 600 RPM – 4s.....	59
Figure 45: Experiment – 6s.....	59
Figure 46: CFD 600 RPM – 6s.....	59
Figure 47: Experiment – 8s.....	60
Figure 48: CFD 600 RPM – 8s.....	60
Figure 49: Experiment – 10s.....	60
Figure 50: CFD 600 RPM – 10s.....	60
Figure 51: Experiment – 12s.....	60

Figure 52: CFD 600 RPM – 12s.....	60
Figure 53: Experiment – 15s.....	61
Figure 54: CFD 600 RPM – 15s.....	61
Figure 55: Experiment vs CFD – 2s.....	61
Figure 56: Experiment vs CFD – 4s.....	61
Figure 57: Experiment vs CFD – 6s.....	62
Figure 58: Experiment vs CFD – 8s.....	62
Figure 59: Experiment vs CFD – 10s.....	62
Figure 60: Experiment vs CFD – 12s.....	62
Figure 61: Experiment vs CFD – 15s.....	62
Figure 62: Experiment - 15s.....	64
Figure 63: CFD 750 RPM – 15s.....	64
Figure 64: Experiment vs CFD – 15s.....	64
Figure 65: Model orientation.....	67
Figure 66: Rectangular mean vel. Z=0.....	68
Figure 67: Cylindrical mean vel. X=0.....	68
Figure 68: Rectangular mean vel. Y=-99.....	68
Figure 69: Rectangular axial vel. Z=0.....	69
Figure 70: Cylindrical axial vel. X=0.....	69
Figure 71: Rectangular axial vel. Y=-70.....	69
Figure 72: Cylindrical axial vel. Y=-70.....	69
Figure 73: Rectangular radial vel. X=0.....	70
Figure 74: Cylindrical radial vel. Z=0.....	70
Figure 75: Rectangular tangential vel. Y=-90.....	71
Figure 76: Cylindrical tangential vel. Y=-90.....	71
Figure 77: Rectangular tank mean vel. vectors.....	72
Figure 78: Cylindrical tank mean velocity vectors.....	72
Figure 79: Rectangular tank mean velocity vectors at walls.....	73
Figure 80: Cylindrical tank mean velocity vectors at walls.....	73
Figure 81: Rectangular turbulent kinetic energy.....	74
Figure 82: Cylindrical turbulent kinetic energy actual.....	74
Figure 83: Rectangular turbulent energy dissipation rate.....	74
Figure 84: Cylindrical turbulent energy dissipation rate.....	74
Figure 85: Rectangular turbulent viscosity.....	75
Figure 86: Cylindrical turbulent viscosity.....	75
Figure 87: Rectangular solid suspension Z=0.....	76
Figure 88: Cylindrical solid suspension X=0.....	76
Figure 89: Solids distribution at 600 RPM Rect. – 5s.....	77
Figure 90: Solids distribution at 600 RPM Cyl. - 5s.....	78

## LIST OF EQUATIONS

(Equation 1: Water Recovery) .....	2
(Equation 2: Permeate Flux) .....	5
(Equation 3: Reynolds number) .....	6
(Equation 4: Impeller power input) .....	12
(Equation 5: Length scale of eddy currents (Brucato et al. 1998) .....	12
(Equation 6: Zwietering off bottom) .....	18
(Equation 7: Settling velocity).....	23
(Equation 8: Settling power).....	23
(Equation 9: Shaft power) .....	32
(Equation 10: Angular velocity) .....	32
(Equation 11: Torque on the shaft).....	32
(Equation 12: RNG-k) .....	40
(Equation 13: RNG- $\epsilon$ ).....	40
(Equation 14: Eulerian granular phase continuity equation) .....	40
(Equation 15: Eulerian granular phase momentum equation).....	41
(Equation 16: Turbulent kinetic energy) .....	42
(Equation 17: Kinetic energy dissipation rate) .....	42
(Equation 18: Wen-Yu drag model).....	42
(Equation 19: Gidaspow drag model).....	42
(Equation 20: Syamlal-O'Brien drag model) .....	43

## LIST OF TABLES

Table 1: Electrical inspection sheet.....	33
Table 2: Mesh quality report.....	48
Table 3: Refined mesh quality.....	51
Table 4: Material input .....	54
Table 5: Phase interaction models.....	55
Table 6: Cell zone condition user input .....	55
Table 7: CFD vs experimental results (600 RPM) .....	63
Table 8: CFD vs experimental results (750 RPM) .....	65
Table 9: Axial velocities .....	69
Table 10: Axial velocities .....	70
Table 11: Solid suspension.....	76

## LIST OF GRAPHS

Graph 1: CFD vs experimental results (600 rpm) .....	63
Graph 2: CFD vs experimental results (750 rpm) .....	65

## NOMENCLATURE

B	Height of impeller blade
$b_w$	Baffle width
D	Impeller diameter
$d_p$	Average particle diameter
g	Gravity
H	Tank height/Liquid height
$K_{st}$	Solid-liquid exchange coefficient
N	Impeller speed
$N_{js}$	Zwietering just suspension speed
P/V	Energy dissipation rate
Re	Reynolds number
S	Zwietering's geometric constant
T	Tank diameter
X	Mass ratio of solids to liquid
$\alpha_s$	Volume fraction of solids
$\alpha_l$	Volume fraction of liquid
$\epsilon$	Turbulent energy dissipation
$d_s$	Particle diameter
k	Turbulent kinetic energy
$\mu$	Dynamic viscosity
$\mu_t$	Turbulent viscosity
$\nu$	Kinematic viscosity
$\rho_s$	Density of solids
$\rho_l$	Density of liquid
$\omega$	Specific dissipation

## CHAPTER 1: Introduction & Background

### 1.1 Background

The mining industry is expanding rapidly across Africa while drinking water shortages are on the rise. It is well known that mines have excessive wastewater, which is usually pumped into evaporation ponds or natural fresh water sources. This wastewater is usually contaminated and unfit for human consumption. The wastewater directly- and indirectly contaminates natural fresh water sources. Consequently, this wastewater cannot simply be disposed of and alternative treatment methods are necessary to treat these wastewaters. (Morillo et al. 2014)

Water treatment methods are not new to the mining industry. Today, reverse osmosis (RO) is the world leading technology for desalination installations. RO is an isothermal process where hydrostatic pressure is applied to the solution through a semi-permeable membrane to desalinate it. (Morillo et al. 2014)

RO is commonly used for the desalination of wastewater from mining and mineral processing operations as a means of recovering water for reuse or discharge into the environment within the acceptable water quality limits. Typically, the rejection of ionic species within an RO system ranges between 95 – 99.5% making it an effective method for water treatment.

However, membrane water treatment processes have a fundamental flaw, which is the production of a hypersaline concentrate stream, namely, brine. The water recovery of a reverse osmosis process is limited by the solubility of the sparingly soluble species. Overall water recovery is typically around 70 - 75%, depending on the salinity of the feed solution. The remaining 25 - 30% constitutes the brine, which needs to be processed further to recover the remaining water and dispose of the hyper-concentrated brine (DOW et al. 2008). The following equation is used to calculate the water recovery of a membrane or any other water treatment process.

$$\text{Recovery} = \frac{\text{Product Water Quantity}}{\text{Feed Water Quantity}} \times 100$$

#### (Equation 1: Water Recovery)

There is an increasing need for sustainable post treatment processes (brine handling). The brine treatment cost increases almost exponentially as higher water recoveries are required, towards ultimately achieving zero liquid discharge (ZLD). The complex chemistry of these hypersaline brines further complicates the brine treatment process. There are two main brine handling methods currently being used.

#### 1.1.1 Brine handling methods

The first, which has been commonly used due to its lower overall operating cost, is disposal of brine into solar evaporation ponds. However, this method of brine disposal is becoming increasingly unacceptable because it is only an interim solution. It merely delays the treatment of the brine to a later stage in the future. While the brine concentrates increase in the evaporation ponds, it retains the exposure to risk associated with the pond overflowing to groundwater contamination in the event of liner leaks. (Morillo et al. 2014:33)

The second method is the recovery of water through forced evaporation. Examples of such systems are multi-stage flash (MSF) and mechanical vapour compression (MVR). These systems are capital and energy expensive. In addition, although they achieve a higher overall water recovery, they generally produce mixed salt waste that commonly needs to be disposed of in a landfill. (Nathoo, J. 2014)

Novel brine treatment processes such as eutectic freeze crystallisation (EFC) are also being investigated for this application. The process involves cooling the brine down to the freezing point of the various solids (ice and salts). The separation between the ice and salt is achieved based on the fact that ice floats, while the salt sinks to the bottom. (Nathoo, J. 2014)

EFC offers a major energy saving when compared to evaporative crystallisation due to the heat of vaporisation (2260 kJ/kg) being roughly seven times greater than the heat of fusion (334 kJ/kg), however, there is still considerable room for optimisation and innovation in developing more elegant brine treatment solutions. (EFC separations 2012)

Considering the brine treatment processes with disadvantages ranging from environmental impact, energy efficiency and high costs involved there is a necessity for alternative brine treatment solutions.

### **1.1.2 Membrane distillation crystallisation (MDC)**

Membrane distillation is an emerging brine treatment method that provides higher energy savings. Unlike other processes, the driving force is not the mechanically applied force but the difference in temperature of the solution on either side of the membrane, which creates a vapour pressure differential. Water vapour pressure is not significantly influenced by higher salt concentrations, which makes MD attractive as a brine treatment method. MD is not as sensitive to varying feed water compositions, which means that the pre-treatment can be significantly reduced and still produce a high-quality product. MD was first developed in the 1960's but was not actively pursued due to its perceived poor performance due to non-optimal operating conditions and membrane availability at the time. Fresh water scarcity in recent times is forcing manufacturers to reconsider MD as an alternative source for brine treatments. (Dow et al. 2008)

MDC relies on two key factors for the successful treatment of brines:

- I. The membrane separation process.
- II. The crystallisation process in the mixing crystallizer tanks.

#### **1.1.2.1 Membrane separation**

Understanding and controlling the crystallisation characteristics of brines is critical in the successful operation of an MDC process due to the potential negative effect of membrane scaling/fouling. In addition to this, the salt yield, purity, and particle characteristics are determined by the crystallisation conditions within the MDC process. (Dow et al. 2008)

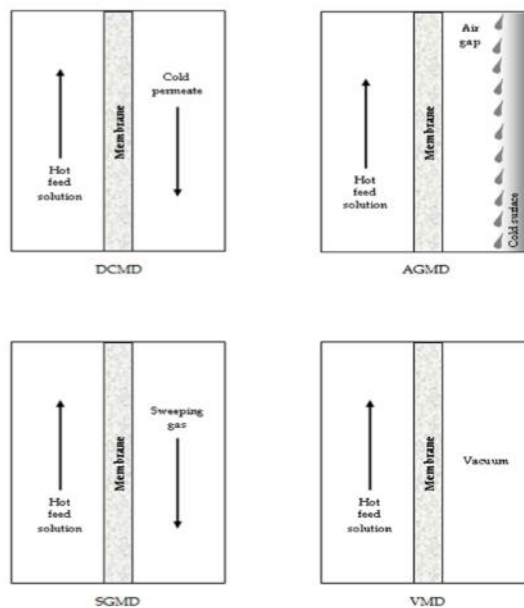
Hydrophobic membranes are typically used for MD, the hydrophobic membrane only allows water vapour to pass through, whereas RO membranes are hydrophilic to promote higher water fluxes at lower operating pressures. MD is a process whereby the temperature is used as the driving force to separate the salts, unlike RO where hydrostatic pressure is driving force to overcome the osmotic pressure of the water. (Dow et al. 2008)

In the MD process, two parallel streams (one heated and the other chilled) are pumped separately along membrane surface on both sides, resulting in a temperature differential through the hydrophobic membrane. The temperature difference creates the vapour pressure differential. The difference in vapour pressure is the force that drives the process. The heated stream of the process has a high vapour pressure, and the chilled stream has a lower vapour pressure. The water vapour molecules travel from the high-pressure stream to the low-pressure stream to achieve vapour equilibrium. (Onsekizoglu 2012)



There are many configurations for MD, the most common types of membrane distillation processes are described below:

- Direct contact membrane distillation (DCMD): The fluid is in direct contact with the membrane on both sides of the membrane. (Dow et al. 2008)
- Air gap membrane distillation (AGMD): The feed water is in contact with the membrane, the coolant is on the outside of a condensation plate, and the permeate is collected in between. (Dow et al. 2008)
- Sweeping gas membrane distillation (SGMD): It is similar to AGMD however, instead of air, an inert gas is being utilised. (Dow et al. 2008)
- Vacuum membrane distillation (VMD): Vacuum pumps are utilized on the permeate side of the membrane. (Dow et al. 2008)



**Figure 1: MD distillation setups.** (Onsekizoglu, 2012).

The advantages of MD in comparison to other membrane processes are mentioned below.

- Lower operating pressures can be achieved. Temperatures lower than the boiling point of the feed solution can still result in reasonably high permeate fluxes. (Sarti et al. 1985)
- a Lower vapour space is required since the vapour-liquid interface is reduced by the addition of the hydrophobic membrane to the process. In conventional distillation, much higher energy input is required to achieve the high vapour velocities required to generate the vapour liquid interface. (Jonsson et al. 1985)
- Traditionally weaker materials can be used for the construction of the setup, since MD requires less energy. This renders the process more economical.
- High osmotic pressure and fouling do not influence the MD process as much as in other membrane processes, since it is operated at atmospheric pressure and the hydrophobic membrane is only supporting the process and is not directly separating the species. (Hsu et al. 2002). Subsequently, the interaction between the membrane and process cleaning chemicals can be reduced. With the reduced chemical interaction, the options of chemical resistant membrane polymers that can be used, are vastly expanded.
- MD separation of ions, suspended solids, cells and other non-volatile solutes are comparable to the separation abilities of UF, NF and RO processes. (Diaz & Diaz 2001)

- Feed water concentration changes does not affect MD as much as other membrane separation processes and thus, have the ability to concentrate aqueous water solutions for crystallisation and or produce high-quality permeate. (Kubota et al. 1988)

The majority of MD setups use microporous hydrophobic membranes, which are normally used for microfiltration (MF). It is commercially available in flat sheets or in capillary form. The most common materials for manufacturing MD membranes are polypropylene (PP), polyvinylidene fluoride (PVDF) and polytetrafluoroethylene (PTFE). (Mahdi et al. 2012)

The essential characteristics of a high quality MD membrane:

- High hydrophobicity
- High micro porosity
- High liquid entry pressure
- Low thickness
- Low tortuosity
- low thermal conductivity
- High fouling resistance
- High thermal, mechanical and chemical stability
- Low surface energy with the process liquid.
- Many believe PTFE as the best-suited material for the MD process. (Mahdi et al. 2012)

The challenges to membrane distillation being used extensively include:

- The development of advanced MD membranes to prevent membrane pore wetting
- Increasing permeate flux rates
- Reducing the energy consumption
- Eliminating inefficient flow distribution
- Poor hydrodynamics
- Severe temperature polarisation (TP). (Yang et al. 2012)

Permeate flux is calculated by the equation shown below:

$$J_p = \frac{\Delta V}{A\Delta t}$$

**(Equation 2: Permeate Flux)**

Where  $\Delta V$  is the volume of permeate (L),  $A$  is the effective membrane area ( $m^2$ ) and  $\Delta t$  is the sampling time (h).

Poor hydrodynamic conditions attribute to severe temperature-polarization. TP is believed to be one of the main factors that affect permeate flux rates, as it results in lower actual trans-membrane temperatures and subsequently, lower vapour pressure and a loss in driving force. For DCMD, where the heated and cooled solutions are in direct contact with the membrane, conductive heat loss is at its highest through the membrane matrix resulting in a lower thermal efficiency, which conceivably hampered its commercialization. Thus, there are two significant challenges for the application of MD on an industrial scale, namely the availability of high-flux membranes and modules with improved hydrodynamics tailor-made for MD processes. (Yang et al. 2012)

Reynolds number can be used to characterise the fluid flow state and is represented by the following equation:

$$Re = \frac{\rho VL}{\mu}$$

**(Equation 3: Reynolds number)**

Where  $\rho$  is density ( $\text{kg/m}^3$ );  $V$  velocity (m/s);  $L$  characteristic linear dimension (m); and  $\mu$  is the dynamic viscosity ( $\text{kg/m.s}$ ) of the fluid.

By increasing the Reynolds numbers of the feed solutions, the mass transfer coefficient in the interface membrane-solution improves. It has been noted by Boubakkri et al. that by increasing the Reynolds number leads to a larger trans-membrane temperature difference. The mechanism for this is likely to be the reduction in the resistance of the transfer, which makes the temperature at the surface closer to the bulk stream leading to an increased trans-membrane temperature difference and reducing the concentration polarization effect. The larger temperature differential increases the driving force and consequently enhances the flux. (Boubakkri et al. 2014)

### 1.1.2.2 Mixing crystallizer tanks

Membranes only allow water vapour molecules to pass through the semi-permeable membrane, the feed solution is being deprived of water molecules resulting in the feed solution becoming supersaturated. In order to reduce the supersaturation in the feed solution, well-designed crystallizer tanks are of great importance to reduce the mineral salt concentration in the process. (Samant et al. 2006)

Supersaturation plays a pivotal role in the crystallisation process, thus mixing tank configuration is of vital importance for mixing processes. It affects the uniformity of the flow field, which in turn affects the distribution of supersaturation. Localised supersaturation affects the crystallisation process and ultimately the particle characteristics, which may result in irregular crystal growth. (Samant et al. 2006)

Vortex formation is a drawback in round tanks, which are prone to swirling and is unwanted for uniform flow distribution. To obstruct vortex formation, baffles are usually installed. The addition of baffles in cylindrical tanks makes them more expensive to manufacture. Secondly, the baffles dissipate the energy provided by the PBT, resulting in a higher energy input requirement. Inlet configurations are important for mixing tanks. When designing a mixing tank the following inlet configurations should be avoided:

- Tangential inlets: it induces rotating swirl to the tank.
- Near to wall inlets: it restricts the inlet jet that provides additional mixing and disrupts the flow field negatively, increasing mixing time.
- Deflectors: it obstructs the inlet jet, preventing it from full development.
- Large inlet diameters: It results in a low momentum of the inlet jet, further increasing mixing time. (Shah et al. 2009)

In rectangular mixing tanks, the corners act as baffling to promote upward flow. The corners hamper rotating swirl, and since baffles are not necessarily required in rectangular tanks, the energy input requirement could be less. (Myers et al. 2002)

In the experimental setup, rectangular stainless steel mixing crystallizer tanks were selected for simplicity compared to the cylindrical tank with baffling. This dissertation focused on the

difference between the hydrodynamic mixing characteristics within a rectangular mixing tank and a cylindrical mixing tank with baffling, using a CFD comparison. It also includes the manufacturing of the experimental rig and noting the advantages and disadvantages of the respective geometries.

## 1.2 Overall aims and objectives

The objective of this dissertation was to investigate whether the geometrically simple un-baffled rectangular mixing tank's performance is satisfactory compared to the traditional more complex cylindrical baffled mixing tank for use as a crystallizer tank in MD experiments. A fully functional MD experimental setup with rectangular mixing crystallizer tanks and a down pumping PBT, which provided the agitation, was constructed. The experiment required crystallizer tanks to be designed and custom made for this application with suitable connection port configurations to interconnect with the process equipment. In order to research the suitability of the rectangular tank the following approach was undertaken:

- 1.1.1. To design, construct and commission a membrane distillation crystallisation (MDC) set up for experimentation on brine emanating from a RO process.
- 1.1.2. Numerical analysis: CFD modelling of the agitated crystallizer tanks to predict the hydrodynamic mixing characteristics of a rectangular mixing tank and compare it to a standard cylindrical mixing tank with baffles, and to predict the characteristics in the experimental apparatus.
- 1.1.3. To determine the advantages and disadvantages in terms of design, manufacturing and commissioning of a rectangular tank.

**Chapter 2: Literature review:** a Review of the current state of research performed using CFD tools by other researchers to gain a better understanding of the hydrodynamics and mixing characteristics within the fluid domain. The area of focus was basic mixing tank design, turbulent flow fields, multiphase solids suspension, particle drag, cloud heights and the corresponding CFD setups applicable to the modelling thereof.

**Chapter 3: MD Experiment:** In order to research MDC, an experimental setup was constructed. This chapter explains the process design, construction and commissioning of the experimental setup.

**Chapter 4: Solids suspension Experiment:** Detailed description of the solid suspension experiment.

**Chapter 5: Computational fluid dynamics:** Turbulence is a non-isotropic phenomenon; therefore, it is very difficult to predict the fluid behaviour inside mixing tanks by means of analytical calculations. This chapter consists of the following topics:

- I. The partial differential equations used by Ansys Fluent, along with the various other models of importance to this work.
- II. The advantages and limitations of CFD.
- III. The approach of the geometrical setup of the models, meshing and the setup of Fluent model within Workbench.

**Chapter 6: Results and discussions:** The hydrodynamic mixing characteristics of the simplistic rectangular-mixing tank were compared to the more complex cylindrical tank. The contours of velocity, turbulence, homogeneity of the solution (in terms of volume fraction) and solid suspension were compared.

**Chapter 7: Conclusion:** The key findings of this research project were discussed.

**Chapter 8: Recommendation for future research:** This chapter focuses on recommendations for future improvements to further investigate the performance mixing crystallizers and improve the overall accuracy of the numerical models and simulations.

## CHAPTER 2: Literature review

### 2.1 Multiphase turbulence modelling

Cokljat et al. (2006) published a paper on the Reynolds-Stress model (RSM) for Eulerian multiphase flow. It presented the way of modelling turbulence in multiphase flows within the context of the Reynolds stress model. Two multiphase models were considered namely the mixture and dispersed models. In the mixture model, the Reynolds Stress Transport equations are not solved individually per phase, instead it handles the entire fluid domain as a mixture. In the dispersed model, the Reynolds stress transport equations are solved only for the primary phase, it assumes the secondary (dispersed) phase is transported by the turbulence of the continuous phase. The dispersion is computed by an extension of the dispersion theory of discrete particles by homogenous turbulence. The dispersed model was applied to calculate fully developed aerated flow inside a cylindrical pipe with an inline orifice and the flow in a baffled stirred tank. Lastly, they applied the mixture model to solve the flow-fields in a cyclone to determine if it has industrial relevance.

In the dispersed model, the turbulence in the primary phase is considered to be the dominant process, and it should be utilized when the dispersed (secondary phases) are dilute. Consequently, transport equations for turbulence quantities are only solved for the continuous (primary) phase, while the well-known Tchen-theory is used to predict the quantities of turbulence. The interaction between the primary and the secondary phase turbulence are also taken into account by the equation.

The main assumption of the mixture model is that the primary and secondary phases have the same turbulence fields, thus the Reynolds stress transport equations are basically neglected. The model individual phase properties and velocities are substituted with mixture properties and mixture velocities.

The section significant to this research study is the flow in unbaffled stirred mixing tanks and not constricted flow. It is well known that strong swirling is a concern in tanks without baffling, and mixing performance deteriorates. Recently, Eddy-viscosity models were used to simulate vortexing in fully baffled tanks with reasonable results. Bakker et al. (2001) simulated swirling flow in single-phase mixing tanks and Motante et al (2001) simulated multiphase systems. According to Cokljat (2006), single-phase flow simulations, the  $k-\epsilon$  models are not yet capable of correctly predicting the swirling flow field in unbaffled mixing tanks.

In order to substantiate the research, two scenarios were studied:

- The first was an unbaffled mixing tank, with four radial Rushton turbines providing the agitation.
- In the second case, four axial A310 impellers in the same mixing tank. Previously, Pinelli et al. (2001) published data showing the experimental solids concentration. The CFD results of Cokljat can be seen in **Figure 2** below:

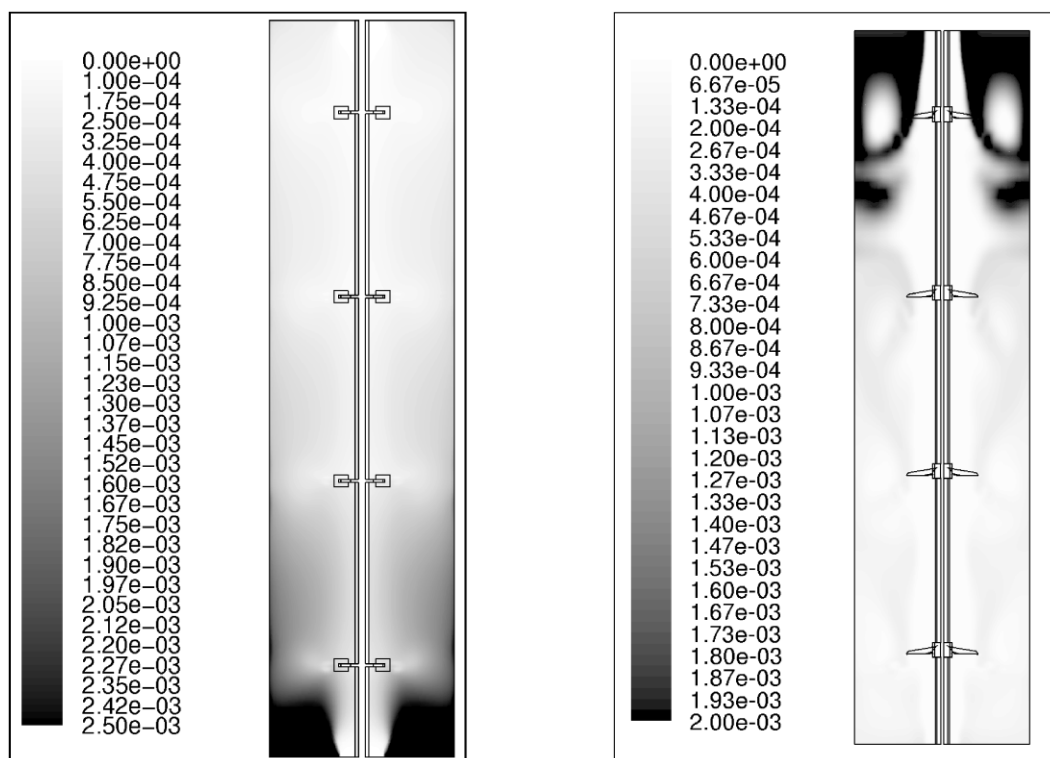


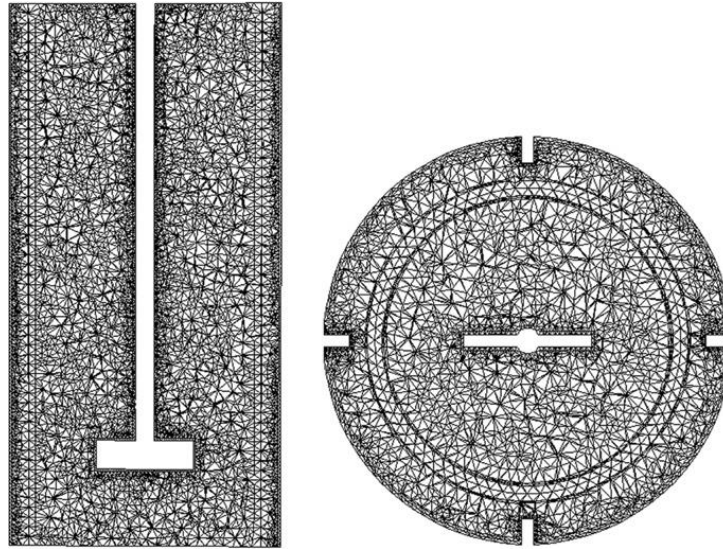
Figure 2: Local volume fraction (Cokljat et al., 2006)

The Rushton turbine was the first to be validated. The impellers had a flat disk with six radially mounted flat plates. The circulation loops were forming above and below the impeller due to the direction of thrust on the radial outflow impeller. The impact of agitation was seen to a minimum extend at the top of the mixing tanks. Subsequently, the segregation between the circulation loops was significant. The average solids concentration loading used in test was  $2 \text{ kg/m}^3$ . In the simulations, the dispersed RSM model was used in combination with the Eulerian granular multiphase model. The second order upwind differencing scheme was used to compute the variables and Schiller-Nuamann drag law was applied. It was also found that the turbulence correction factor to the drag law recommended by Pinelli et al. (2001) could be omitted for this specific case since it had a negligible outcome on the results. The MRF method was used to simulate the rotation of the impeller. One sixth of the mixing configuration using the Rushton turbine was modelled with a consequential mesh of 80 000 hexahedral cells.

The second stirred tank validation involved the same tank, with the difference being the four A310 hydrofoil impellers. Again, the flow was dominated by swirl. However, the swirl was much weaker for the A310 impellers compared to the Rushton turbines, as expected. For the A310 impeller, one third of the mixing configuration was modelled with a mesh of 1.1 million unstructured hexahedral cells. The Schiller-Naumann drag model was also used with the correction factor suggested by Pinelli et al. (2001). It was observed that the solids were eventually transported to the top of the A310 impeller tank system and gets caught in the upper circulation loop. This phenomenon was previously unreported using the RNG  $k-\epsilon$  model. It was further substantiated by the experimental work of Pinelli et al, (2001).

The RNG  $k-\epsilon$  results did not agree satisfactory with the experimental data from Pinelli, providing a growing necessity for new models to be developed. The RSM model was able to accurately predict the solids concentration in the Ruston turbine setup for medium to high slurry density hydrocyclones. According to Cokljat et al (2006) there is no unique model which can accurately predict the effect of turbulence on mass and momentum transfer between phases.

Vakili et al. (2008) studied the turbulence in a stirred, baffled tank using a three-compartment model. This model was used to analyse the non-homogeneity of mixing in fully baffled stirred tank. The (MRF) method was also applied to simulate the impeller rotation. The tank was divided into three respective zones: the region around the impeller, the region at the baffles with a larger non-complex volume between the inner and outer regions named the circulation zone.



**Figure 3: Tetrahedral meshes of model (Vakili et al., 2008)**

The boundaries for these zones were determined using the gradient and cumulative energy dissipation rates respectively. The turbulent kinetic energy dissipation gradient was selected due its simplicity for the simulations. The turbulent kinetic energy showed change with an increase in angular velocity of the impeller in the impeller zone with no remarkable change in the outer baffled zone.

The CFD simulations were conducted in a 0.3 m high and 0.16 m diameter cylindrical tank that was filled with liquid up to a height of 0.28 m. The mixing tank was fitted with four baffles and a standard two-bladed impeller. The baffles were 5 mm thick and 280 mm high to cover the complete height of the tank. Different baffle thicknesses were used to study how the baffle thickness affect the mixing characteristics.

Since the MRF method was selected for the simulations, the tanks had to be divided into two cylindrical sections. A non-uniform grid with tetrahedral elements was selected near the impeller and baffles zones.

The authors used the first order upwind discretization scheme for the convection term of momentum, turbulent kinetic energy, and the energy dissipation rate equations. Relative velocity formulation and the  $k-\epsilon$  turbulence model were used for simulating a tank containing water. The angular velocity of the impeller was set to zero with respect to the rotating coordinate system. According to Vakili et al. the velocity, pressure and turbulence parameters should be estimated for initial calculation. The angular velocity of the rotating reference at the first step of calculations was set to 10% of the case under study. The initial estimations were based on the values after the computation of a 1000 time steps using the time-stepping technique.

According to Vakili et al. energy dissipation rate,  $\epsilon$ , is the most important property to characterise turbulent kinetic energy. Energy dissipation is largely responsible for micro-mixing and it positively affects the rate of heat and mass transfer in reactive systems. On the downside



excessive localised energy dissipation zones could cause damage to the cells and reduce yield in bio-reactors. In the simulations, it was found that the energy dissipation rate of the leading edge of the impeller was approximately double in magnitude compared to the energy dissipation rate in the wake of the blade. The average energy dissipation rate in front of the blade, where the fluid is forced into motion was  $0.127\text{m}^2/\text{s}^3$  and the average value for the back of the blade was around  $0.069\text{m}^2/\text{s}^3$ . The highest energy dissipation rate was seen at the impeller and the baffle regions, the values were much lower for the bulk of the fluid in the intermediate region.

To capture the energy dissipation rate effectively, the mixing tank was also divided into three separate compartments as done by other researchers, however, it was only separated based on the energy dissipation rate. The first was the region around the impeller characterized by high turbulent kinetic energy dissipation rates because of fluid agitation. The second, the region between the impeller and the baffles where the bulk of the fluid is located, and low-energy dissipation rates is expected because of the homogenous nature of the fluid and the surroundings in the region. The last region is the section between the container walls and the inside edge of the baffles where the energy dissipation is less than at the impeller but much larger than in the intermediate zone.

Three scenarios were simulated case 1, 2 and 3 with agitation rates of 100, 400 and 800 rpm respectively. Results showed that doubling the agitation rate from 400 to 800 increases the energy dissipation rates by eight-fold in the impeller region while a six-fold increase was seen in the baffled region. The energy dissipation rate at the impeller region is proportional to  $N^3$ . The impeller power input can be calculated by using the following equation:

$$P = \rho N_p N^3 D^5$$

**(Equation 4: Impeller power input)**

Considering that flow is fully turbulent, power number is constant, and therefore the power input is proportional to  $N^3$ . When the agitation rate was increased the turbulent kinetic energy increased along with it throughout the mixing tank. Turbulent kinetic energy slopes in the baffle and the homogenous zones were similar. At the impeller, where the energy is transferred into the fluid, the turbulent kinetic energy slope is at its greatest and is proportional to the square of linear velocity. By doubling the agitator speed from 400 to 800, turbulent kinetic energy increases by almost four and a half-fold in the impeller region and four-fold in both the baffle and circulation zones.

An increase in turbulent viscosity was seen in all zones as the agitation rate was increased. The turbulent viscosity was found to be highest inside the circulation zone, and that turbulent eddies were the main contributor to scalar transfer. Thus, the turbulent viscosity was higher in the circulation zone than in the other zones. The length of eddies is related to the turbulence properties and can be calculated according to Brucato (1998) with the following equation:

$$L \propto \frac{k^{\frac{2}{3}}}{\varepsilon}$$

**(Equation 5: Length scale of eddy currents (Brucato et al. 1998))**

It was previously stated that the energy dissipation rate increased almost six-fold and the kinetic energy rate increased by four times. Consequently, the length scales of the turbulent eddies were halved. This shows, at an increased agitation rate the length scale of the turbulent eddies are reduced. Smaller values of eddies relate to greater energy dissipation and kinetic energy values.

It was further found that impeller clearance had no significant influence on the turbulent properties within the three respective zones. At the impeller zone both the energy dissipation rate and turbulent kinetic energy showed a considerable increase with impeller diameter. However, no significant effect on these parameters could be observed in the circulation and baffle zones. The highest concentration of turbulent kinetic energy dissipation in the baffle zone occurred on the edges of the baffles. By increasing the baffle widths, the tangential velocity was slowed down due to the tangential inner-baffle edge being in closer proximity to the central axis of the mixing tank and thus reducing the velocity impact, which results in a reduced energy dissipation rate in the baffle zone. The baffle width also had a negative impact on the size of the “dead zone”. The wider baffles further reduced the velocity magnitude at the tank wall resulting in a decrease of turbulent kinetic energy in the homogenous and baffled zones.

Ibrahim et al. researched Zwietering’s equation for the suspension of porous particles and the use of curved blade impellers in 2002. They specifically focussed on the minimum just suspended speed ( $N_{js}$ ) of porous palm shell-activated carbon (PSAC) particles in a cylindrical tank using a six curved blade (CB) impeller compared it to a six bladed down pumping mixed-flow (MFD) impeller and a Ruston turbine.

Various size particles were used for the experiment with concentrations ranging from zero to five percent by weight. The six curved blade impeller classified as a radial impeller, had a similar performance to the standard six bladed PBT in terms of down pumping and to the mixed-flow turbine in terms of speed and power at "just suspension", and distribution of particles. The six-bladed MFD required 100% to 200% less power input than the radial impellers and achieved greater solids suspension heights. The denser the solids concentration became, all the impellers showed a reduction in power per unit mass required.

The Zwietering’s just suspended formulation was used to calculate the geometric factor  $S$ . The just suspended speed ( $N_{js}$ ) was determined by experimental visualisation. The average size of the particles was known as well as the respective densities of the liquid and solid phases. The solid-liquid mass ratio was prepared precisely for the experiments. The power requirement was calculated by the torque measurement on the motor, the impeller was rotated in air to obtain the starting torque and thereafter in the respective solutions, and from this data, the difference in torque was calculated.

The geometric factor ( $S$ ) data were closely related to the available findings from Zwietering when assuming that the spaces between the particles are filled with water, and as a result, the particle density of the activated carbon needed to be adjusted. Therefore, Zwietering’s equation is effective in predicting the just suspension speed for porous particles, when a minor adjustment is made to the particle density. Ibrahim et al. presented in their research maiden geometric factor values for curve bladed impellers.

It was seen that for solids concentrations below 20%, the mixed-flow 6MFD was far superior in its ability to suspend particles compared to the two radial impellers 6CB and 6DT, with respect to power input the requirement and minimum rotational velocity. Activated carbon, ranging from 1.40 to 2.36 mm in size required significantly amplified mixing to agitate the particles into suspension compared to smaller particles in the 1.00-1.40 mm and 0.75–1.00 mm size range. It should be noted that very little change was observed for particles sizes below 1.40 mm.

According to the summary of CFD status of Ochieng and Lewis (2010) CFD simulation techniques have developed very rapidly in recent years. The most CFD strategies evolves around the following key aspects:

- The boundary conditions

- Meshing size
- Discretization scheme
- Equation solvers
- Turbulence models
- Impeller operating modes

The computational cost and the accuracy of the simulations relies on using the correct turbulence model for the simulations. Very little CFD research are performed on round-bottom tanks and hydrofoil impellers, since many commercial CFD packages have difficulties capturing the more curvature and detail correctly. (Sharma and Shaikh, 2003). The problem was amplified with older CFD packages, which were only capable of generating structured meshes.

Usually, the k- $\epsilon$  model used in the two-fluid formulation context. In this approach, the turbulent flow field and turbulent interaction are solved for both phases. Many researchers for mono-size particles use this method, and therefore, in the standard k- $\epsilon$  model, the suspension of solids are not affected by the particle size distribution range. Shah et al. (2001) used the Eulerian based, dispersed model coupled with six solids phases, however, the distribution of the solids concentration was vague. Ochieng and Lewis (2006) applied a poly-dispersed approach to study solid concentration and particle size distributions for high nickel particles. The high-density solids agglomerated on the bottom surface of the mixing tank, they showed that the PSD in the mixing tank was influenced by the density of the particles, and differed throughout the fluid domain. From their findings, it can be concluded that mono-size particles do not represent reality entirely and will vary from practical applications.

The turbulence models based on the Reynolds Average Navier-Stokes (RANS) equation fall into two categories, namely, eddy-viscosity model and Reynolds stress models (RSM). The two-equation models consist of the following models, available in standard packages. The Renormalization group (RNG) k-  $\epsilon$ , standard k- $\epsilon$ , and the k- $\omega$  models. Additional terms are necessary to account for the interphase momentum transfer in multiphase models. The eddy viscosity models assume a relationship between the Reynolds stress and the Viscous stress when the flow fields are isotropic and operated in the turbulent flow regime. The disadvantage of assuming that the turbulent flow fields are entirely isotropic, inaccurate information is computed in the areas where the flow fields are anisotropic and is therefore considered a fundamental flaw. According to Aubin et al. (2004), a negligible difference between the velocity fields and turbulence exist, and claimed improved results can be obtained from large eddy simulation (LES) modelling approach.

The Brucato drag model includes an important difference in the fact that it takes into consideration free stream turbulence, which is not the case for other drag formulation. The other models were developed for single particles immersed in one-directional fluid flows, with the exception of the Gidaspow model. The Gidaspow model effectively becomes Wen-Yu ( $w/w < 0,2$ ) and Ergun ( $w/w > 0,2$ ) models for low and high solids loading respectively.

Ochieng concluded that CFD models based on the fundamental principles of species transport are better at predicting the flow fields and turbulence than empirical models which are largely system specific. In practical methods some regions such as dead zones are not captured accurately, CFD allows for these zones to be predicted correctly. The review shows that the continuously improving computational technology opened up possibilities to simulate solids concentration distribution, particle trajectory and size distributions. In the past these characteristics were predominantly determined by experimental procedures. The current availability of turbulence model formulation, still proves a major challenge for computing accurate CFD simulation results in numerous studies.

At the 9<sup>th</sup> international conference on CFD, in the minerals and process industries CSIRO, Melbourne Australia, Wadnerkar et al. (2012) presented a research paper on the simulation of solid-liquid flow in stirred tanks with high solids loadings.

A hydrodynamic study was performed at a high solids concentration stirred tank. The Eulerian-Eulerian multiphase modelling approach was used to simulate the solid suspension within the tank. The MRF method was applied to mimic impeller rotation in a fully baffled tank. For the calculations Ansys Fluent was selected as the preferred software package. The simulations were conducted for a concentration of 20% w/w and the impeller speeds were operated at the just suspended condition.

The modified Bructo drag model was included in the simulations to account for the interactions between the solids and liquid phase. When solids were added to the mixture, a substantial reduction in flow number was observed. In the areas closest to the impeller where the solids concentration was the highest the turbulence was dissipated the most. The velocity profiles predicted showed reasonable agreement with the data of Guida et al. (2010).

Poor mixing can be resolved by modifying the tank rather than increasing the impeller speed. Simple modifications such as reducing the distance between the base of the tank and the impeller, selecting the correct impeller type, adapting the impeller width, changing the baffles configuration etc. can already improve mixing quality. Merely increasing the impeller angular velocity increases the power consumption with minor changes in the homogeneity of the mixture. Therefore, changing the design parameters is the preferred option, which remains an open problem for design engineers. (Guida et al. 2010)

Visual observation of cloud height can only be applied to low solid loadings. At higher volume fractions, the solids obstruct the visualisation of the cloud. (Sardeshpande et al. 2009). Other methods like direct sampling affect the withdrawal geometry, configuration and subsequently disrupt the velocities within the flow fields making measurements inaccurate. (Yamazaki et al. 1986)

The applicability of flow field measurement based on optical measurements like light scattering techniques, laser Doppler velocimetry and particle image velocimetry are limited to low concentration due to their inapplicability in high solids loading systems. (Pianko-Oprych et al. 2009; Unadkat et al. 2009). The continuous investment in non-invasive electrical, magnetic and radioactive techniques made the research possible for high solids loading conditions. (Barigou 2004; Guida et al. 2010; Stevenson et al. 2010)

The objective of these studies conducted was the applicability of the techniques used for: flow, concentration measurement, investigating off-bottom suspension, the effect of particle size, and the generation of a data set. None of these studies mentioned above covered the disturbance of the turbulence (responsible the suspension of particles) in high solids loading in tanks stirred by axial impellers.

Wadnerkar (2012) took a similar approach to Cokljat et al. (2006) and stated that a third turbulence model could be used for the simulations, namely the per phase model. As mentioned earlier, the mixture turbulence model assumes the domain as a mixture of solids and liquid and solves for  $(k)$  and  $(\epsilon)$  values, which are the same for both the phases. In the dispersed turbulence model, the modified  $k$  and  $\epsilon$  values are solved for the continuous phase, and the turbulence quantities of dispersed phases are calculated using the Tchen-theory correlations. It also takes the fluctuations due to turbulence by solving the interphase turbulent momentum transfer. Motante and Magelli (2005) performed analysis on the turbulence models at the time. They found that the dispersed model provided inaccurate results and predictions while there was negligible difference in the results between the mixture and the per phases models.

The method that Wadnerkar used to perform the calculations is very similar to the research conducted by him previously, therefore it will only briefly be mentioned. The MRF approach was used to rotate a single pitched blade turbine impeller. The impeller was operated normally, generating downwards flow. The top of the tank was modelled as "zero shear" since it is open to atmosphere. A grid dependency study was performed with no considerable difference between the power numbers that was calculated for the respective meshes and therefore taken as negligible. When the residuals and additional parameters were no longer changing the simulation was deemed converged. The calculation was done with time steps of 0.0001s for 10s. The time-averaged data for the last 2.5 s was used for the comparison of results. The simulations were carried out 0, 20 & 40 % w/w with 330, 480 & 590 rpm respectively.

Slip velocities were calculated using the time-averaged component of velocity of the two phases. The slip velocities were normalised using the impeller tip velocity. It was found that the relaxation time for the particles has a very high value of 1.25s, and the Stokes number was 9.94 and 12.21 for 20% w/w and 40% w/w cases respectively. These values are an indicator of high slip velocities in the stirred tanks. The high values in the impeller discharge region were expected due to the large force exerted onto the fluid by the accelerating impeller, while the particle acceleration remains low because of its inertia.

Wadnerkar found that the modified Brucato model worked well up to a Reynolds number of  $1.91 \times 10^5$ . The predictions of the drag model deviated while predicting the velocity components in cases with higher solids concentration (40% w/w) due an under prediction of drag. Further, the increased solid concentration significantly changed the flow field. The false bottom effect at very high solid concentrations results in higher velocity values compared to moderate and low solids loadings. High slip velocities were found below the impeller, near the wall as well as near the impeller rod for PBT. The magnitude of slip velocities increased along with the increase in solids concentration. Dampening of turbulence was evident near the impeller region because of the maximum solids concentration loading at this region as well as the dispersion of solids. The power number also increases linearly with an increase in the solids concentration. External forces need to be accommodated to incorporate the effect of energy dissipation due to particle collision at high solid concentrations.

## 2.2 Solid suspension

In (2002) Bakker et al. studied the CFD modelling of solids suspension in stirred tanks. It was focused on understanding the parameters that govern the just suspended impeller speed  $N_{js}$  and the distribution of solids. The simulations were conducted on solid loadings ranging from 0.5% to 50% utilising CFD modelling.

The Eulerian Granular multiphase model was used to analyse the context of correct scale up and the effect on the quality of solids suspension. A standard 45° PBT turbine was used under different suspension speeds. The solids volume fraction of the fluid volume for speeds just below  $N_{js}$  and the cloud height for impeller speeds operated above  $N_{js}$  were predicted.

Bakker used Fluent 4.52, and the time stepping method coupled with the EGM model to simulate multiphase flows in mixing tanks. The Syamlal & O'Brien model was implemented to account for the granular viscosity of the solids. To calculate the drag force on the suspended particles, Bakker made use of the fluid-solid exchange coefficient developed by Di Felice et al. The turbulence generated by the impeller in the liquid phase was modelled by the standard k- $\epsilon$  turbulence model formulation and the secondary phase turbulence were neglected.

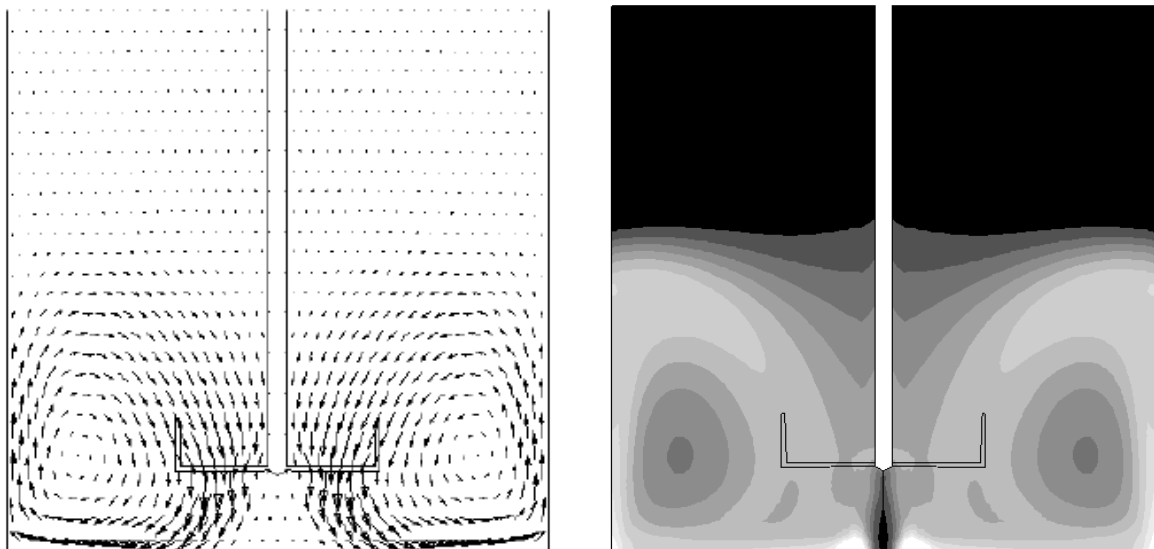
The mixing tank walls and the impeller shaft for both the liquid and the dispersed phase were modelled as no-slip surfaces, ( $u,v,w = 0$ ). The shaft wall was set to a preset rotational velocity.

The impeller was modelled implicitly using internal boundary condition based on laser Doppler velocimetry (LDV) data supplied by the impeller manufacturer.

The simulation was set up using the two-dimensional, axis-symmetric model and a transport equation to simulate the swirl. In the baffle region, the tangential velocity was set to zero, to account for the existing baffles. It was found by modelling the tank in 2D the computational runtime is considerably accelerated. On average, the calculations took about two hours of CPU time to complete.

To support the results, the CFD simulations were compared to the experimental data from Guirard et al., collected from LDV measurements. The predicted velocities were similar to the measured velocity. The velocities were measured at  $r/D$  of 0.464 and 0.961, midway between the baffles. The solid and liquid phase velocities differed from the experimental findings as expected. The velocity of the solid phase trailed the liquid phase velocity as a result of slippage between the phases with maximum variance at the impeller. Towards the top of the tank the liquid phase decelerates, and the solid phase is accelerated by the gravitational influence.

It was found in the study of the effect of agitation speed that the CFD predictions at 1000 rpm were less efficient at suspending solids when compared to the existing experimental data of Godfrey and Zhu. The results of the CFD simulations using 1000 rpm and 390  $\mu\text{m}$  particles are shown in **Figure 4** below. The liquid flow field ranged from 0 – 0.95 m/s. The predictions exaggerated the variation in the axial profile of solids concentration through the single eight-flow loops generated by the down pumping PBT. By using separate turbulence equations for the solids phase, the solid dispersion could be improved to resemble the experimental data, however, the experimental error was not quantified by Godfrey and Zhu, which, also accounts for part of the deviation.



**Figure 4: Flow field of 390 micron particles (Bakker et al., 2002)**

As the mixing rate increases to 1600 rpm, the solids phase tends to be more homogeneously or completely suspended, and no significant deviation in the axial concentration profile was seen. The low clearance between the bottom of the tank and the PBT results in high-velocity gradients projected onto the bottom of the tank. Specific attention should be given to this area as well as near the walls, and the grid resolution should be refined sufficiently to avoid numerical errors and improve the accuracy of the results.

The effect of particle size was also accounted for in the model done by Bakker et al, it was found that as the model particle decreases the drag and slip velocity also decline, which allows the solids phase to be transported more effectively by the liquid phase, enhancing the solids

suspension in the tank. Therefore, as the particle size decreases, solid particles are more completely suspended even when the mixing rate of the impeller is constant.

The decolourization technique was used to compute the mixing time, (t), which showed good agreement with the CFD model. It was found that all local tracers reach equilibrium at approximately the same time. It also was found the correlation between the just speed suspension ( $N_{js}$ ) and the model was inconsistent. This phenomenon can possibly be explained by the low impeller-tank bottom clearance combined with the efficiency of modern impellers. However, the standard deviation of solids volume fraction was shown to be a useful measure of the quality of suspension.

Thorough mixing up to a molecular scale of the reactants is necessary for a chemical reaction to proceed. Micro-vortices are classified as the theoretical minimum size of vortices and is developed by the turbulence in the fluid. The size and characteristics of the micro-vortices is a function of the average specific power input and the viscosity of the liquid. Turbulence does not assist the mixing process further than up to a molecular level. Molecular diffusion of chemicals within the micro-vortices is therefore, responsible for mixing at a molecular level. (Himmelsbach et al. 2006)

Macro-blending time is in general more time consuming than micro-blending time. Micro blending time is usually not considered to be very significant. According to Himmelsbach, the size of the micro vortices in an aqueous solution can be 36  $\mu\text{m}$  with a diffusion rate of approximately  $2 \times 10^{-9} \text{ m}^2/\text{s}$ , thus the micro mixing time would be approximately 0.08 seconds. Designers should always consider if micro-mixing will have an adverse influence on the mixing process. In some cases, it can be decisive, such as when competing consecutive reactions occur extremely quickly.

Himmelsbach et al. (2006) also noted that there are three main objectives by means of solids suspension in terms of agitation rate. In some scenarios on bottom suspension may be sufficient, however, in processes where higher degrees of homogeneity are required, mixing tanks can be placed in series to improve the suspension of the particulates. The three stages of suspension are on bottom motion, off-bottom suspension and uniform suspension. In order to increase the state of suspension, a higher input power and or improved tank geometry is required.

In "on bottom motion" the particles are visible in the solution and the fluid is clear, large zones of clear fluid is visible at the top of the tank, with the bulk of the solid particles rotating at the bottom of the tank.

According to Zwietering, in off-bottom suspension, no solid particles come to rest at the bottom for more than 1 second. "Off-bottom suspension" is often used for large-scale, mineral-processing applications. Off-bottom suspension is defined as the minimum power requirement, where the complete surface of the solids particles is in contact with liquid phase. Zwietering (1958) derived the minimum shaft speed for off-bottom suspension from dimensional analysis and the exponents were estimated from relating experimental databases:

$$N_{js} = S * \nu^{0.1} \left[ \frac{g*(\rho_s - \rho_l)}{\rho_l} \right]^{0.45} * d_p^{0.2} * X^{0.13} * D^{-0.85}$$

**(Equation 6: Zwietering off bottom)**

With S, the dimensionless number (Zwieterings number) for the impeller-tank mixing configuration, determined by experimental data, X, the mass ratio of the solid phase to liquid phase. The equation also considers the kinematic viscosity, solid- and liquid densities, impeller diameter (D) and the average particle diameter (d).

In uniform suspension there is no clear visual distinction between the solid and liquid phases. The coarser particles may continue to settle, when the size distribution of the particles is not uniform. In some processes a very high degree of solids suspension is required, such as continuous overflow operations or the manufacturing of dispersion of products. In these processes the solution is homogenous and the size distribution is uniform throughout the mixing tanks. It is very difficult to maintain this, unless the particle settling velocity is very low.

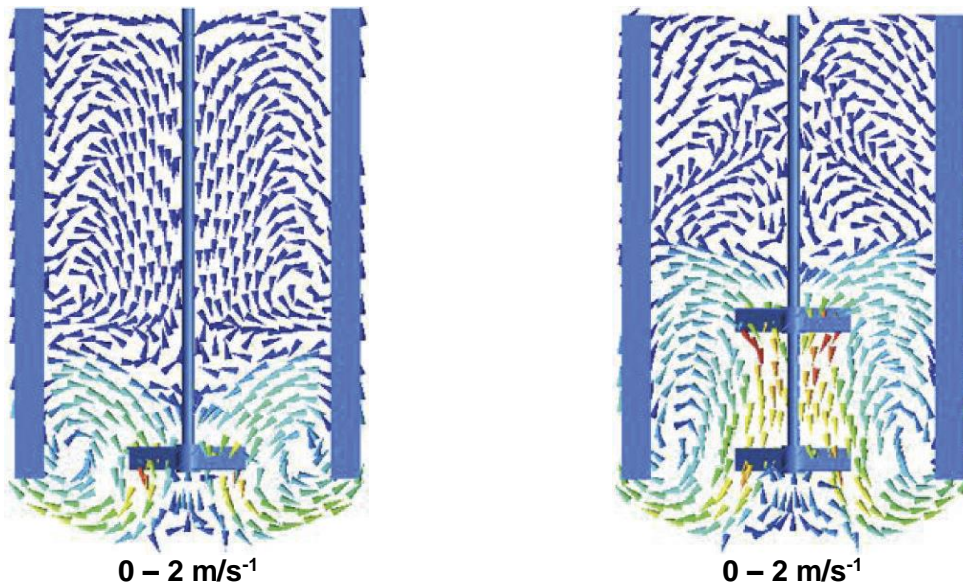
Gohel et al. (2012) studied the CFD modelling of solid suspension in a stirred tank. It was focused in particular on the effect of drag models and turbulent dispersion on cloud height. The Eulerian Granular multiphase theory was applied in the commercial CFD software Ansys Fluent. The realisable  $k-\epsilon$  turbulent was applied to solve the turbulent solid-liquid flow field. Interphase momentum exchange terms were calculated using the Gidaspow (hindered) and the Schiller-Naumann (unhindered) drag models. The MRF approach was also used to model impeller rotation. The no-slip boundary condition was applied to the walls except for the open top which is a free surface and therefore, set to a symmetry boundary. The meshing of the two scenarios are shown in **Figure 5** below.



**Figure 5: CFD meshes for impeller setups (Gohel et al., 2012)**

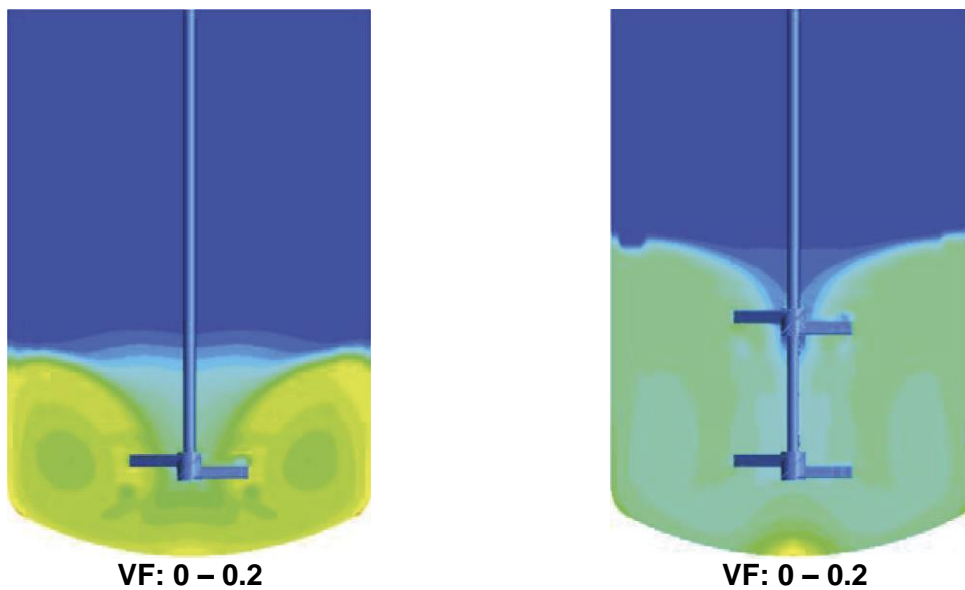
It was found that recirculation zones were evident near the bottom of the tank. Dual impeller configurations and higher rotational velocities predicted larger recirculation zones. At lower impeller rotational velocities, a clear separation could be seen between the cloud at the bottom and the clear liquid above in the mixing tank. The model further predicted that solids were distributed more uniformly throughout the entire mixing tank as rotational velocities were increased.





**Figure 6: Velocity vectors of systems 200RPM (Gohel et al., 2012)**

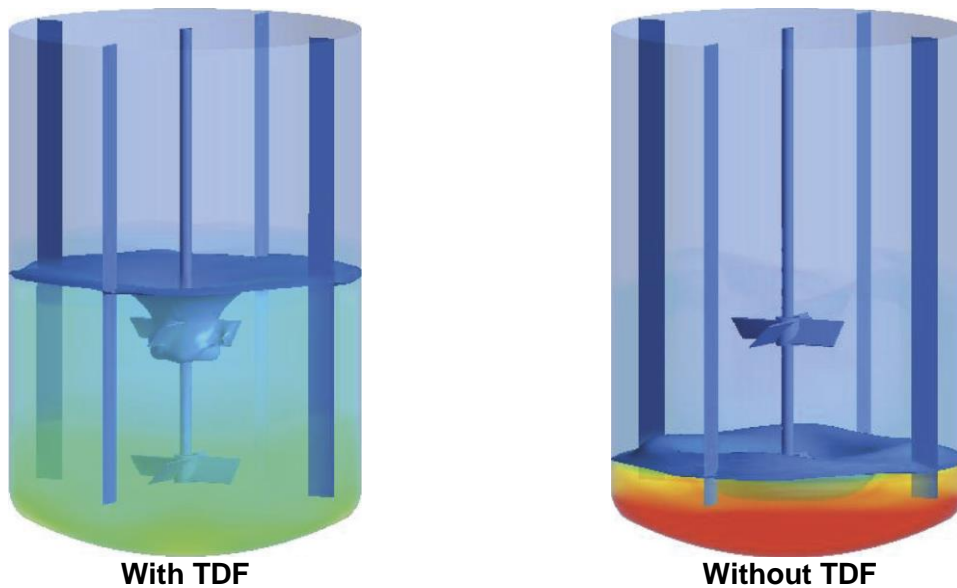
The Gidaspow drag model has been specifically developed to include particle induced hindrance and therefore, should give a good accuracy on high solid volume fractions. Additionally, simulations with the Schiller-Naumann were performed to visually observe the significance of particle hindrance in mixing tanks. It was found that the Gidaspow model is better compared to the Schiller-Naumann with regards to predicting cloud height. Experimental verification further substantiated the Gidaspow model to be a better predictor for cloud height.



**Figure 7: Solids suspension of systems 200RPM (Gohel et al., 2012)**

The inclusion of the turbulent dispersion force (TDF) is important when the length scales of the turbulent eddies exceed the particles size distribution. It was found that TDF substantially increases cloud height and relates better to experimental results. When the TDF function was omitted from the simulations, differences in cloud heights of up to 250% were seen, and therefore, considered essential for realistic predictions.

It was found that the models were predictive over a broad range of solid loadings with different impellers configurations. The model proved insignificant however for single impeller systems at low agitation rates. It was also found that TDF has greater influence than the drag models in predicting cloud height.



**Figure 8: Effect of TDF on solid suspension (Gohel et al., 2012)**

CSIRO released a paper on “CFD predictions on the solid distribution in a stirred tank” by Kubicki et al. (2012). The tank was operated in the just suspended condition, it proved difficult because of the varying solids concentrations within the mixing tank. The distribution of solids is high near the bottom of the tank and low near the top of the tank.

In their model, they utilised the Eulerian multiphase formulation. STAR-CCM+ was used to simulate the suspension of glass particles in a stirred tank. The standard  $k-\epsilon$  model was again used to simulate the turbulence in the mixing tank. They used the Gidaspow model to calculate the drag force of the particles in the liquid phase. To simulate the rotation of the impeller, the MRF method and Rigid Body Motion (RBM) also known as the sliding mesh (SM) method were used. According to Kubicki, RBM is more capable of capturing the impeller-baffle interaction, however, the MRF method is far less computationally expensive.

Kubicki et al. also compared the CFD solids concentration predictions with the experimental data from Guida et al. (2009) for single impeller PBT's. A solid concentration of 5.2% w/w and 10.6% w/w and two impeller speeds were simulated. The turbulent dispersion force was used to account for the interaction between the dispersed particles and the turbulent eddies. The turbulent dispersion force is important in predicting cloud height as pointed out by Lo (2006). The solid pressure force, which takes into account the particle-particle interactions (when the solid volume fraction is close to the maximum packing limit) were also taken into consideration.

A grid dependency study was carried out for polyhedral grids, 300 000 cells up to 1.1 million cells were analysed the solution showed it was grid independent. The setup was similar to previous researchers. All boundaries were considered walls except the tank top that was modelled as a symmetry plane. Walls will dissipate turbulence but not by a symmetry plane. A slip wall could be used at the top of the tank to represent the top boundary. The simulations were initialized with uniform distribution of solid particles.

The velocities for the RBM model were computed over five impeller revolutions since after five impeller revolutions no further changes in average quantities were observed. It is shown that the RBM and MRF models generate very similar results. On average the steady MRF took 18 times less time to solve than the transient RBM. For the MRF model, the converged solution was reached after 40 000 iterations, whereas the RBM requires 80 000 iterations to resolve the flow field for four seconds of mixing.

In all cases, the CFD models closely represented experimental data. The CFD model correctly predicted the solids distribution and the cloud height. The impeller showed close agreement when operated to pump the fluid axially downwards but not as promising when the impeller was operated in reverse to propel the fluid upwards. "The reason could be in down pumping mode the measuring plane is recording fairly well-defined flow discharged from the impeller, whereas the up pumping mode the measuring plane is recording returning flow back to the impeller after passing through the complex turbulent mixing flow in the tank." (Kubicki et al. 2012)

In down pumping mode, the RBM model does not significantly improve the velocity prediction indicating that turbulence modelling is a source of error as shown by Joshi et al. (2011)

### **2.3 Tank configuration and geometry**

August 2010 Ochieng et al. published a scientific paper on the CFD simulation of solid suspension in stirred tanks. According to Ochieng, important characteristics of mixing tanks are the hydrodynamics and the capability to mix fluid or phases. Industrial processes such as flotation, precipitation and biochemical reactions rely on these parameters. In these systems, the mass transfer process is what limits the reaction rate. Reaction rate is largely generated by the convective motion of the impeller at larger scales, it also induces the turbulence required for the smaller scales, down to diffusion in the molecular scale.

The objective of their work was to summarize the work already done by other researchers and the current state of research with regards to CFD simulations of solid-liquid mixing in agitated tanks. Ochieng et al. specifically focussed on the hydrodynamic properties of the mixing tank such as the solid cloud heights, off-bottom suspension and drag & non-drag forces. In solid suspension systems, it is important to know the particle size distribution requirement applicable to the process. Processes require either just suspension or total solids suspension after complete solids suspension cloud heights become important. To understand how hydrodynamics, affect the homogeneity in solids suspensions systems, detailed simulations and extensive experimental research data on solid-liquid interactions are required.

It is known that round-bottom mixing tanks eliminate dead zones. The important advantages of the high aspect ratio tanks include high volumetric loading and efficient use of space. However, the increased segregation area as well as in hydrostatic pressure are drawbacks to the high aspect ratio tanks. Draft tubes can be placed into the tank to reduce the dead zone within the fluid flow field. Mixing tanks can either have flat or profiled bottoms, the degree of curvature of the bottom can be altered to match the process requirement. Flat bottom profiles are usually sufficient for liquid applications, whereas, for solid-liquid applications dished or elliptically bottom tanks is normally required to aid the particle suspension.

A large number of industrial processes are operated in the turbulent flow regime, the specific Reynolds number classed as fully turbulent flow is inconsistent in literature.  $Re > 4000$  is usually considered to be turbulent flow. However, Reynolds number does not take into account the size or aspect ratio of the tank. Fluid flow near the wall of the tank may be laminar or turbulent, depending on the diametric ratio of the impeller to tank, the impeller rotational velocity, and the tank aspect ratio. The combination of operating parameters and the geometry of the tank, affects the solid-liquid interface features, such as off-bottom suspension and the

cloud height. The measurement and modelling of mixing tanks with high solid concentration loadings still requires improvement, since intrusive techniques are required, which cause disruption to the natural flow patterns.

Solids suspension is focussed on three aspects: Off-bottom solids suspension, solids cloud height, and solid concentration distribution. Off-bottom suspension was simulated with single impeller and multiple impeller systems. The impellers provided the degree of mixing typically required in a mixing application, which is dependent on the process at hand. In the case of crystallisation and precipitation, the rate of reaction is dependent on the particle surface area in contact with the liquid phase, for optimum contact complete suspension is necessary.

The most common method still used to quantify off-bottom solids suspension is the critical impeller speed ( $N_{js}$ ) of (Zwietering, 1958). According to Armenante (1998) the just suspension speed depends on the impeller to bottom clearance and the impeller-tank diameter ratio. Sharma and Shaikh (2003) have shown the suspension of the solids are affected by the distance of the impeller to the bottom of the tank. At low impeller clearance ranges the energy transferred from the impeller to the solids is improved

Low clearance ranges provide improved energy transfer from the impeller to the solids, and the ratio of the local energy to the overall energy dissipation per unit volume is constant. The fluid projected by the impeller is deflected by the bottom of the tank and disperse the solids.

Himmelsbach et al. (2006) also stated that, in addition to agitator parameters and tank geometry, the solids suspension is affected by the hydrodynamics in the mixing tank, which in turn is influenced by the properties of the solid and liquid phases. The physical properties crucial to mixing tank design are the liquid phase density, the change in density between the liquid and solid phase, the viscosity of the liquid phase, the average particle size distribution and the volumetric solids concentration.

The free settling velocity is calculated by using the following equation:

$$v_{sh} = v_s(1 - C_v)^m$$

**(Equation 7: Settling velocity)**

Where,  $v_{sh}$ , - hindered settling velocity,  $v_s$  - free-settling velocity and  $C_v$  - volume fraction of solids.

The equation below can be used to quantify the settling power, when the following assumption is made. All the particles are uniformly distributed in the liquid phase, and that all particles start settling at once due to the effect of gravity:

$$P_{settle} = v_{sh} * c_v * \Delta\rho * g * V$$

**(Equation 8: Settling power)**

Where,  $\Delta P$  is the change in density between the liquid and solid phase. The mixer must provide a consistent energy input in order to counteract the effect of gravity on the solid particles and keep the suspension of the solids uniformly distributed in the liquid phase. The power input required by the impeller is always a multiple of the settling power.

When using the formula above, it is important that the particle size selected for calculating the free settling velocity, ( $V_s$ ), is correct. In practice, the size and shape of particles will be inconsistent, simply choosing the largest particle for the calculation will result in over-designed and expensive mixers. According to Himmelsbach, the general rule of thumb is to design the

agitators with a particle size at which the bulk (typically 80%-90%) of the solid particles would pass the reference mesh.

According to Genck (2003), in order to optimize the hydrodynamics for mixing crystallization applications the following design considerations should be taken into account. An impeller suitable for the intended purpose, calculating the optimum impeller to tank diameter ratio and the position of the impeller within the fluid domain.

The impeller is an essential component of crystallizer design and must be capable of:

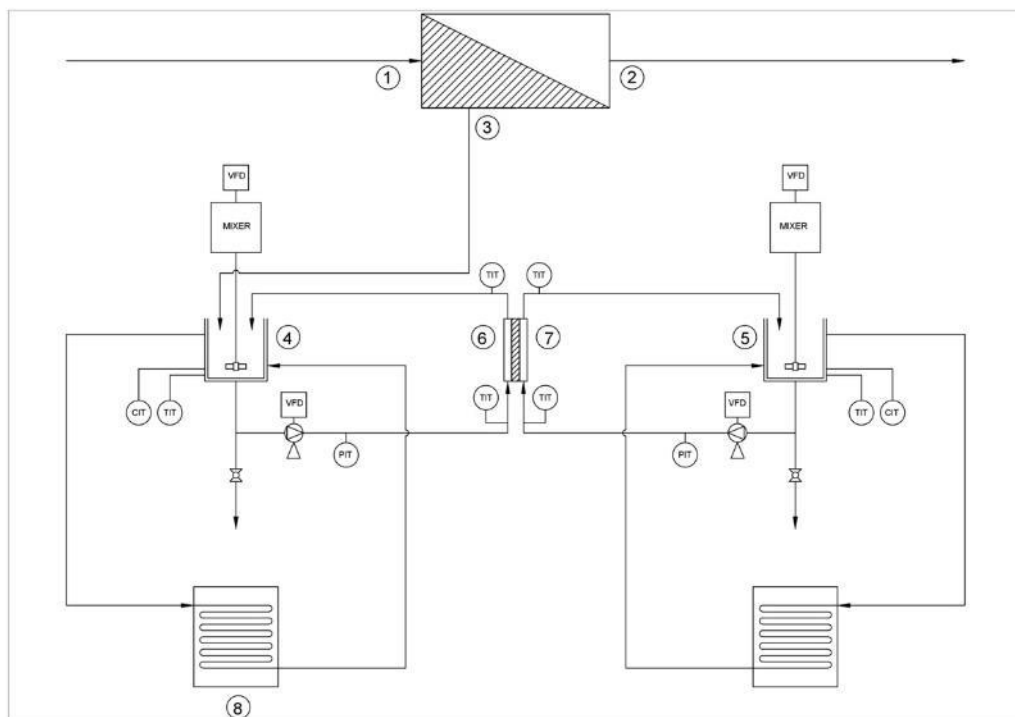
- Keeping the solids in suspension to catalyse crystal growth.
- Providing sufficient mixing to prevent excessive localized super saturation areas at the feed points, cooled down surfaces and evaporation surfaces to avoid primary nucleation and deposits.
- Sufficient mixing for effective heat transfer for heating and cooling applications, in order to operate within the metastable zone.
- Bleeding of the product by means of isokinetic discharge
- Maintaining sufficient levels of secondary nucleation required to achieve the sought particle size distribution. (Genck 2003)

Shah et al. (2009) stated that baffles are mostly a requirement for round mixing tanks, except for very high Reynolds number applications. Baffles are necessary to prevent vortexing, and the rotation of the entire fluid volume. The industry standard is four radial baffles spaced equally. Six are only slightly more efficient, and three are insufficient. If the impeller is placed off-centre in the solution (one-fourth to one-half the tank radius), less swirl is observed and the need for baffles is lessened, particularly for low viscosity applications.

## CHAPTER 3: Membrane Distillation Experiment

### 3.1 Process design

A lab scale DCMD unit was designed, manufactured and set up using three types of PTFE hydrophobic membranes, the P&ID diagram is shown in **Figure 9** below. DCMD was selected as the preferred setup as higher permeate flux rates can be achieved since the membrane is direct contact with the heated and cooled water sides, creating greater thermal conduction, but at the expense of heating and chilling demand. AGMD works in a similar manner but with added loss in thermal efficiency from the air gap. Temperature polarisation is also a disadvantage of AGMD, however not to the same scale as DCMD since the cooling solution is separated from the feed solution by the air gap, reducing thermal conduction. (Dow et al. 2008). By incorporating an air gap into the membrane holder, it complicates the design, making DCMD the most attractive option for the experimental setup. The mixing crystallizer tank relating to this work is shown at point 4 below.



**Figure 9: DCMD Piping and instrumentation diagram (Smith, 2015)**

Brackish or seawater containing any amount of solutes is forced with high pressure pumps through the reverse osmosis membranes in stream 1 in above. The high energy input from the high-pressure pumps is to reverse the process of natural osmosis. The semipermeable membrane retains up to 99% of the solutes, which is rejected in the concentrated saline stream (brine) shown at point 3.

In order to force the solution through the membrane, backpressure is applied by means of a throttle valve in the reject stream. The pressure differential is the driving force pushing the water through the membrane. The purified water molecules that pass through the semi-permeable membrane is collected in the permeate stream shown at position 2 in the figure above.

The concentrated saline solution is then accumulated in the feed tank of the DCMD setup. The feed tank (point 4) is heated and the permeated solution (point 5) is chilled. In this tank, supersaturation will occur and subsequently, crystals will start nucleating. Both tanks were equipped with PBT's to provide necessary agitation and promote the nucleation process. The experiment was executed at different temperatures in order to determine the optimum operating conditions. In the experiments, three different wastewaters with different salt concentrations were used to determine the membrane's performance.

The membrane is depicted in the hatched area between points 6 & 7. As mentioned earlier the heated solution is passed through point 6 and similarly the cooled down solution is passed through point 7 on either side of the PTFE membranes, which is placed in the centre.

### **3.2 Control philosophy**

The project required that temperature, conductivity, pH and pressure could be monitored for the duration of an experiment. It was further required that the data be graphed in order to envisage and understand the development of the process. In order to do this, the following options were considered to select the most suitable method:

- I. Manual measurements with interval data capturing by the use of handheld instruments.
- II. A semi-automated system with individual displays and controllers for the respective instruments and manual data logging.
- III. Fully automated system with a human machine interface, programmable logic controller and analogue inputs with fully automated logging and data processing capability.

For ease of use, minimising human error, collecting data from the equipment and logging, the fully automated were selected. It was further required that operation of the machine is simple and easy to change the parameters. It was decided that the most efficient method to perform all these activities is a PLC and HMI setup. The PLC - HMI setup has built-in standard functions such as temperature recording from PT100 temperature probes. Other data is received from analogue input modules to the instrumentation controllers. The HMI has an incorporated PLC, it is fully customizable and can accommodate mathematical formulation and other user-defined equations. The PLC is able to run the experimental program time dependent and measures data at the pre-set intervals.

### **3.3 Process equipment & instrumentation**

The following parameters needed to be measured and recorded accurately, to study the membranes actual performance:

- I. The temperature in the feed solution, permeate solution, and the transmembrane temperature difference are precisely measured.
- II. Conductivity, measured in the feed and the permeate solution in order to verify the membranes salt rejection and the formation of crystals in the feed solution.
- III. Flow rate is controlled at the feed and permeate side in order to set the permeate flux rate.
- IV. A balance will be used to calculate the permeate flux rate.
- V. pH measurement in the feed solution to ensure acceptable feed water quality.

The circulation pumps used in the MD process are two peristaltic type Watson & Marlow pumps. Peristaltic pumps were selected for the following advantages. The pumping mechanism is never in direct contact with the pumped fluid and the tubing (wear parts) in the pump head is easily interchangeable. Another advantage of peristaltic pumps is its easily adjustable variable speed to set a sizeable range of precision flow rates. The pump is able to communicate to a desktop computer via RS 232 to the USB port.

The feed solution was heated using a thermostatic circulating unit (Lauda RE415). The heating solution (Kryo 40) was circulated through a jacketed feed water tank. The heated solution was pumped through the outer cavity "Jacket" of the tank. The conductive heat transfer between the jacket and the inner fluid volume heats up the primary solution without direct contact to avoid any contamination, the boundary between the primary and secondary solution was made from stainless steel 304.

A Chiller (Lauda RP855) was installed on the permeate side to cool down the permeate stream and create the necessary vapour pressure difference between the heated and the cooled down solution. The solution on the product circuit is indirectly cooled by means of a copper tube heat exchanger placed into the product water tank. The heat exchanger design is based on the specific heat transfer coefficient of the copper tubing and the heat removal required based on an energy balance over the membrane distillation system.

Agitators were installed in the tank to promote effective homogeneous mixing and optimise heat transfer. The overhead agitator has a variable speed drive (VSD) with the potential for measuring output power, from this, the torque increase could be calculated and ultimately a calculation could be done to measure the change in viscosity.

To measure the temperature, PT 100 temperature transmitters were used for the recording of the temperatures at the specified locations in the MD setup. The temperature transmitters were connected to the analogue input modules of the PLC. The transmitters transmit a 4 -20 mA output, which is converted by the PLC into degrees Celsius or any other unit of measure. The 4mA is scaled to the minimum measurement required in the setup and likewise the 20 mA corresponding to the maximum temperature within the system. The placement of the PT 100 transmitters was carefully selected within the setup to minimise the length of the signal cables to allow for more accurate readings.

Electrical conductivity was used as a measurement for the TDS within the solutions, since inline TDS meters does not exist yet and electrical conductivity provided a suitable alternative. Although, not completely as accurate as the laboratory TDS analysis, it is usually very close to the actual TDS value if a meaningful correction factor is applied. Conductivity cells were placed in the feed tank, product tank as well as before and after the MD unit. The conductivity cells were also connected to the analogue inputs in the same manner. Similarly, they were scaled to the required range.

pH probes were installed into the feed and product tanks. The pH probes provided a 4-20 mA output converted by the PLC into a reading. The pH probes were not directly connected to a PLC input, in reality, they are connected to a pH controller that converts the millivolt output signal into readable data for the PLC unit.

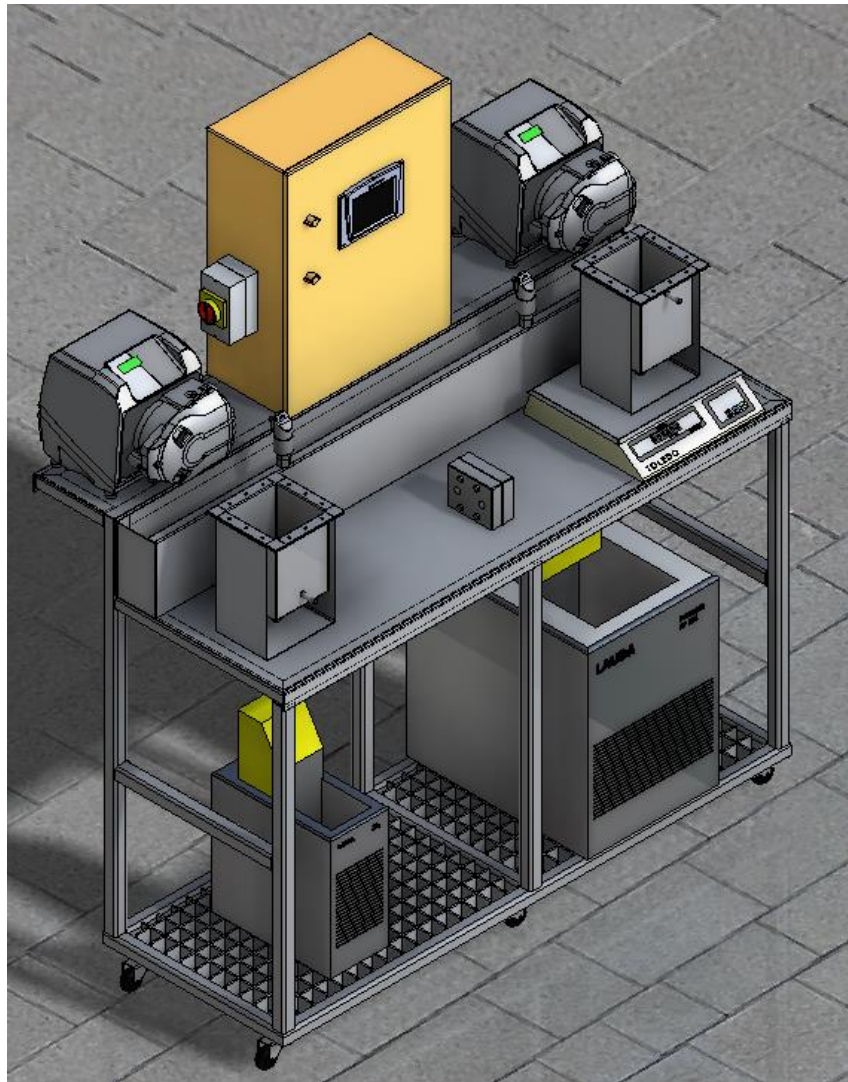
The PLC controller actively monitors all signals, which in turn plot them into graphs for easy visualisation. This data is displayed on the HMI. The control of the process was also executed on this unit. Memory shortage on the PLC forced the data to be automatically exported onto a desktop PC or SD card to capture the data for the entire duration of the experiment.

### **3.4 Manufacturing of equipment**

The entire MD experiment was designed in the commercial software package Autodesk Inventor 2014. The manufacturing drawings are presented in Appendix B. It will be used mostly in laboratory environments, therefore, the experimental setup must be able to fit through a standard office door. The dimensions were subsequently restricted in height but not in overall length. The process equipment was carefully located onto a frame to be easily accessible and



ergonomically pleasing. Since the experiment uses saline liquids care was taken to select the most suitable materials of construction for the parts.



**Figure 10: CAD model of experimental rig**



Figure 11: Photograph of the experimental rig (Nathoo, 2015)

### 3.4.1 Jacketed tanks

Stainless steel 304 was selected as the preferred material to manufacture the tanks for the following reasons: it is relatively easy to manufacture, easy to modify, good conduction properties and corrosive resistant. The tanks have a capacity of approximate four litres each. The tanks were designed as bendable flat profiles. The flat profiles were bent up and TIG welded with stainless steel filler material.

To minimise the chances of air pockets forming within the jacket, the inlet of the jacket was positioned at the bottom of the tank with the outlet positioned at the top. By having the in- and outlet positions at different heights also prevented short circuiting of the heating and cooling solutions.

The jacket was pressure tested up to one bar to ensure there will be no fluid transfer from the jacket into the experimental solution and also to prevent any loss of the primary fluids. The tanks had tapered bottoms to allow all fluids to be drained from the tanks after the experiment to ensure effective removal of all impurities that may cause irregular results in subsequent experiments.

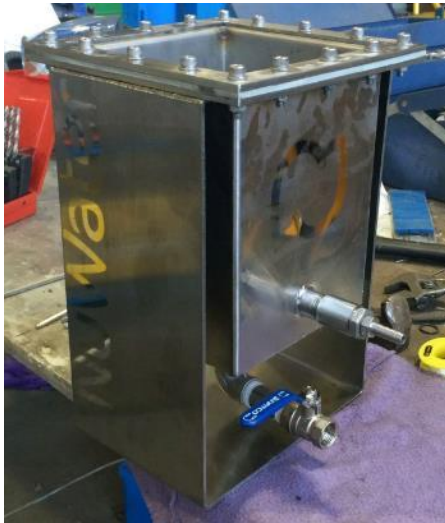


Figure 12: Rectangular jacketed tanks (Smith, 2014)

### 3.4.2 Impeller

To provide agitation, a standard pitched blade turbine (PBT) was selected on both the feed and the permeate crystallizer tanks. A PBT was chosen as it is one of the most basic axial down pumping impellers and the manufacturing could be done in-house.

The agitator was manufactured from stainless steel 304; a rod was machined with key slots to prevent rotational slippage of the impeller. Grub screws penetrating through the wall of the bush clamped the shaft to the impeller as well as the motor to the shaft.

A 6 pole three-phase 160W motor was used to power the agitator, 6 poles were preferred since its normal rotational velocity is slower compared to the standard 2 pole motor at 50 Hz frequency. A variable frequency drive was connected to the motors in order to control the speed and measure the torque applied by the motor onto the impeller.

The VSD's were connected via an Ethernet connection to the human machine interface (HMI), the connection allowed for both agitators to be operated independently on the HMI with minimal effort. The impeller frame was designed and manufactured in a cantilever way, which also allowed the impeller to be removed from the tank and be adjusted in height easily.



Figure 13: Pitched blade turbine (Smith, 2014)

### 3.4.3 Frame

The materials considered for the MD frame were stainless steel, galvanised mild steel and epoxy coated mild steel. Stainless steel was again selected as the preferable option because of its excellent corrosion resistant properties.

The lab scale workbench was designed on Autodesk Inventor 2014 with a complete stress analysis to ensure the frame will not bend or buckle when all the equipment is mounted on the frame. The frame was modelled in 3D using 40 x 40 x 2 rectangular tubing for the easy manufacturing and to limit sharp edges.

Complete manufacturing drawings were produced and the construction of the frame was done at Nuwater's steel workshop. Swivel castors with a safe working load of 75 kg each were mounted to the bottom of the frame in order to move the MD experiment. Two-swivel castors diagonally from each other were the lockable type to prevent unwanted movement.

At the base RS 40 x 40 x 4 mm glass reinforced plastic grating was installed as the floor for the chillers. The grating prevented water from accumulating underneath the chillers and cause corrosion. For the bench top, 2 mm stainless steel 304 was selected to compliment the stainless steel frame. A cover plate was added for the connections to minimize modifications to the backbone, which could also be used for different experiments in the future as shown in **Figure 14** below.



Figure 14: Stainless steel Frame (Smith, 2014)

### 3.4.4 Membrane holder

The casing halves were machined from stainless steel 316. It houses BSP threaded feed and permeate connections. This configuration allowed for simple connection of the tubing and inline instrumentation. A double O-ring was used to seal the connections from membrane properly. Common EPDM rubber O-rings were selected since it is inexpensive and readily available. The feed and permeate spacers were constructed from polyester fabric and can be purchased fairly easily, should replacement be required.

### 3.4.5 Electrical installation

The control panel is supplied by 3 phase, 440 V @ 50 Hz. Single phase is used to power the 24 VDC power supply for the control circuit, the pumps, and the chillers. The VSD's for the motors of the mixers is powered by 3 phase supply.

The control panel is located at the highest point of assembly, where it is clear from most water activities and still easily accessible. The VSD's were installed away from the "splash zone" to

protect it from water damage. The VSD's controls the speed of the impeller to the pre-set rotational velocity on the HMI screen. The VSD measured the output power and provided a 4-20 mA output to the HMI, which is converted by the PLC into a torque on the shaft reading. Two made up solutions with individual viscosities close to the actual solutions could be used for the calibration. By incorporating the basic formulas below into the PLC code, the viscosity is displayed on the HMI.

$$P = T\omega$$

**(Equation 9: Shaft power)**

Where P is the power measured on the shaft. The angular velocity  $\omega$  was computed from the preset rotational velocity N by the user. By combining these formulas, the torque on the shaft could be computed and the PLC calibrated according to prepared solutions with known densities, in this manner the viscosity change data could be collected.

$$\omega = \frac{2\pi N}{60}$$

**(Equation 10: Angular velocity)**

$$T = \frac{60P}{2\pi N}$$

**(Equation 11: Torque on the shaft)**



**Figure 15: Electrical cabinet and VSD's (Smith, 2014)**

### 3.5 Commissioning of experimental equipment

#### 3.5.1 Electrical check

Electrical check: Note! The constructor of the panel is not allowed to perform the check below.  
**NOTE! THE FOLLOWING CHECKS SHOULD BE PERFORMED WITH SUPPLY POWER DISCONNECTED FROM THE PANEL**

<b>WIRING CHECK</b>		<b>YES</b>	<b>NO</b>	<b>IF NO, PLEASE SPECIFY</b>
<b>TEST</b>				
Is the panel wired according to the drawings?				
Is the panel conforming to agreed standard?				
Is the panel wiring clearly marked and visible?				
Is the wiring done neatly?				
Pull gently on all cables to ensure they are fixed. Pass?				
Do all wires have enough slack?				
Perform short circuit testing on all circuits and PLC outputs. Pass?				
Perform continuity testing on all relays, contacts and switches. Pass?				
<b>COMPONENT CHECK</b>				
Are all push buttons, switches and contacts checked?				
Is the fuse amperage(s) as specified by the drawings?				
Are all components clearly marked?				
Are all component securely fixed?				
<b>NOTE! CONNECT THE POWER SUPPLY TO THE PANEL</b>				
<b>FUNCTIONALITY TEST</b>				
Does the HMI turn on?				
Is the error log clear?				
Is the Emergency Stop functioning?				
Does the E-Stop reset button function?				
Is the correct program loaded for the machine to be tested?				
Are the recipes preloaded on the HMI?				
When the PLC is reset, are the settings still available?				

Table 1: Electrical inspection sheet

### **3.5.2 Mechanical check**

- Check that the installation is rigid and safe for usage
- Ensure all connections are securely fixed
- Inspect water hoses for visible damage
- Pressurize system and check for leakage
- Check wheel locks are functioning

### **3.5.3 Functionality check**

- Check that all sensors are live
- Ensure that all sensors are scaled correctly
- Calibrate all sensors
- Check chiller heating & cooling for both sides
- Check pump fluid direction
- Check impeller/motor direction

## CHAPTER 4: Solid suspension experiment

The tanks manufactured of stainless steel in the MDC experiment created another challenge, it was impossible to observe the particle suspension in the tank and more importantly at the bottom of the tank. Cameras could also not be used as it disturbs the flow field and alters the suspension. Inspection windows could also not be used since the tanks were jacketed and the fluids were not allowed to interact as it will completely compromise the crystallization results. In the absence of Laser Doppler velocimetry (LDV), tracers or similar specialized experimental equipment, the only option remaining was to manufacture a completely new tank and record the experiment at 1 second intervals.

### 4.1 Construction

A clear polycarbonate tank was manufactured for the experiment to observe the particle suspension within the fluid domain. The tank was manufactured to the exact dimensions of the CFD simulations and the MDC experiment. To gauge the cloud height, Autodesk Inventor was used to create a 1:1 ruler for the tank as shown in **Figure 16** below. A new impeller was manufactured from stainless steel 304L on a 5-axis CNC milling machine to match the geometry of the numerical simulations exactly.

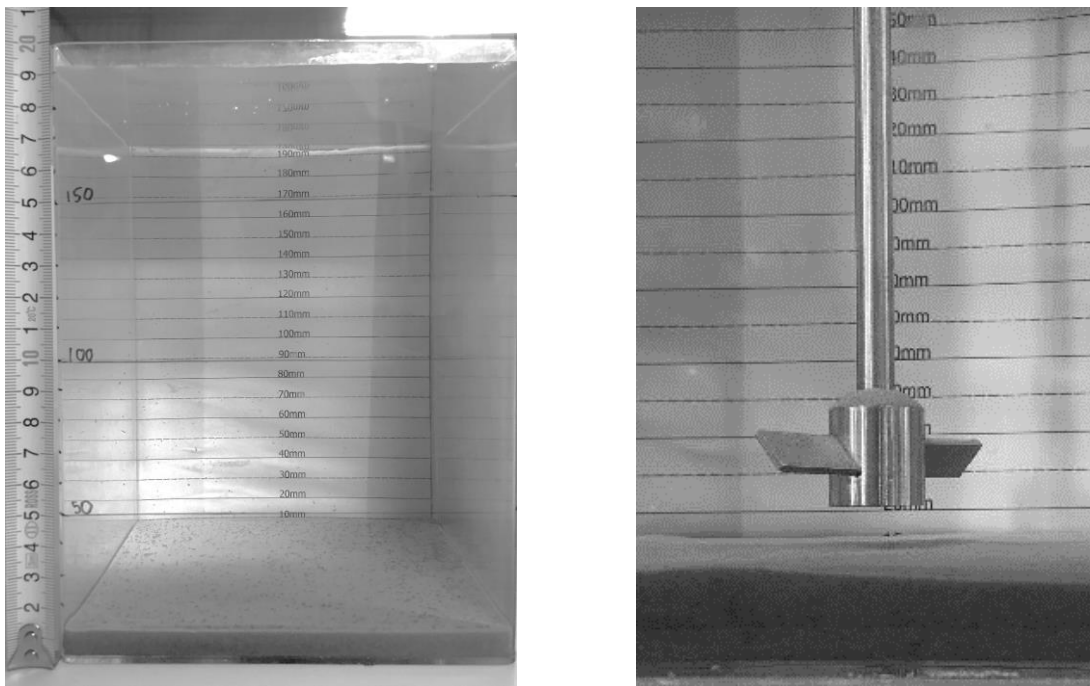


Figure 16: Experimental setup (Smith, 2018)

The agitation was provided by a DLAB OS40-pro digital lab scale stirrer. The lab stirrer had a maximum inaccuracy of  $\pm 3$  rpm. In order to simulate the calcium carbonate crystals, the tank was loaded with 5% silica by volume. Silica was selected for the experiment as it is readily available and the properties resemble that of calcium carbonate crystals. See **Figure 17** below. A 150 micron screen was used to sieve the silica to get the bulk density and particle size distribution as close to the configuration used in the CFD simulations as possible. Colloids were removed by agitating the mixture and then draining the murky fluid from the top. The process was repeated until the bulk of the suspended solids were granular and settling within a few seconds after agitation. The impeller was accurately positioned to the centre of the tank and the tank. Subsequently, the tank was filled with water at room temperature up to a height of 190mm.



To minimize the effect of the camera angle and avoid parallax, a black marker was used to mark the scale on the front of the tank. The camera was aligned to the centre of the fluid volume at 100mm before the experiment was initiated.

## 4.2 Experimental results

### 4.2.1 Experiment - 600 RPM

It was found that at 600rpm the flow field takes  $\pm 15$  seconds to stabilise. Uniform accumulation of solids in all four corners are clearly visible. The cloud takes approximately 15 seconds to reach the waterline. After the flow field has stabilized, it was seen that the cloud was suspended at approximately 10mm from the waterline. Solids accumulation in the bottom corners are clearly visible in **Figure 17** that shows the solution is only partially suspended. Minor vortex formations were seen at the waterline around the shaft along with highly turbulent flows on the flat surface between the corners where the particles are suspended primarily.

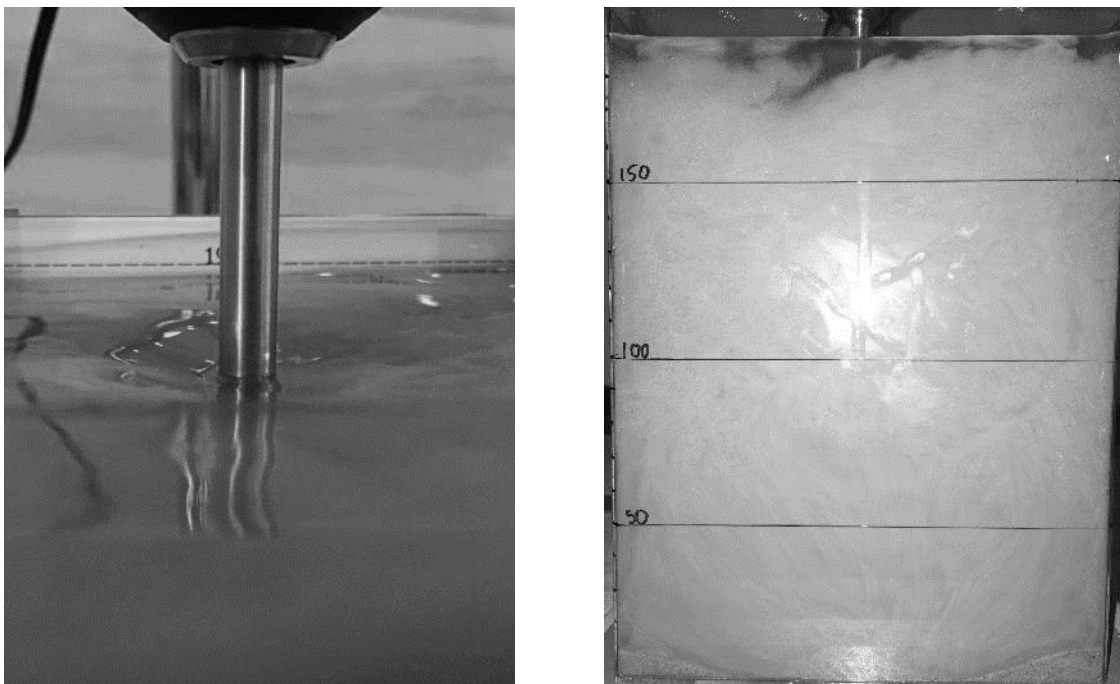
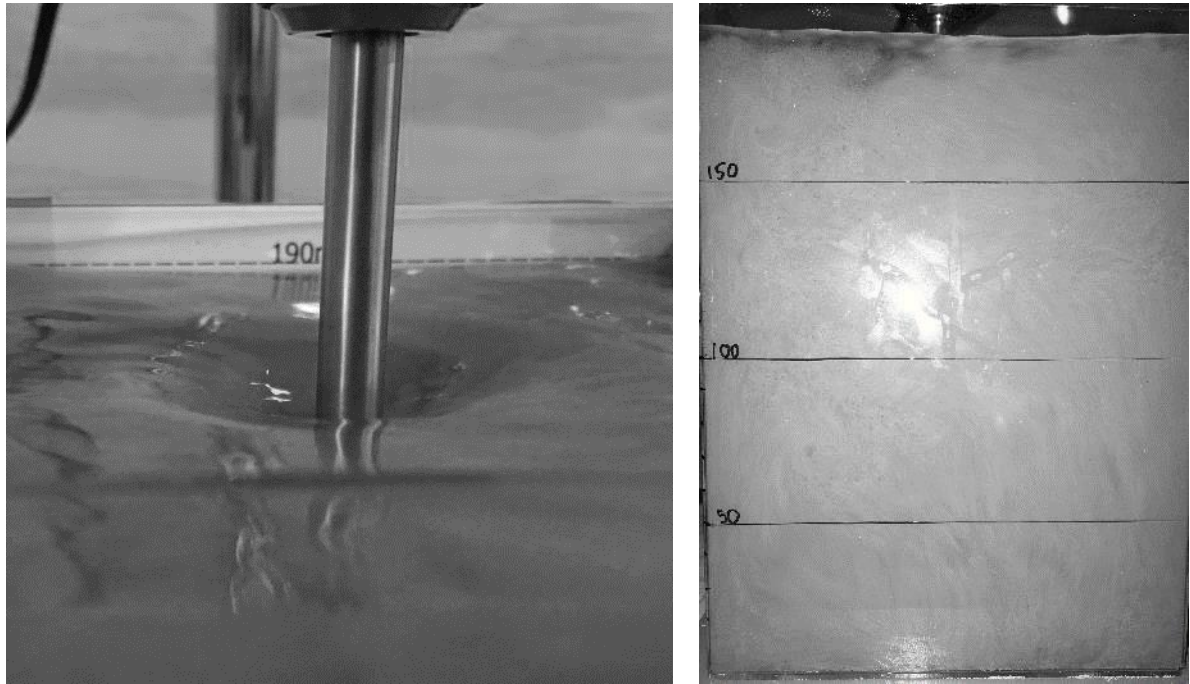


Figure 17: Vortex and flow field at 600RPM, 15s (Smith, 2018)

### 4.2.2 Experiment – 750 RPM

When operated at 750 rpm the solution reaches complete suspension at approximately 15 seconds as well. Periodic clustering of solids are seen at the bottom corners for split seconds. This shows that the mixture have reached the just suspended condition.

The vortex formations around the shaft were intensified at the higher impeller speeds. It can further be concluded from the experiment that the corners of the tank are sufficient in preventing excessive horizontal velocities, which causes rotational swirl.



**Figure 18: Vortex and flow field at 750RPM, 15s (Smith, 2018)**

The experiment showed weak solids suspension in the corners, which could be the result of a combination of the following factors:

- Less intense flows were seen in the corners.
- The distance between the corners of the tank and the impeller tip is at a maximum.
- Axial up flows necessary for effective solids suspension are restricted since the bottom of the tank is flat, causing “dead spots” in terms of flow velocities.

From the experiment it could be concluded that the solids suspension ranged from partial to complete suspension between 600 - 750 rpm. The suspension of the calcium carbonate crystals in the experiment agreed well with the data from the silica of the suspension experiment. Based on these findings, granular silica particles could be used for the comparison of the tanks in the numerical simulations.

## CHAPTER 5: Numerical simulation

### 5.1 Computational fluid dynamics

In modern times computational fluid dynamics (CFD) has become an accepted tool for studying the crystallisation process. The mixing process can be investigated at different scales such as macromixing, mesomixing and micromixing by conducting a staged modelling approach. If the crystallization kinetics are known of an actual process, the models can be incorporated into the technology by the user to accurately predict the particle size distributions or numerous other related parameters. (Ansys Fluent 12.0, 2009)

Fluid flow is governed by conservation laws of mass, energy and momentum. In order to compute these characteristics, a set of partial differential equations (PDE's) are usually required. CFD solves a set of PDE's utilizing numerical simulations to generate qualitative and quantitative predictions of fluid flow. In computational fluid dynamics, the fluid domain needs to be divided into small elements or grid. By using the discretization scheme, PDE's are solved to represent the variables of mass, momentum and energy balance at any given position within the centre of the cell. The initial boundary conditions are used to solve these differential equations. In order to control convergence, stability, and the accuracy of the solution, additional control parameters need to be included. These PDE's are solved iteratively until the solution converges with the pre-set parameters called the convergence criteria. (Ansys Fluent 12.0, 2009)

All commercial software packages available in the market consist of three distinct phases of calculation namely pre-processing, solver and post-processing. In the pre-processing, the geometry of the model is drawn or imported and adapted for use in the meshing platform. The solver receives the input files set up by the pre-processor. Thereafter the simulations are calculated for a set period or until the solution reaches the pre-set convergence criteria. During the runtime of the calculation, the progress can be monitored and initial conclusions can be drawn. In the post processor, the results can be manipulated to display the areas of interest in the required setting to examine the data in depth.

#### I. Advantages of CFD:

- CFD simulations are less expensive than experimental or physical solutions and are usually generated in much shorter time frames.
- The researcher can study a large number of locations in the area of interest, CFD generates an extensive group of flow parameters that can be further examined.
- CFD allows the user great flexibility to exclude certain parameters in the physical process to clarify the area of study. (Bakker 2006)

#### II. Limitations of CFD:

- CFD models were developed from experimental, real world processes such as turbulence, chemistry, multiphase flow and compressibility etc. that could have contained errors.
- Rounding errors from the computer that solves the PDE's.
- The numerical models are large dependant on the initial/boundary conditions used in the setup, which affects the accuracy of the solutions. (Bakker 2006)

## 5.1.1 Fluent governing equations

CFD methods are based on the first principles of mass, momentum and energy conservation, as described by the Navier-Stokes equations. The solutions for mass, momentum, energy and species at thousands of locations within the flow domain are computed numerically. The computed solution provides flow variables such as velocity, pressure, temperature, density, concentration, etc. (Andersons 2009)

### 5.1.1.1 Turbulence

One of the main means to classify the characteristics of fluid flow is Reynolds number. Turbulence is a natural occurrence of fluids when the velocities are high, and fluctuating in all directions with an infinite number of scales. Therefore, solving the Navier-Stokes analytically, becomes impossible, because the fluid flow is elliptic, nonlinear, coupled (pressure-velocity, temperature-velocity). Turbulence is chaotic, dissipative, diffusive, intermitted and transpires in all directions. (Paul et al. 2004)

### 5.1.1.2 RANS Based models (Time-averaged)

The mean velocities coupled with the fluctuating velocities provide the actual velocity. By substituting the actual velocity into the momentum equation, gives rise to the “Reynolds Averaged Navier-Stokes” equations. The factors containing fluctuating components terms averages to zero after time-averaging a large number of cycles of fluctuation. These models include Reynolds stresses, from where more unknowns to the RANS equations are created, which need to be accounted for by adding additional variables. As a result, the turbulence models were developed, the most common models are listed below. (Ansys Fluent 12.0, 2009)

- I. One equation models
  - a. Spalart – Allmaras
- II. Two equations models (Eddy viscosity models)
  - a. Standard  $k-\epsilon$
  - b. **RNG  $k-\epsilon$**
  - c. Realizable  $k-\epsilon$
  - d. Standard  $k-\omega$
  - e. SST  $k-\omega$

Based on extensive research and work by previous researchers the RNG  $k-\epsilon$  was selected as the most suitable model in this work for its robustness and the handling of rotational swirl.

### 5.1.1.3 Renormalization group (RNG) $k-\epsilon$ model

A typical model used for engineering applications is the  $k-\epsilon$  turbulence model, where  $k$  is the turbulent kinetic energy transported variable and  $\epsilon$  the turbulent energy dissipation rate transported variable. Turbulence dissipation,  $\epsilon$ , is the rate at which turbulent kinetic energy is converted into thermal internal energy. (Ansys Fluent 12.0, 2009)

The RNG  $k-\epsilon$  model was derived from the statistical technique called renormalization group theory. The RNG model is closely related to the standard  $k-\epsilon$  model, except for the added refinements below:

- To increase the accuracy of rapidly strained flows, the RNG model has an extra term in the turbulent kinetic dissipation equation. (Ansys Fluent 12.0, 2009)

- The RNG model contains a term to explain how turbulence is affected by swirl. Thus, the accuracy for swirling flows is greatly improved. (Ansys Fluent 12.0, 2009)
- For turbulent Prandtl numbers, the RNG theory provides an analytical formula, while the standard k-ε model uses user-specified, constant values. (Ansys Fluent 12.0, 2009)

While the standard k-ε model is a high Reynolds number model, the RNG theory accounts for low Reynolds number situations by an analytically derived differential formula for the effective viscosity. Specific care should be taken on the treatment of the near-wall region to effectively make use of this feature. These characteristics render the RNG k-ε more tolerant for a larger range of flows.

$$\frac{\partial}{\partial t}(\rho k) + \frac{\partial y}{\partial x}(\rho k u_i) = \frac{\partial}{\partial x_j} \left[ \alpha_{kl} \mu_{eff} \frac{\partial k}{\partial x_j} \right] + G_k + G_b - \rho \varepsilon - Y_M + S_k$$

**(Equation 12: RNG-k)**

Where  $G_k$  is the turbulence generation term, it contains the products of the velocity gradients and is influenced by the turbulent viscosity.  $G_b$  is the turbulence kinetic energy due to buoyancy.  $Y_M$  adds to the fluctuating dilatation in compressible turbulence to the overall dissipation rate and  $S_k$  and  $S_\varepsilon$  user defined source terms.  $\alpha_k$  and  $\alpha_\varepsilon$  are the inverse Prandtl numbers.  $R_\varepsilon$  is the correction factor on  $k$  and  $\varepsilon$ , which is a major difference between the standard and the RNG k-ε Model, it makes it more responsive to the effects of rapid strain and streamline curvature and is computed by an additional formula. The remaining standard symbols are listed in the nomenclature.

$$\frac{\partial}{\partial t}(\rho \varepsilon) + \frac{\partial y}{\partial x_i}(\rho \varepsilon u_i) = \frac{\partial}{\partial x_j} \left[ \alpha_{\varepsilon l} \mu_{eff} \frac{\partial \varepsilon}{\partial x_j} \right] + C_{1\varepsilon} \frac{\varepsilon}{k} (G_k + C_{3\varepsilon} G_b) - C_{2\varepsilon} \rho \frac{\varepsilon^2}{k} - R_\varepsilon + S_\varepsilon$$

**(Equation 13: RNG-ε)**

Where  $C_{1\varepsilon} = 1.42$ ,  $C_{2\varepsilon} = 1.68$ ,  $C_{3\varepsilon} = 0.1$ ,  $\alpha_k = \alpha_\varepsilon = \alpha \approx 1.393$

The Eulerian multiphase model can be used, when the primary phase consists of either a liquid or a gas, with solid granular particles in the secondary phase. The kinetic theory is used in the Eulerian granular multiphase (EGM) model to predict the granular phase flows, which is typically very different from the primary liquid phase. (Ansys Fluent 12.0, 2009)

#### 5.1.1.4 Multiphase turbulence modelling

Multiphase fluid calculations are divided into two main groups namely separated and dispersed flow. The options available in the Fluent software for separated flow are the volume of fluid and the multi-fluid volume of fluid model. The two options available for dispersed flow, which is relevant for mixing tanks, are the Eulerian and the Lagrangian models. The Eulerian granular multiphase model was selected as the preferred model for simulating solids suspension in the stirred tanks. The Eulerian-granular model treats the solid phase as an additional continuous phase where additional interphase transport equations need to be applied to compute the solid-liquid interaction. The granular phase continuity and momentum equations are shown below. (Ansys Fluent 12.0, 2009)

$$\frac{\partial}{\partial t}(\alpha_s \rho_s) + \nabla(\alpha_s \rho_s \mathbf{u}_s) = \dot{m}_{fs}$$

**(Equation 14: Eulerian granular phase continuity equation)**

$$\frac{\partial}{\partial t}(\alpha_s \rho_s \vec{\mu}_s) + \nabla(\alpha_s \rho_s \vec{\mu}_s \vec{\mu}_s) = -\alpha_s \nabla p_f + \nabla \bar{\tau}_s + \sum_{s=1}^n (\vec{R}_{fs} + \dot{m}_{fs} \vec{\mu}_{fs}) + \vec{F}_s$$

(Equation 15: Eulerian granular phase momentum equation)

Granular phase momentum equations are shown on the left. The first term on the right of the equation is the fluid pressure, the second, the solid stress tensor, and the third, the phase interaction term. The pressure field is uniform for all phases. The solid stress takes into account the interaction between the solids, derived from the granular kinetic theory. The phase interaction term takes into account the interaction between the primary and secondary phase. Where  $\alpha_s$  is the solids volume fraction,  $\rho_s$  is the solids density,  $\vec{\mu}_s$  the time-averaged solids viscosity,  $\nabla \bar{\tau}_s$ ,  $p_f$  the fluid pressure, the solids stress tensor,  $\dot{m}_{fs}$  the mass transfer term.

### 5.1.1.5 Modified k- $\epsilon$ models

There are three different variations of this particular turbulence models in Fluent namely the mixture, dispersed and per phase functions. The mixture model is applicable when the primary and secondary phase densities are similar and there is no clear distinction between the primary and secondary phase. The per-phase model solves a complete set of PDE's for each phase and is therefore very computationally expensive. (Ansys Fluent 12.0, 2009)

The dispersed model was selected for this setup since the concentration of the secondary phase is dilute. In other words, the one phase is clearly the dominant phase and the other the secondary phase. In this case, the water is clearly the primary phase and the  $\text{CaCO}_3$  crystals the secondary. (Ansys Fluent 12.0, 2009)

#### 5.1.1.5.1 Dispersed Model

The dispersed turbulence model should be used when the liquid phase is controlling the process, and the secondary phase (particles) is dilute. Subsequently, the inter-particle collisions can be omitted, and the secondary phase behaviour is mainly influenced by the turbulence in the liquid phase. Therefore, the fluctuating quantities of the solids particles can be obtained from the averaged characteristics of the primary phase as well as the particle relaxation time and the interaction of the eddy currents of the particles. (Ansys Fluent 12.0, 2009)

The assumptions made by the dispersed model are listed below:

- The liquid phase turbulence is generated from the standard k- $\epsilon$  model coupled with additional terms to account for turbulent momentum transfer between the solid and the liquid phase. (Ansys Fluent 12.0, 2009)
- The dispersed phase turbulence quantities are computed from the Tchen theory, which predicts the dispersion of discrete particles in homogeneous turbulence. (Ansys Fluent 12.0, 2009)
- The interaction between the instantaneous distribution of the solid phase and the turbulent liquid in motion is added to the momentum exchange term. The additional term allows the dispersion of the solid phase transported by the liquid phase to be visualised. (Ansys Fluent 12.0, 2009)
- The dispersion of the solid phase in multiphase turbulent flows is affected by the choice of averaging process. Fluctuations in the phase volume fractions are created when using a two-step averaging process. If a phase-weighted average to account for turbulence is used in conjunction with the two-step averaging process, these

fluctuations are eliminated. Fluent incorporates phase weighted averaging, thus volume fraction fluctuations are not transferred into the continuity equations, allowing for more stable calculations. (Ansys Fluent 12.0, 2009)

Transport equation for the modified k-ε model,

$$\frac{D}{Dt}(\rho k) = \frac{\partial}{\partial x_j} \left[ \left( \mu + \frac{\mu_t}{\sigma_k} \right) \frac{\partial k}{\partial x_j} \right] + G_k - \rho \varepsilon$$

**(Equation 16: Turbulent kinetic energy)**

$$\frac{D}{Dt}(\rho \varepsilon) = \frac{\partial}{\partial x_j} \left[ \left( \mu + \frac{\mu_t}{\sigma_\varepsilon} \right) \frac{\partial \varepsilon}{\partial x_j} \right] + C_{\varepsilon 1} \frac{\varepsilon}{k} G_k - \rho C_{\varepsilon 2} \frac{\varepsilon^2}{k}$$

**(Equation 17: Kinetic energy dissipation rate)**

Where  $\mu_t$  is the eddy viscosity,  $\sigma_\varepsilon$  &  $\sigma_k$  is the turbulent Prandtl numbers,  $G_k$  the turbulent kinetic energy generated from the mean velocity gradients. The constants used in the above equations:  $C_\mu = 0.09$ ,  $C_{\varepsilon 1} = 1.44$ ,  $C_{\varepsilon 2} = 1.92$ ,  $\sigma_k = 1.0$ ,  $\sigma_\varepsilon = 1.3$ . The other symbols are listed in the nomenclature.

### 5.1.1.6 Drag models

The interphase momentum transfer is modelled via the drag function  $C_d$ . Fluent 14.5 have many drag functions pre-installed in its library; the ones significant to solid-liquid applications are mentioned below. The Wen Yu model was selected for these specific solids loading conditions. Although not as common as the Gidaspow and the Syamlal-Obrien models, the Fluent database recommends it for low solid loading applications. (Ansys Fluent 12.0, 2009). The fluid - solid exchange coefficient  $K_{st}$ , is given by the following equations.

I. Wen – Yu:

When the phase flow is dilute the Wen & Yu model is applicable, it was designed for when the volume fraction of the secondary phase is significantly lower than that of the primary phase.

$$K_{st} = \frac{3}{4} C_d \frac{\alpha_s \alpha_l \rho_l |\vec{v}_s - \vec{v}_l|}{d_s} \alpha_l^{-2.65}$$

**(Equation 18: Wen-Yu drag model)**

II. Gidaspow:

The Gidaspow model is recommended by Ansys Fluent Inc. 6.3 (2006) for dense fluidised beds.

$$K_{st} = 150 \frac{\alpha_s (1 - \alpha_l) \mu_l}{\alpha_l d_s^2} + 1.75 \frac{\alpha_s \rho_l |\vec{v}_s - \vec{v}_l|}{d_s}$$

**(Equation 19: Gidaspow drag model)**

III. Syamlal-Obrien:

The Syamlal-O'Brien fluid-solid drag model is recommended by Ansys Fluent Inc. 6.3 (2006) for use in combination with the Syamlal-O'Brien model for granular viscosity.

$$K_{st} = \frac{3}{4} C_d \frac{\alpha_s \alpha_l \rho_l |\vec{v}_s - \vec{v}_l|}{4 v_{r,s}^2 d_s} \left( \frac{Re_s}{v_{r,s}} \right) |\vec{v}_s - \vec{v}_l|$$

**(Equation 20: Syamlal-O'Brien drag model)**

Where,  $C_d$  is the drag coefficient,  $\alpha_l$  &  $\alpha_s$  the volume fraction for the liquid and solid phase,  $d_s$  is the average solid diameter,  $\vec{v}_s$  &  $\vec{v}_l$  the averaged phase velocities,  $v_{r,s}$  is the terminal velocity correlation for the solid phase. (Ansys Fluent 12.0, 2009)

### 5.1.1.7 Lift Force

The lift force is insignificant compared to the drag force, therefore, it is unnecessary to include it in this calculation since the phases do not separate quickly. (Ansys Fluent 12.0, 2009)

### 5.1.1.8 Turbulence interaction

Turbulence interaction is an important function of solid-liquid solutions. Turbulence is an important part of the development of single-phase flow structures and it is generally accepted as a major contributor to solid dispersion within the solution in agitated tanks. CFD simulations studied by other researchers, stressed the importance of turbulence-assisted solids dispersion in mechanically agitated tanks. The Simonin et al. formulation was used in this work for the computation of the turbulence interaction as suggested by Cockljat et al. (2006).

### 5.1.1.9 Turbulent dispersion

The contribution of the turbulent dispersion force should be included when the size of the eddy currents is larger than the particulate size, this function allows for the particulate to be transported and dispersed by the eddy currents. In all cases, it was computed using the Simonin formulation. The Ansys Fluent guideline suggests that the Simonin turbulent dissipation model is used in conjunction with the Simonin et al. turbulence interaction formulation for optimal predictions.

### 5.1.1.10 Modelling flows in a moving zone

Ansys FLUENT offers three methods to approach modelling flows in moving zones:

- Multiple reference frame (MRF) model
- The mixing plane model
- Sliding mesh (SM) method

In the MRF and the mixing plane model, a uniform flow field is assumed. The effect of the impeller on the baffles is estimated. The models are sufficient when the intermediate fluid volume is large and the impeller has a limited influence on the turbulence at the baffles or detailed analysis is not required.

The sliding mesh modelling approach assumes an unsteady flow field and the interaction is computed individually. When the baffles have a strong influence on the flow fields generated by the impeller or a detailed analysis is required the SM model is much more suitable for the application. However, since the SM model makes use of an unsteady numerical solution, the



computational expense is greatly increased compared to the MRF and mixing plane models. (Ansys Fluent 12.0, 2009)

The strategy applied to simulate the rotation of the impeller in this work for the modelling of the crystallizer tanks was the sliding mesh method. It was selected because of the importance of the baffles in the cylindrical crystallizers and the corners of the rectangular crystallizer tanks. The SM approach also handles the secondary flows produced by the impeller more effectively.

The sliding mesh is when two or more cell zones are created. Each cell zone should have at least one interface with the adjacent cell zone. The "Grid interface" is created where the two the respective interface zones meet. The cell zones will move relative to each other defined by the user input along the grid interfaces.

It is important in the sliding mesh model that the grid interface must be positioned so that it has fluid cells on both sides as shown in **Figure 24** below. When the simulation is activated, the cell zone of the inner fluid volume slide with respect to the cell zone of outer fluid volume along the grid interface created. The rotation is controlled by discrete time steps. It is not required that the nodes align as the inner fluid rotates when using the SM method. The fluid field is unsteady by nature, thus the time stepping technique is a necessity. (Ansys Fluent 12.0, 2009)

## 5.2 Geometry

Two individual models were designed in Autodesk Inventor. The assemblies included the individual parts with the "merge of parts" function disabled. The assemblies were exported from Inventor in step file format and imported into the geometry function on Workbench. In the geometry platform, the models were further defined by Boolean and slice operations in order to get all the zones and named selections necessary to prepare the models to be imported into the meshing platform.

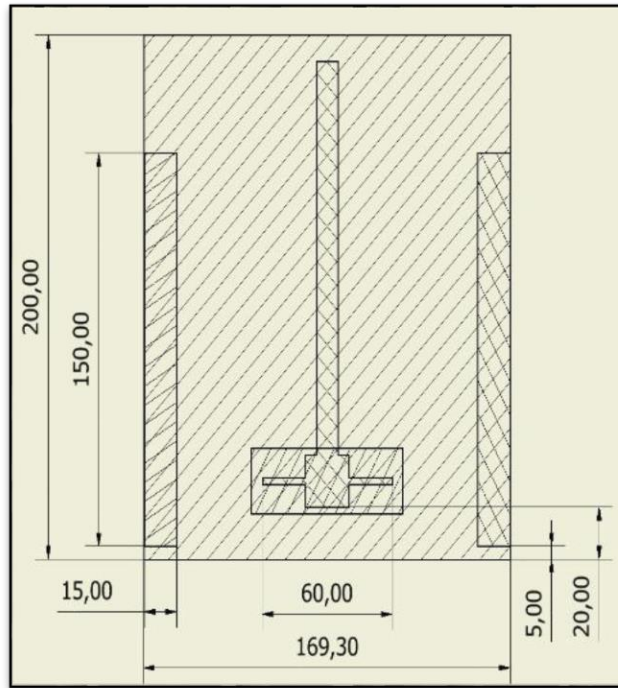
A Boolean subtraction operation was performed; first, the rotating volume and the baffles are subtracted from the fluid domain and then the impeller and the shaft are subtracted from the rotating fluid.

A slice operation was required on the outer surface of the rotating fluid separating the entire centre of the rotating volume from the outer fluid volume. Following the slice operation, four bodies were created in the workspace. The outer volumes were combined into a part as shown in **Figure 24** below. By dividing the models into multiple sections the areas not containing complex geometries could be simplified by using quadrilateral meshes and greatly reduce the cell count. Properties for both sections were manually set to a fluid, as Fluent does not adopt these settings automatically.

The geometry now had two single bodies, the outer stationary volume, and the inner rotating impeller volume. Consequently, a non-conformal interface was generated and allows the inner "impeller rotational volume" to rotate during the computational analysis.

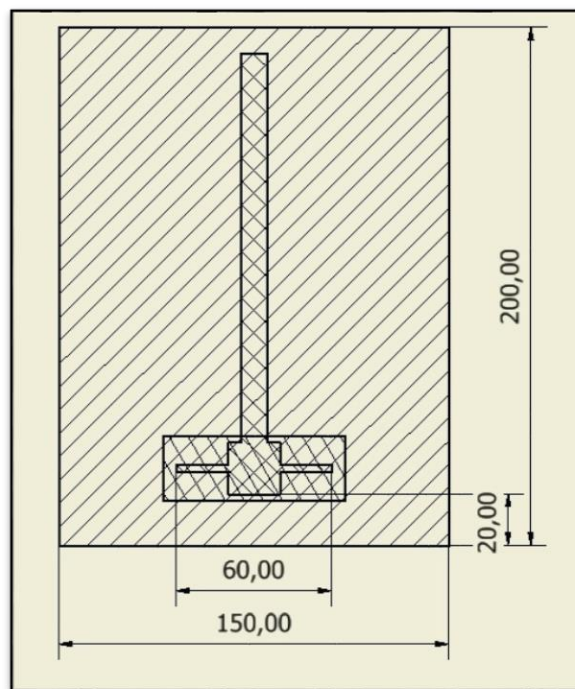
### 5.2.1 Dimensions

Referring to **Figure 19** below, a cylindrical tank with an inside diameter of  $T = 169.3$  mm was created. The fluid domain consisted of a fully baffled cylindrical tank with four 15 mm wide baffles circularly arrayed spaced ninety degrees apart. The height of the tank was set to 200 mm. Agitation was provided by a standard 45° PBT with a corresponding blade width of 10 mm and the overall impeller diameter of 60 mm. The distance between the bottom of the impeller and the bottom of the tank was fixed to 20 mm. The tanks used throughout this work had an approximate volume of 4.5 litres.



**Figure 19: Cylindrical mixing tank with baffles**

Similarly, referring to **Figure 20** below, a tank of 150 mm wide was created. The fluid domain consisted of a square volume without baffling. The height of the tank was kept at 200 mm. The impeller geometry and position were carried over from the previous setup. The rectangular tank below has the exact same volume as the cylindrical tank for an accurate comparison.



**Figure 20: Rectangular mixing tank without baffles**

### 5.2.2 Named selections

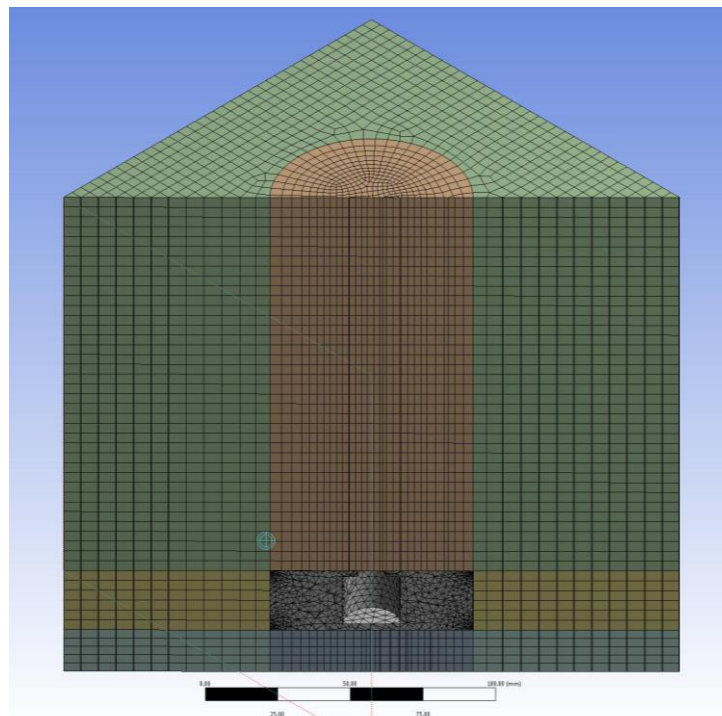
In order for Fluent to recognise the fluid domain(s), walls and interfaces, it was important that the named selections were clearly defined. Any named surface not recognized by the fluent library is automatically considered a wall. The outer surfaces of the model were therefore automatically assumed to be walls. If the surfaces were not correctly imported into Fluent the surface type could be corrected in the boundary conditions tab. However, if it was done correctly and Fluent recognises the named selections, very lengthy setup times can be avoided.

The top of the tank and the interface wall had to be manually modified as symmetry to allow for smooth flow patterns and eliminate unwanted interfaces in the flow fields.

The models consisted of the following named selections:

- Stationary zone
- Rotating zone
- Impeller
- Interface inner
- Interface outer
- Baffles (Cylindrical tank only)
- Tank top

The named selections and chosen technique for the meshing of the rectangular tank can be seen in **Figure 21** below.



**Figure 21: Rectangular mixing tank named selections**

## 5.3 Meshing

Meshing was found to be critical for realistic results. If the mesh quality is insufficient the results may be incorrect and misleading. Furthermore, if the mesh quality is not high enough it may cause difficulties with the convergence of the partial differential equations. The factors that should be taken into consideration are shown below.

### 5.3.1 Meshing quality

Poor quality meshing may influence:

- Setup time
- Computational expense
- False diffusion

#### 5.3.1.1 Setup time

Many engineering problems that are complex and difficult or not possible to solve analytically usually have very complex geometries. The creation of structured meshes utilising quadrilateral or hexahedral elements may be time-consuming and often impossible to solve. Therefore, using unstructured meshes like triangular or tetrahedral cells can greatly decrease the time expense for the setup. However, if the geometry is not very complex structured meshing may also be used without a great time loss. (Ansys Fluent 12.0, 2009)

#### 5.3.1.2 Computational expense

Triangular and tetrahedral meshes can be used to massively reduce the cell count when the geometries are complex or a large range of length scales are required, when compared to quadrilateral and hexahedral elements. Since, clustering of cells in specified areas in the flow field is possible when using triangular and tetrahedral meshes, structured quadrilateral and hexahedral meshes normally requires more cells in the fluid field, also in areas where they are not necessarily needed. In less complex geometries however, there are many advantages to using quadrilateral and hexahedral meshes. (Ansys Fluent 12.0, 2009)

Un-structured quadrilateral and hexahedral elements can be more economical for certain applications, where larger aspect ratios are needed. In large aspect ratio applications, the cell-skewness is affected by using triangular and tetrahedral cells as it reduces the quality of accuracy and convergence. Thus, if the fluid flow closely follows the shape of the geometry, e.g. flow in long thin pipe, quadrilateral/hexahedral should be used to create the high-aspect-ratio cells. Subsequently, the mesh can be generated using far less cells than when triangular or tetrahedral cells are used. (Ansys Fluent 12.0, 2009)

If a very detailed simulation is not a requirement, the entire fluid flow field mesh of tetrahedral cells can be modified to using only polyhedral mesh, which will reduce the cell count considerably. The coarser mesh will reduce the computational runtime and a converged solution could be reached sooner. (Ansys Fluent 12.0, 2009)

Depending on the application, Fluent recommends using the following meshes:

- Less complex geometries, quadrilateral or hexahedral meshes should be used.
- Moderately complex geometries, unstructured quadrilateral or hexahedral meshes should be used.

- Relatively high complexity geometries, triangular or tetrahedral meshes with prism layers should be used.
- High complexity geometries, use only triangular or tetrahedral meshes.

### 5.3.1.3 False diffusion

A common source of numerical error in multidimensional situations is computational diffusion (false diffusion). The term false diffusion is used to describe the instance when the diffusion is not real. However, in the flow calculation the effect of false diffusion is similar to an increase in the real diffusion coefficient.

In the list below the most common characteristics of false diffusion is shown:

- When actual diffusion is small, false diffusion will be the most noticeable when the simulation is convection dominated.
- To a limited extent, false diffusion is a phenomenon in all practical numerical schemes for solving fluid flow fields, it develops from truncation errors, which is the result of flow equations presented in discrete form.
- Ansys Fluent can incorporate the second-order and the MUSCL discretization scheme to limit the impact of false diffusion on the results of the simulation.
- The resolution of the mesh has an inverse effect on the amount of false diffusion, therefore by better refining the mesh, the chances of false diffusion are decreased.
- False diffusion can be minimised when the meshes are aligned with the flow. When selecting the mesh, the alignment is the most relevant to the selection. If triangular/tetrahedral meshes are being used, the flow will never be aligned with the mesh. If a quadrilateral/hexahedral mesh is being used, the flow might align with the mesh, but not for complex flows. It is only in simple flow, such as the flow through a long duct, in which quadrilateral/hexahedral mesh can be relied on to minimise numerical diffusion. In such situations, it is advantageous to use a quadrilateral/hexahedral mesh, since it is a superior solution with fewer cells than triangular or tetrahedral meshes.
- If a higher resolution for the gradient perpendicular to the wall is a requirement, prism layers with higher aspect ratios can be created near the walls. (Ansys Fluent 12.0, 2009)

### 5.3.1.4 Meshing of models

The models were adapted for CFD analysis, all walls, interfaces, bodies and volumes were named. Following the necessary preparations, the models were imported into the “Meshing workspace”. With the complex geometry of the impeller and the baffles, Fluent automatically adopts a non-uniformed tetrahedral meshing in the respective zones to capture the curvatures effectively. Care should be taken when using tetrahedral meshes, it may cause the cell skewness to become excessive and cause difficulties with the convergence of the solution. The meshing details of the two models are shown in **Table 2** below.

	<b>Rectangular</b>	<b>Cylindrical</b>
<b>Number of nodes</b>	53 048	61 225
<b>Number of elements</b>	56 932	233 882
<b>Max. Skewness</b>	0.599	0.77
<b>Min. orthogonal quality</b>	0.4	0.22
<b>Min. element quality</b>	0.36	0.316

**Table 2: Mesh quality report**

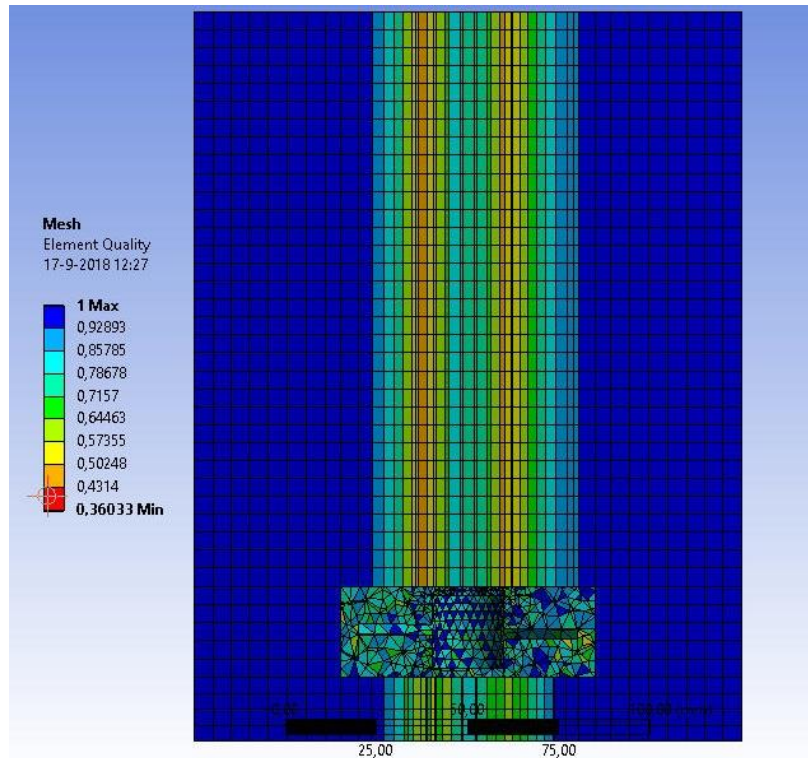


Figure 22: Rectangular tank mesh quality

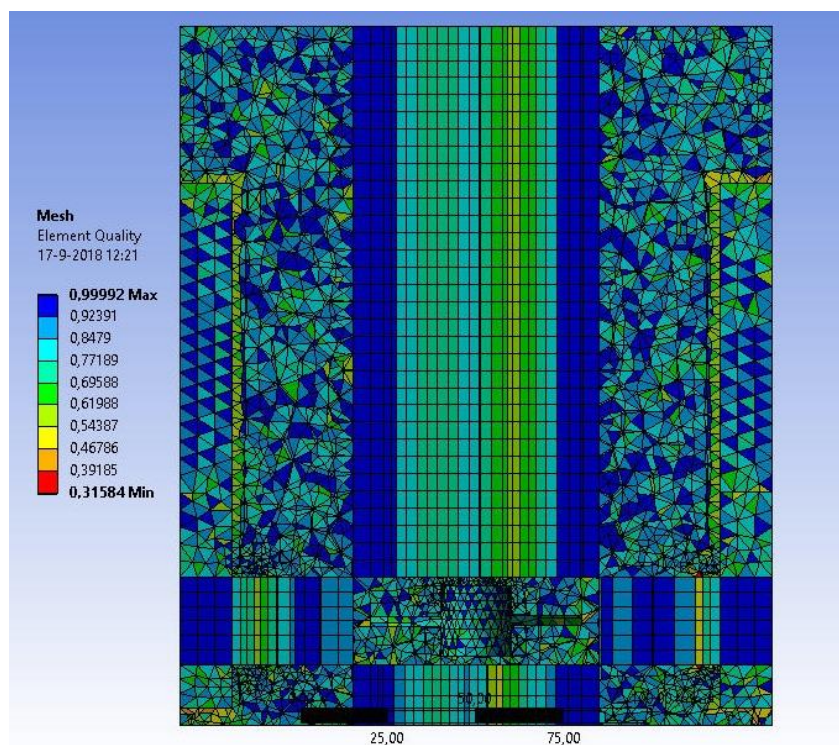


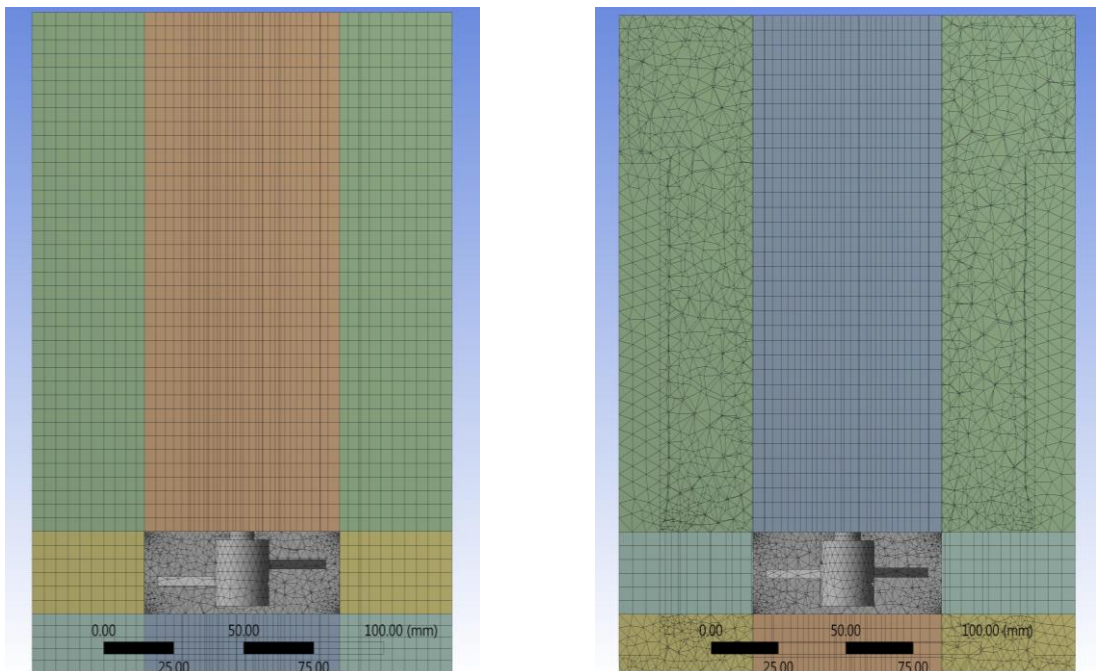
Figure 23: Cylindrical tank mesh quality

A section plane was created at  $XY=0$  to inspect the mesh. The Boolean technique used can be seen in **Figure 24** below. The rectangular tanks required less tetrahedral elements than the cylindrical tank since it is geometrically simpler by containing less components and curvatures. Subsequently, it was easier to obtain higher mesh qualities on the rectangular tanks.

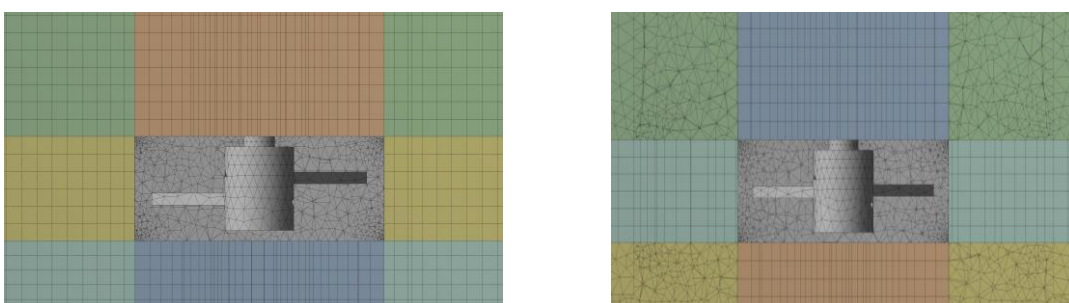
To further improve the mesh, the tanks could be “sliced” into multiple sections, the areas containing less complexities could then be simplified to using only quadrilateral elements. This greatly improved the mesh quality by reducing cell skewness and improving the aspect ratio, which could be closer to 1 in quadrilateral meshes.

The corners of the rotational volume however, were prone to false diffusion. A clear line was visible in the results between the stationary and rotational zones and a smooth transfer of properties could not be achieved. The first method of reducing this phenomenon, was to apply extensive manual input to area affected by the false diffusion.

Although, mesh quality had an impact on the false diffusion, it could not be identified as the sole reason thereof. Further improvements to mesh quality had no significant effect on the result and additional input was required in the solver to obtain the smooth transition of information through the meshing interface.



**Figure 24: Meshing (Section view, XY=0)**



**Figure 25: Meshing inflation (Section view, XY=0)**

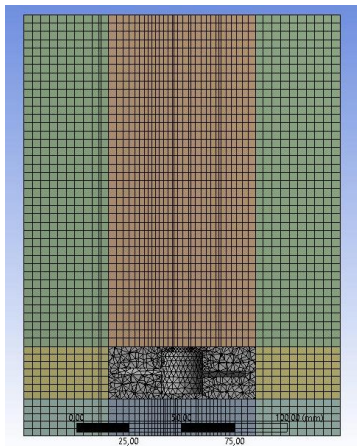
### 5.3.2 Effect of cell size

A grid dependency study was performed to ensure the solution would not be improved significantly with a higher quality meshing. It was seen that with very poor-quality meshing, which uses large unstructured meshing, the solutions were unstable and inconsistent. The mesh quality was improved to a point where no major changes were seen in the resulting flow fields.

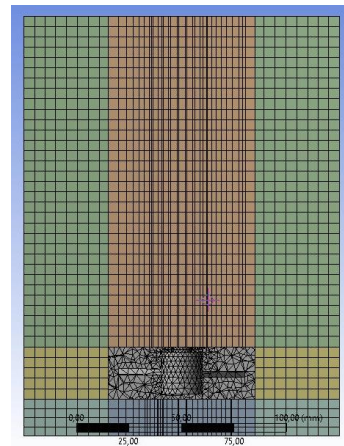
To evaluate the effect of the cell size on the solution, a control simulation were performed to ensure the results did not change significantly with finer meshing and more elements.

	<b>Cylindrical Actual</b>	<b>Cylindrical Control</b>	<b>Rectangular Actual</b>	<b>Rectangular Control</b>
<b>Number of nodes</b>	61 225	126 975	53 048	100 604
<b>Number of elements</b>	233 882	505 647	56 932	105 983
<b>Tetrahedral</b>	210 694	459 808	10 281	14 752
<b>Wedges</b>	256	488	388	1 132
<b>Pyramids</b>	3690	5 768	0	0
<b>Hexahedral</b>	19 242	39 583	46 263	90 099

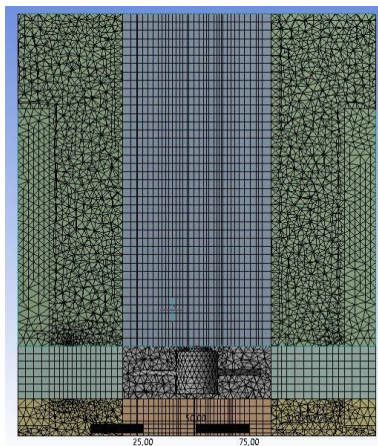
**Table 3: Refined mesh quality**



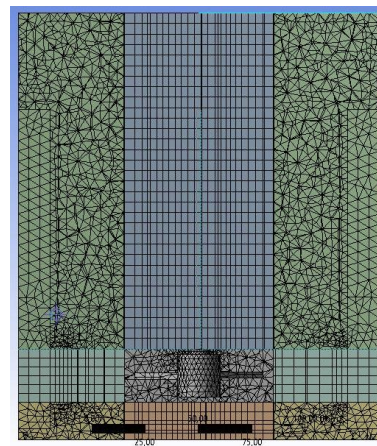
**Figure 26: Rectangular tank refined mesh**



**Figure 27: Rectangular tank actual mesh**



**Figure 28: Cylindrical tank refined mesh**



**Figure 29: Cylindrical tank actual mesh**

The contours of mean velocity and turbulent kinetic energy were compared in the figures below. It can be seen the refined meshing had minimal effect on the flow fields. Subsequently, the mesh of the tanks were considered satisfactory for the numerical comparison.



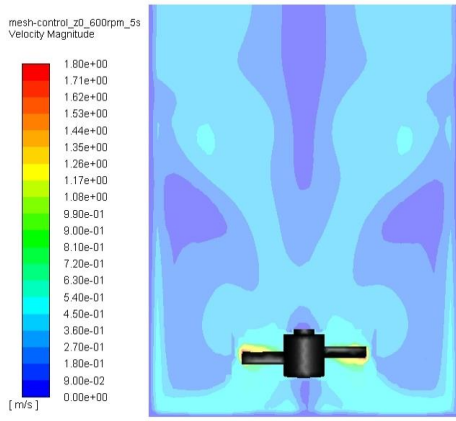


Figure 30: Rectangular tank mean vel. refined

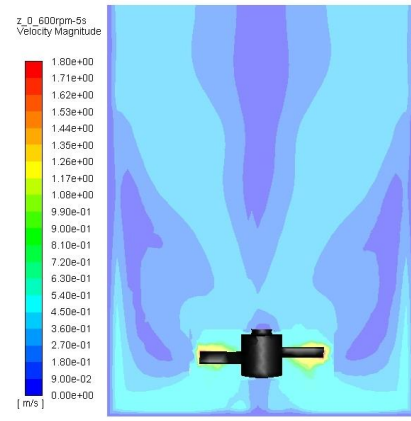


Figure 31: Rectangular tank mean vel. actual

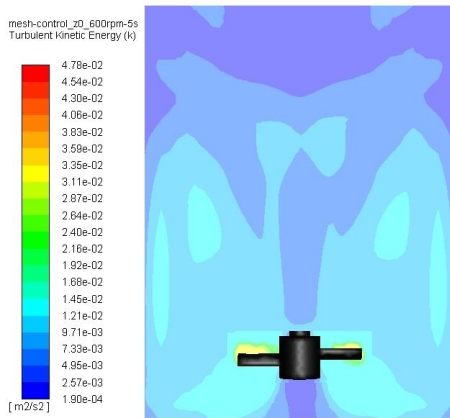


Figure 32: Rectangular tank turbulent kinetic energy refined

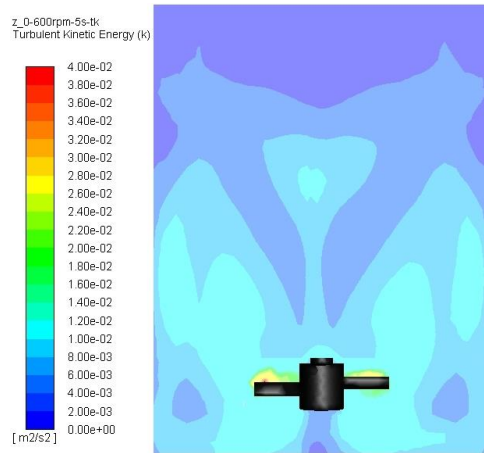


Figure 33: Rectangular tank turbulent kinetic energy actual

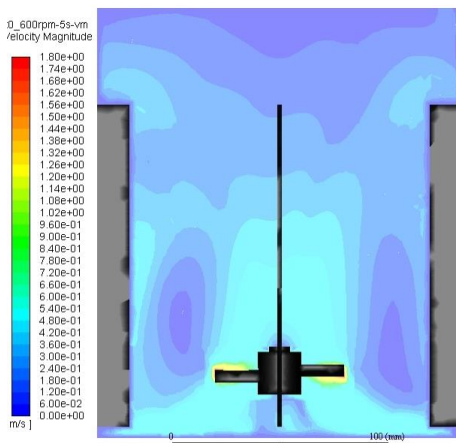


Figure 34: Cylindrical tank mean vel. refined

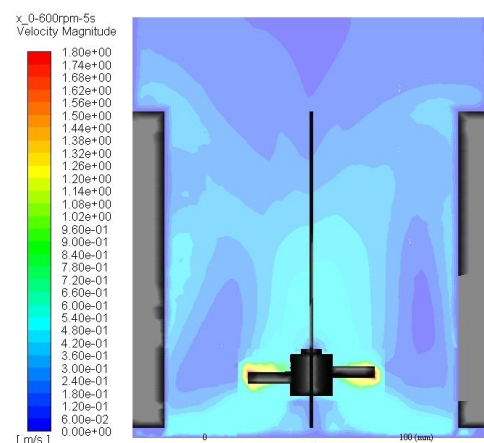
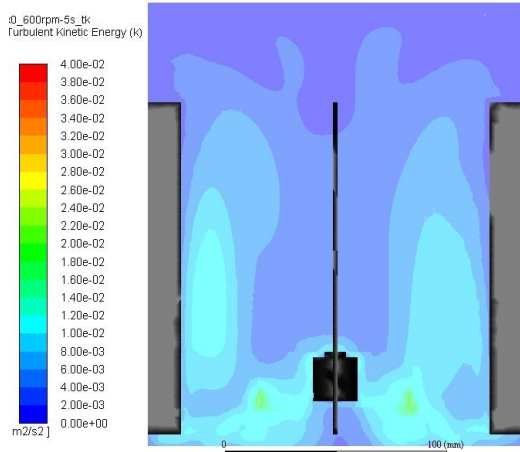
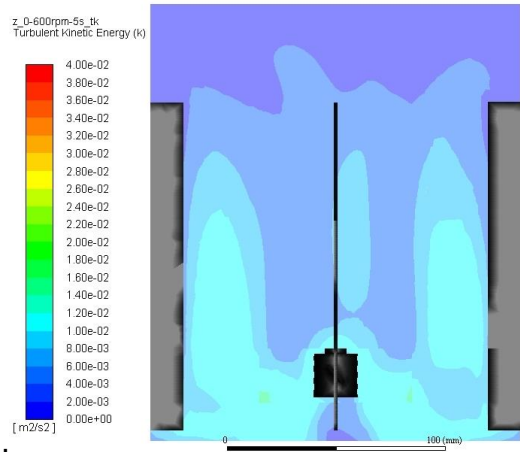


Figure 35: Cylindrical tank mean vel. actual



**Figure 36: Cylindrical tank turbulent kinetic energy refined**



**Figure 37: Cylindrical tank turbulent kinetic energy actual**

## 5.4 Fluent model setup

### 5.4.1 General

Ansys Fluent uses units rather than relying on the user to use consistent units that correspond to the dimensions that the geometry was specified in. The model unit of measure was millimetre. The pressure-based solver was selected with the absolute velocity formulation computed on a transient time solution. Gravity was set to  $-9.81 \text{ m}^2/\text{s}$ , which is in the negative Y direction of the model orientation.

### 5.4.2 Models

#### 5.4.2.1 Viscous model

The RNG  $k-\varepsilon$  (2-equation) was selected with standard wall treatment. The dispersed turbulence model was applicable in this case because there is a distinct primary and secondary phase and the material density ratio of the phases is approximately 2.2. Furthermore, the Stokes number will be less than one. The kinetic energy of the particles will not differ significantly from the liquid phase. (Ansys Fluent 12.0, 2009)

#### 5.4.2.2 Multiphase flow

As external agitation is applied to the packed bed in rest, the granular phase undergoes a phase change and is transformed intermittently from a stationary granular phase to a fluid in motion. To compute it accurately special treatment of the Eulerian-Granular multiphase model is applied. The EG model is the only model that includes solids pressure, which is a result of inelastic collisions between solid particles. Typically, for gasses defined by the kinetic theory, a Maxwellian velocity distribution can be assumed for the granular phase. It is impossible to fill the cavities between particles because of their shape and size, therefore the volume fraction of the granular phase can never reach one hundred percent. Fluent typically assumes a value of 0.6. For this reason the EGM model is more popular for a wide variety of simulations ranging from stirred tanks to fluidised bed flow patterns to flow in a riser. (Paul et al, 2004)

### 5.4.3 Materials and phases

Water in the liquid state was used as the primary phase for the models, for the secondary state mono-sized particles with the properties mimicking that of calcium carbonate ( $\text{CaCO}_3$ ) crystals were selected. The diameters of the crystals were measured experimentally by using a state of the art "laser particle size distribution analyser." The laser particle analyser passed the solution through an instrument that measures the size using laser diffraction in real time. The particulate sizes were grouped with the software and is converted into a "particle size distribution" graph from where the average particle size could be obtained.

Phase	Primary	Secondary
State	Liquid	Granular
Density ( $\text{kg/m}^3$ )	998.2	2200
Diameter (m)	Fluid	0.000150
Viscosity ( $\text{kg/m-s}$ )	0.001003	Syamlal-Obrien
Granular bulk viscosity ( $\text{kg/m-s}$ )	N/A	Lun-et al
Solids pressure	N/A	Lun-et al
Radial distribution	N/A	Lun-et al
Packing limit	Primary	0.63

Table 4: Material input

Phase interaction	
Drag	Wen Yu
Turbulent dispersion	Simonin
Turbulent interaction	Simonin et al.
Collisions constant	0.9

Table 5: Phase interaction models

#### 5.4.4 Cell Zone Conditions

The cell zone conditions were the set point for selecting the correct material state (fluid or solid) of the respective zones. The material state was fluid for both zones. The fluid selected, was “water liquid” from the FLUENT database. The model was operated at atmospheric pressure (101.325 kPa) with a correlating temperature of 293 K. The impeller was rotating at  $\pm 3^\circ$  per time step. The no-slip condition was used to the walls of the shaft, impeller, tank and the baffles.

The inner fluid volume was rotated with respect to the outer fluid. The rotational velocity was set to the desired velocity in rpm to the value obtained by the experimental setup, shown in **Table 6** below. In order to reverse the direction of the mesh motion, an absolute negative integer was used.

Zone	Stationary	Rotational
Rotational velocity (RPM)	0	600 and 750
Direction of Rotation	Y	Y

Table 6: Cell zone condition user input

#### 5.4.5 Boundary Conditions

Fluent automatically assumes all surfaces as walls, except for surfaces named specifically to the language that the program recognises. The baffles and the impeller were kept as no-slip walls and the interface between the rotating volume and the stationary volume is automatically recognised as an interface. The only added user input needed when the meshing is done correctly is to alter the tank top to a symmetrical surface, which acts as an extension of the tank, with drag on this surface not taken into account. In reality, the top of the tank is open to atmosphere. Therefore, symmetry was applied to the surface since the calculation cannot be computed without all boundaries in place.

#### 5.4.6 Interface

A meshing interface was created on the outer surface of the rotating volume. Similarly, on the inner surface of the stationary volume, the inner and outer interface zones were joined to form the grid interface. The interface allows the impeller to rotate freely from the stationary/outer volume by using the sliding mesh method. The turbulent flow properties are transferred through the mesh interface, unlike a wall and therefore, care should be taken to change the interface wall from a wall to symmetry.

#### 5.4.7 Solution initialization

The fluid region must be adapted to allow for the solids to be included in the mixture. The hybrid function was used for the initialization. After the completion of the initialization, the solids concentration was set to a specific height in the flow field. For all cases, the tanks were initially loaded with a 5% w/w solution, which equated to a 10 mm loading. The initial solids loading conditions are shown in **Figure 38** below.

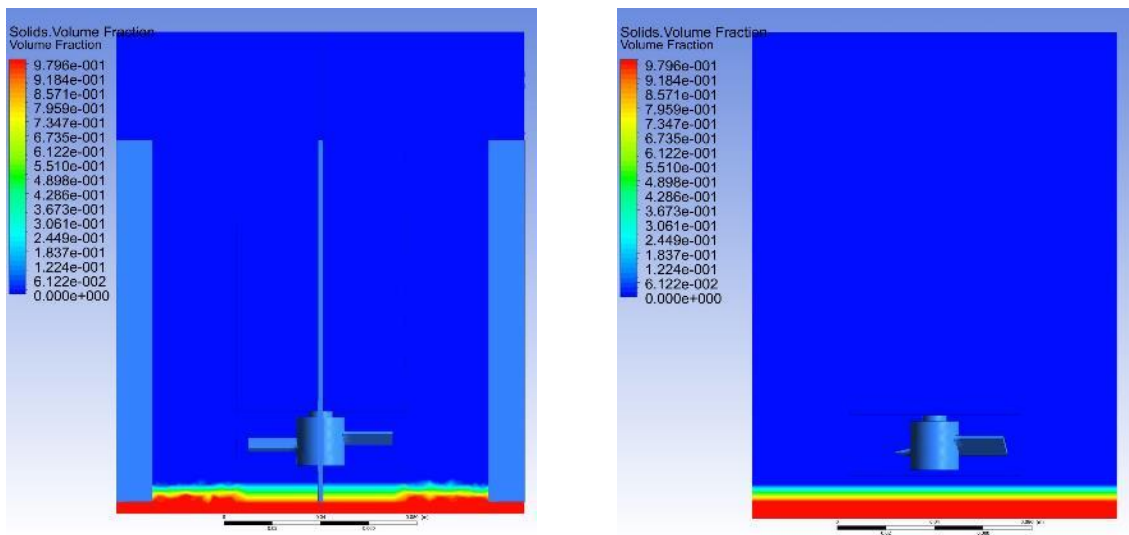


Figure 38: Solids loading (Section, XY=0)

#### 5.4.8 Solution methods and the calculation

The fixed time stepping method was selected for the calculation in order to reduce computational expense. The time step was carefully selected to ensure the mesh reform was not too significant and force the calculation into false diffusion. 0.0025 seconds was selected for each time step with 20 iterations per time step. The convergence value set for all parameters was  $1 \times 10^{-6}$ . Because of the fixed time stepping method convergence was never met because of the continuously reforming mesh, therefore the calculation was set to calculate for 2000-time steps which amounted to five seconds of actual mixing time. The transient three dimensional solution provided a time accurate solution.

From the experimental setup, it was determined that the rectangular mixing tanks should be operated between 600 – 750 rpm for sufficient solids suspension. Therefore, two separate cases were simulated for each type of mixing tank. In the first case the rectangular and cylindrical tanks were simulated at an impeller rotational velocity of 600 rpm. For the second case, the mixing tanks were simulated with an impeller rotational velocity of 750 rpm.

The solution method along with the appropriate meshing were found to be essential for realistic results. When using the sliding mesh approach, the mesh interface size should be carefully selected as it affects the time step size directly. If the meshing is refined the time step should be modified accordingly, i.e. when the element size is reduced the time step should be reduced as well. If the time step does not align with the interface element size, false diffusion is clearly visible on the top and bottom corners of the rotational volume. Therefore, the time step size should always be less than the element size when using the sliding mesh method, as information is transferred back and forth between the cells by the solver in order to approximate the face values of each element.

It was found that different solver schemes did not have a substantial effect on the mass and momentum solutions. However, the QUICK solver were found to be the most accurate in predicting the solid suspension in the tank. Higher order discretization schemes were needed to calculate the face values of the elements. In lower order methods the face value is taken as an average of the central value of the cell. The higher order interpolation methods incorporates multidimensional Taylor expansions to better approximate the gradients of the face and cell centred values of the upstream cells. This led to improved results of the solid suspension in the tanks.

Scheme	Coupled
Gradient	Least squares based
Momentum	Second order upwind
Volume Fraction	QUICK
Turbulent kinetic energy	Second order upwind
Turbulent dissipation rate	Second order upwind
Transient formulation	Bounded Second order implicit

**Table 7: Solution methods**

## CHAPTER 6: Results and discussions

The hydrodynamics in stirred mixing tanks are complex, turbulent and three-dimensional. The cases were studied three-dimensionally using the unsteady  $k - \epsilon$  solver. The sliding mesh (SM) strategy was applied to compute the transient solution in the stirred mixing tanks.

### 6.1 CFD vs experimental results

#### 6.1.1 Simulations 600 RPM

Below the experimental results are compared to the results of the CFD, the results from the experiment showed very good agreement with the results of the CFD in terms of the off-bottom suspension and cloud height throughout the experiment. The differences in the results can be prescribed to the fact that the particles were 150 micron mono sized particles in the simulations and in reality the particles have been sieved by a 150 micron sieve only. Therefore, it has an absolute maximum size of 150 micron but the granular phase of the experiment also contained smaller particles which were suspended more easily. The images of the experiment were taken from outside the tanks as shown in **Figure 39** below. It was therefore compared to same position in the simulations which is on the outer surface at  $x = 75\text{mm}$ .

At fifteen seconds the flow field stabilises in the experiment. It is seen that after fifteen seconds the accuracy of the CFD simulation deteriorates. In the author's opinion, it is the result of the selected models no being able to handle strong swirling flows accurately. The results of were compared at two second intervals.

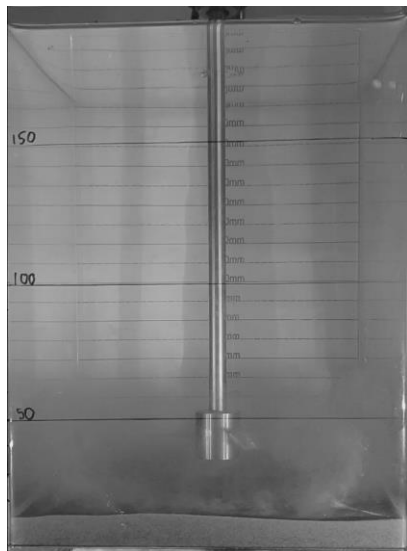


Figure 39: Experiment - 0s

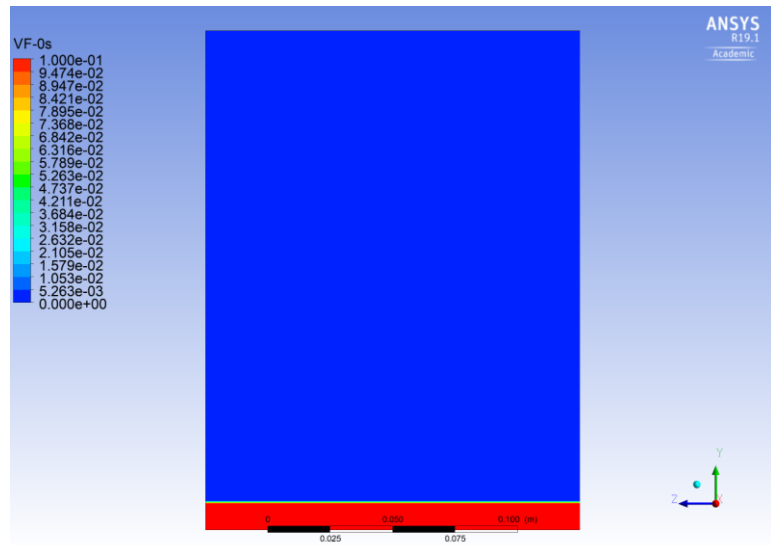


Figure 40: CFD 600 RPM - 0s

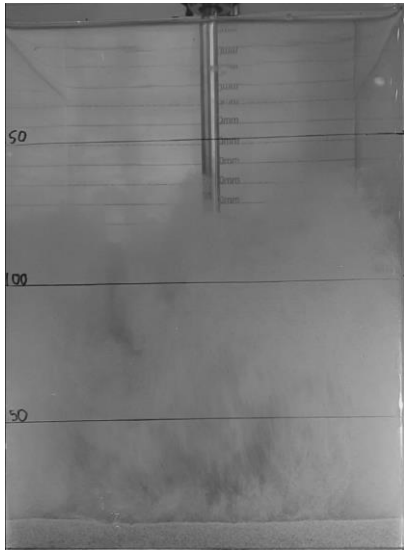


Figure 41: Experiment - 2s

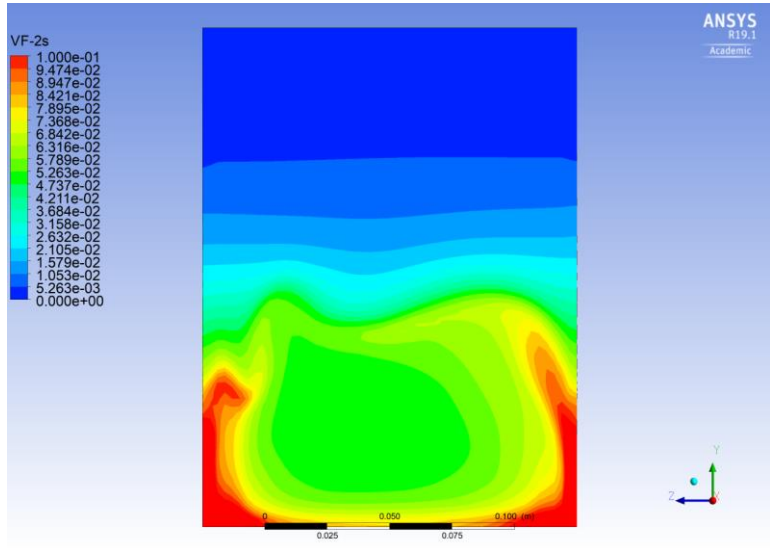


Figure 42: CFD 600 RPM – 2s

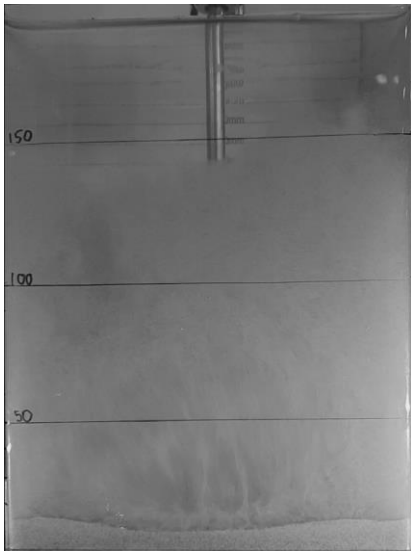


Figure 43: Experiment – 4s

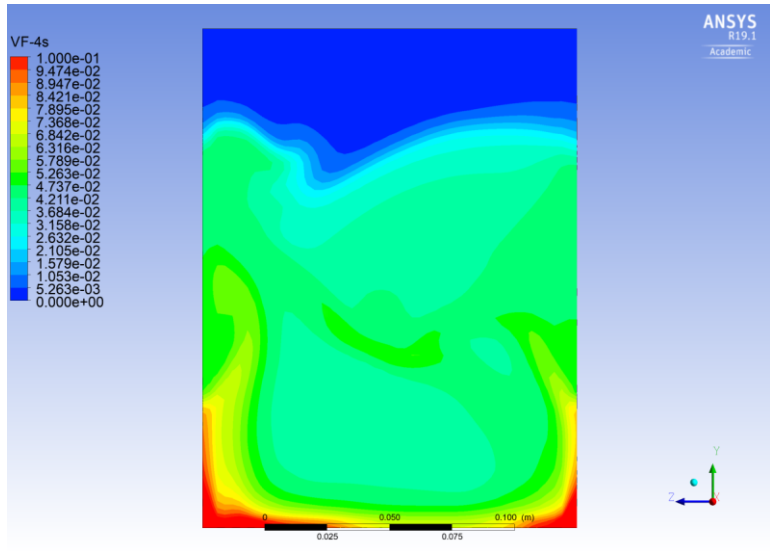


Figure 44: CFD 600 RPM – 4s

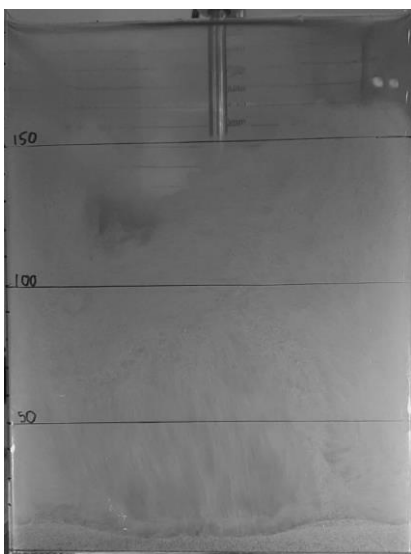


Figure 45: Experiment – 6s

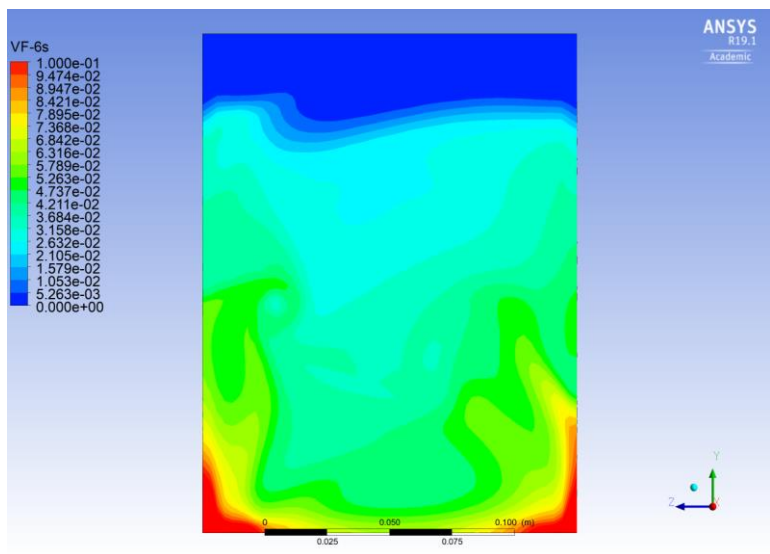


Figure 46: CFD 600 RPM – 6s



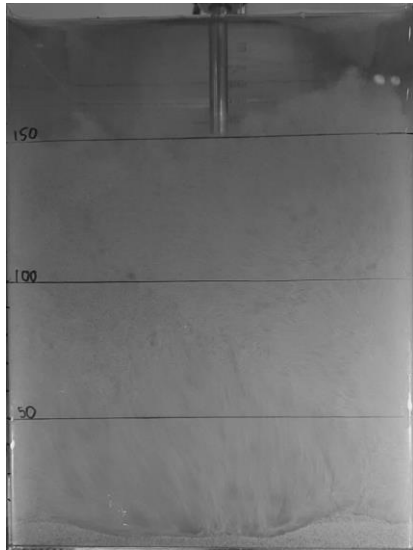


Figure 47: Experiment – 8s

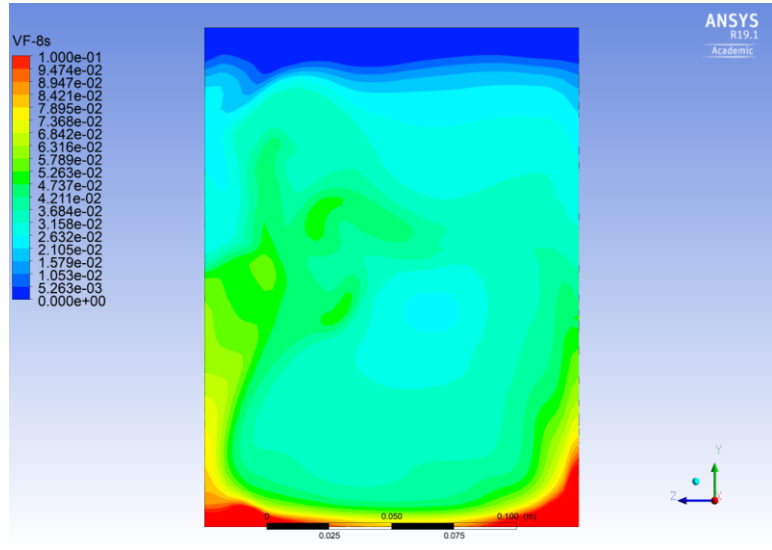


Figure 48: CFD 600 RPM – 8s

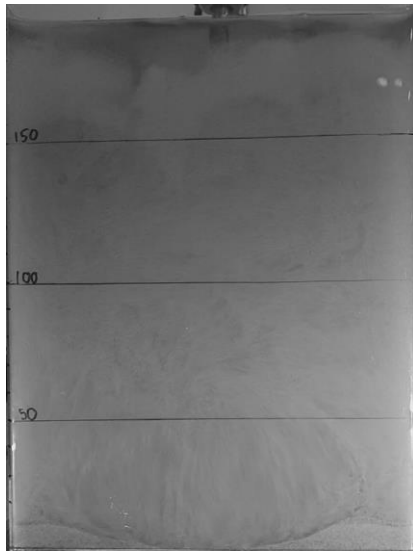


Figure 49: Experiment – 10s

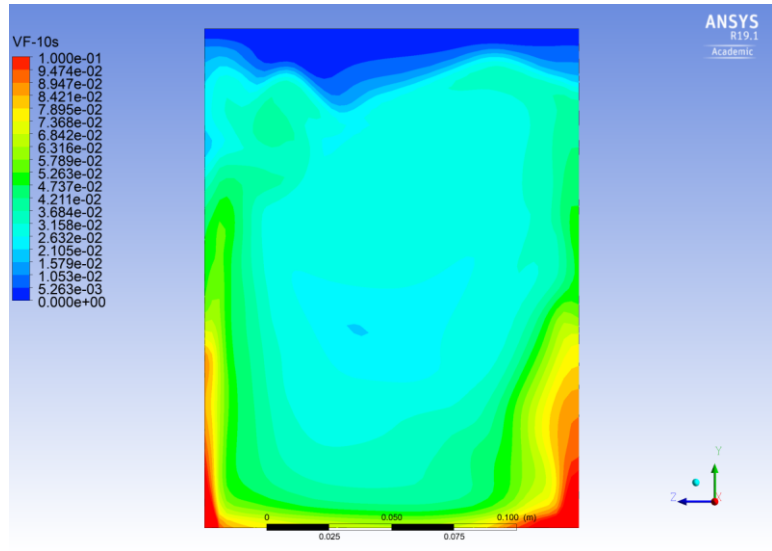


Figure 50: CFD 600 RPM – 10s

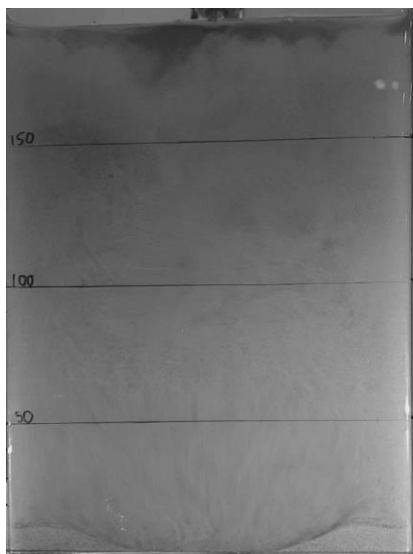


Figure 51: Experiment – 12s

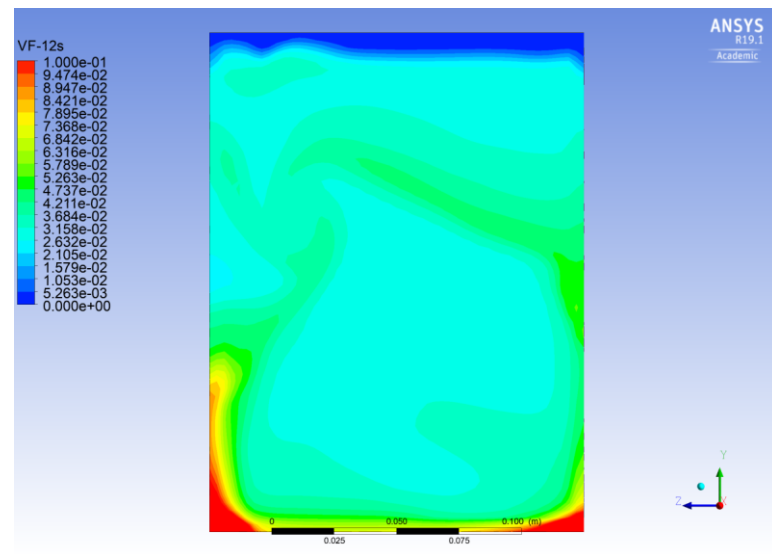


Figure 52: CFD 600 RPM – 12s

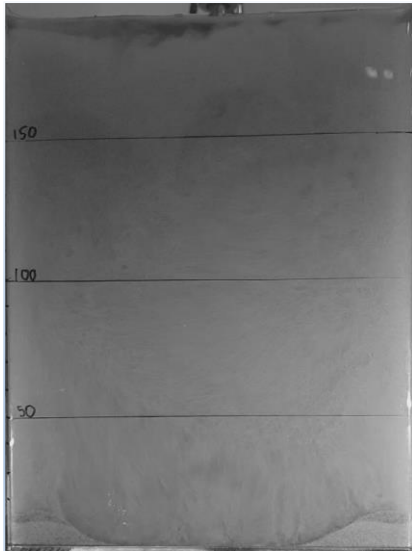


Figure 53: Experiment – 15s

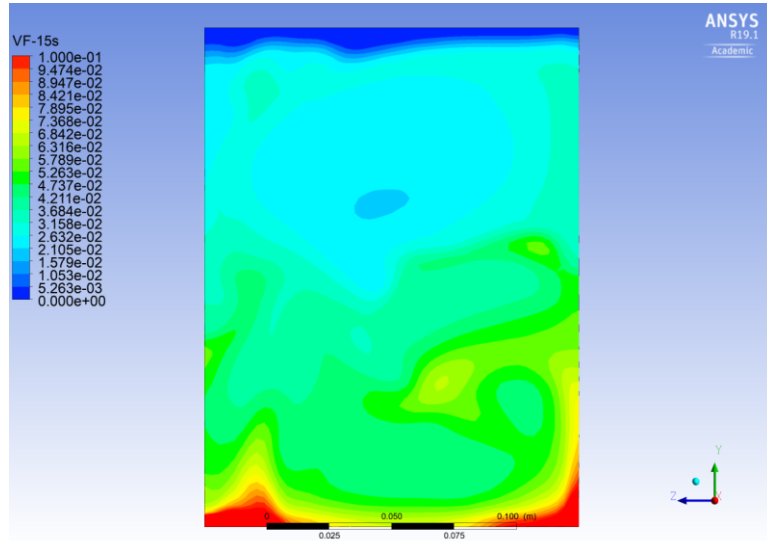


Figure 54: CFD 600 RPM – 15s

In order to extract meaningful results from the raw data it had to be further processed. Autodesk AutoCAD was used to create 1:1 scale models of the captured images. The images were superimposed to accurately measure and compare the CFD to the experimental cloud height. In the figures below the superimposed data can be seen.

The simulation predicted the solid suspension gradient on the bottom plane of the tank with reasonable results. Furthermore, the CFD captured the development of the cloud height very well. The shape of the cloud at the top of the suspension were also captured with surprising accuracy as seen in the figures above.

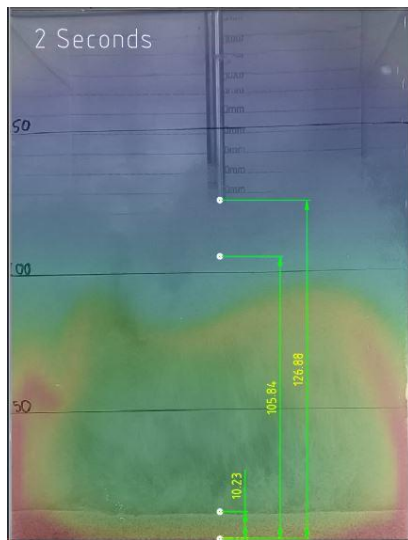


Figure 55: Experiment vs CFD – 2s

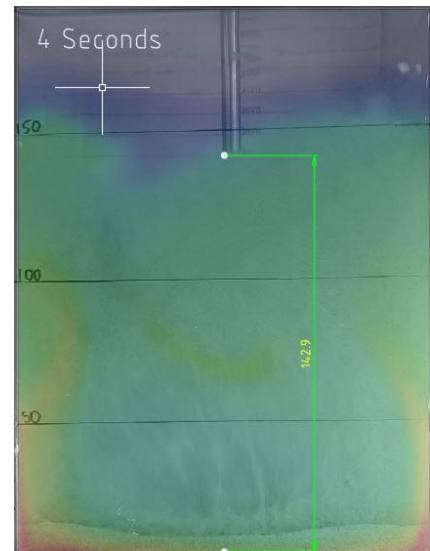


Figure 56: Experiment vs CFD – 4s

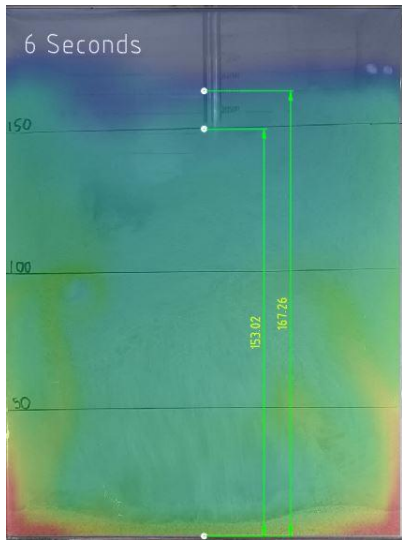


Figure 57: Experiment vs CFD – 6s

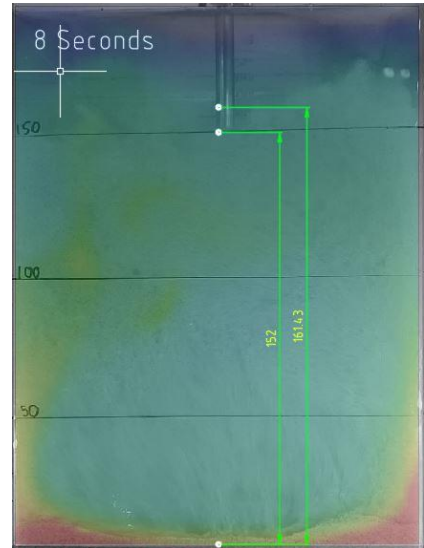


Figure 58: Experiment vs CFD – 8s

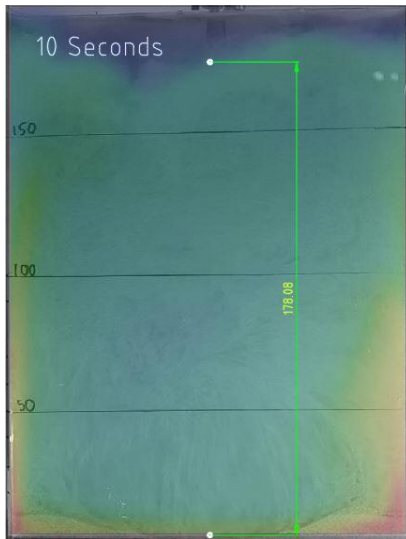


Figure 59: Experiment vs CFD – 10s

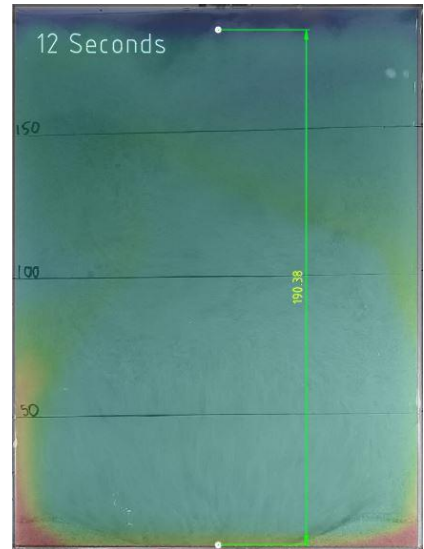


Figure 60: Experiment vs CFD – 12s

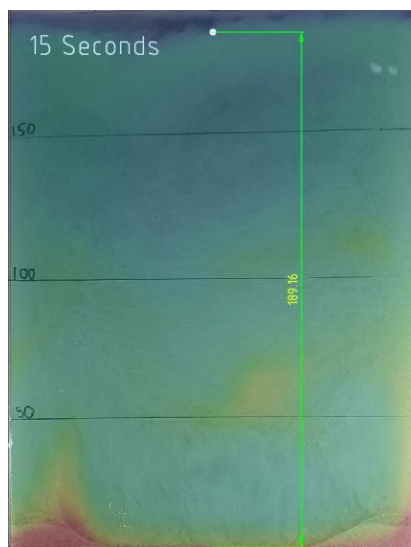
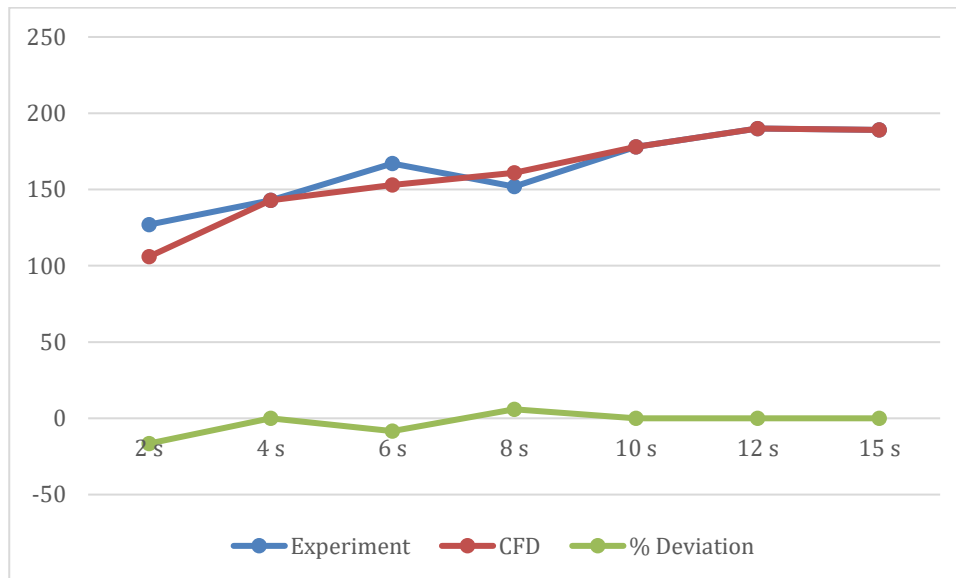


Figure 61: Experiment vs CFD – 15s

The superimposed images were used to accurately measure the deviation between the CFD and the experiment. The recorded data is shown in **Table 7** and **Graph 1** below. Overall the CFD simulation agrees very well with the experiment. The CFD trend was more gradual, whereas the results from the experiment were more irregular.

Time	Experiment (mm)	CFD (mm)	% Deviation
2 s	127	106	-16.5
4 s	143	143	0.0
6 s	167	153	-8.4
8 s	152	161	5.9
10 s	178	178	0
12 s	190	190	0
15 s	189	189	0

**Table 7: CFD vs experimental results (600 RPM)**



**Graph 1: CFD vs experimental results (600 rpm)**

The results of the CFD compared very well to the experimental data regardless of the experimental error. Since the largest particles are the heaviest, they will be the first to settle and the last to be suspended. The particles in the experiment have a maximum absolute size of 150 micron (as in the CFD simulations) excluding experimental error, typically around 5%. In this case the maximum error as a result of parallax was less than 2.5%, taking into account all other errors, 5% is a reasonable assumption for this specific case.

It can be seen in **Graph 1** above that the CFD under predicted the cloud height at two seconds, as noted by other researchers the initial data of a transient solution are usually disregarded as the solvers are not stable yet. At four seconds the data of the CFD matches the experiment with negligible deviance. At six seconds the cloud height is over predicted. During the final stages, from eight to fifteen seconds at a rotational velocity of 600 revolutions per minute, the experiment aligns very well with the CFD results.

In terms of off-bottom suspension, the CFD shows the particle suspension currents very well. It is clear from the flow fields above that the corners of the tank were responsible for the bulk of the solids suspension.

## 6.1.2 Simulation 750 RPM

To validate the findings of the 600 rpm the simulation was performed at 750 rpm as well. It was again seen that solids were suspended more aggressively in the CFD simulations initially than in reality. This could be prescribed to the more densely packed bed resulting from the finer particles also contained in the experiment and not in the CFD.

At four seconds the cloud height is noticeably over predicted, the accuracy shows improvement after five seconds and from six seconds towards the end of the simulation the CFD aligns very well with the experiment.

The final result of the experiment performed at 750 revolutions per minute after fifteen seconds can be seen in **Figure 62**, **Figure 63** and **Figure 64**. The rest of the results of the 750 rpm experiment can be found in **Appendix C**. As mentioned earlier, it is important to select the correct time step size. The time step size was reduced to 0.002 for the simulation at 750 rpm to ensure the mesh reform ratio remains the same as in the 600 rpm simulations.

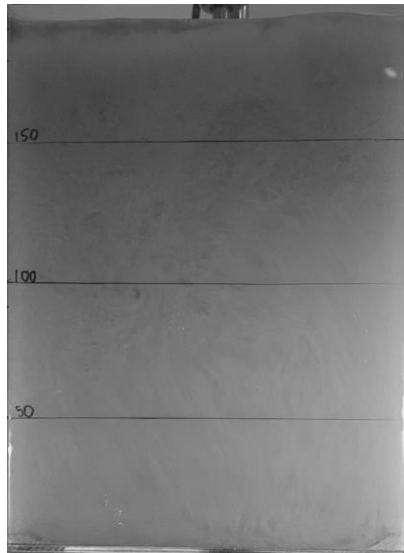


Figure 62: Experiment - 15s

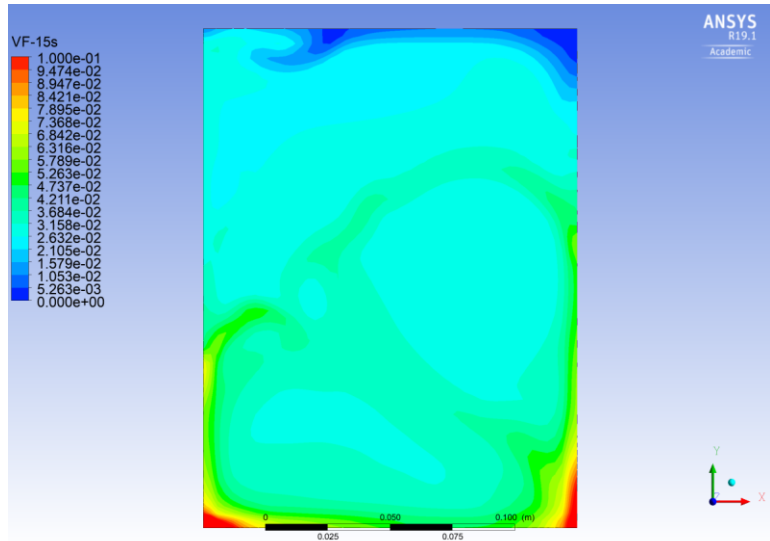


Figure 63: CFD 750 RPM – 15s

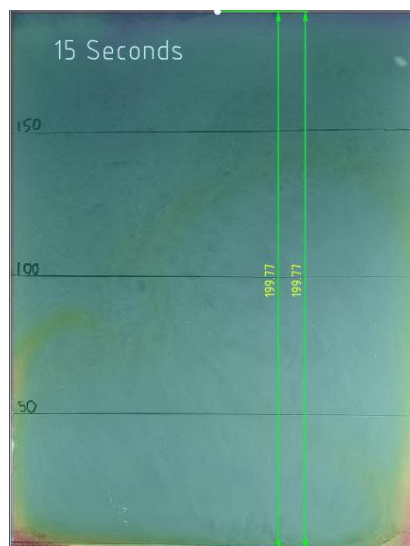
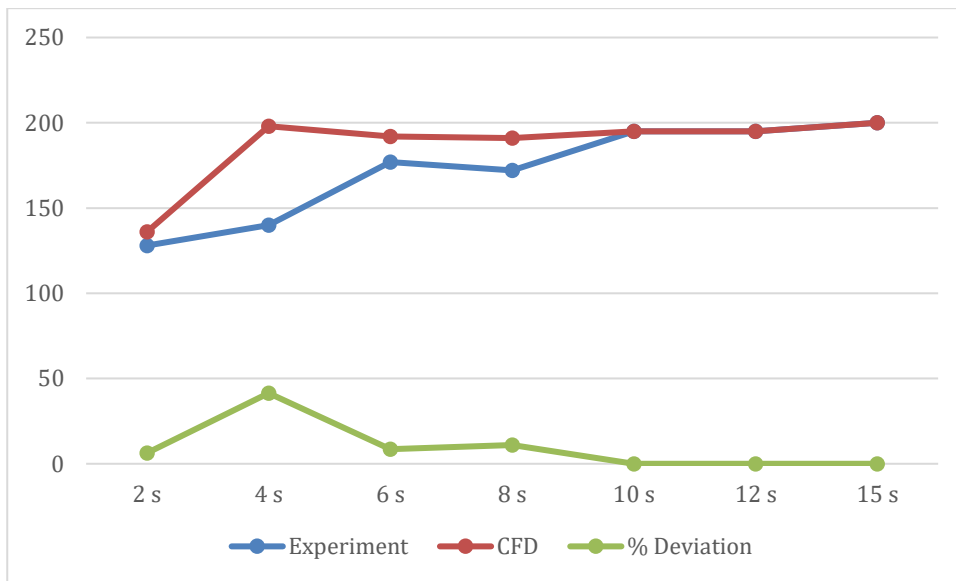


Figure 64: Experiment vs CFD – 15s

Time	Experiment (mm)	CFD (mm)	% Deviation
2 s	128	136	6.3
4 s	140	198	41.4
6 s	177	192	8.5
8 s	172	191	11
10 s	195	195	0
12 s	195	195	0
15 s	200	200	0

**Table 8: CFD vs experimental results (750 RPM)**



**Graph 2: CFD vs experimental results (750 rpm)**

### 6.1.3 Experimental findings

The following conclusions could be drawn from the experiment:

- The corners of the tank were effective in preventing rotational swirl at moderately low impeller velocities.
- The accumulation of solids was evident in the bottom corners.
- Highly turbulent flows were seen in the fluid domain.
- The non-uniform particles of the experiment had a minimal effect on the prediction of the cloud height.
- The Gidaspow and the Syamlal-O'Brien drag models provided poor results for the off-bottom suspension in the corners of the rectangular tank.
- The Wen-YU drag formulation along with Simonin turbulent interaction and dispersion models proved effective in capturing the off bottom suspension and cloud height in comparison with the experiment.
- The use of the QUICK formulation was required to compute realistic results for the volume fraction calculation.
- First order upwind schemes were not able to compute stable values for the momentum and turbulence equations.
- Time step size was crucial for stable calculations.
- The sliding mesh method was computationally expensive.
- The CFD simulation could accurately predict the cloud height at 600 and 750 revolutions per minute once the calculation had stabilized.

Given that through careful model selection and meshing we were able to produce numerical results that, in the aspects considered to be important for this analysis, had the same characteristics as the experimental results, it can be concluded that the CFD simulations can effectively predict particle behaviour and thus provide a useful comparison of the rectangular versus cylindrical tank.

## 6.2 CFD comparison of the rectangular vs round mixing tank

The CFD simulations were found to be highly computational expensive. To reduce the simulation time the tanks were compared at the following conditions:

- 5 seconds simulation time
- 0.0025 time step size
- 600 rpm

The results of the 600 rpm and 750 rpm were similar and therefore, deemed unnecessary to include the results of the 750 rpm for the CFD comparison. At five seconds the flow fields were completely developed throughout the entire domain of the cylindrical tank. Subsequently, it was considered to be the earliest rounded time for the comparison.

The model orientation used in both scenarios are shown below. Y was selected as the vertical vector, with X & Z being the horizontal vectors.

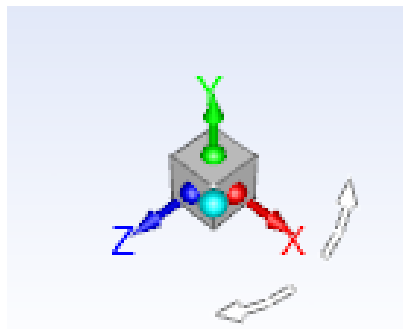


Figure 65: Model orientation

### 6.2.1 Mean velocity

The velocities in the flow field provide valuable insight into the macromixing taking place inside the agitated mixing tanks. As shown in **Figure 66** and **Figure 67** the velocity generated seems comparable within the tanks. It will be shown in the following sections that although the flow fields of mean velocity seem comparable, it developed completely differently with respect to axial, radial and tangential velocities.

The highest velocities were in both cases near the impeller tip, the velocities were in line with the theoretical maximum linear velocity of 1.88 m/s, calculated at 30 millimetres from the centre and an angular velocity of 600 rpm.



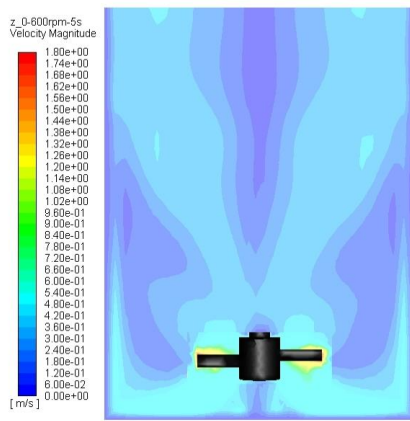


Figure 66: Rectangular mean vel. Z=0

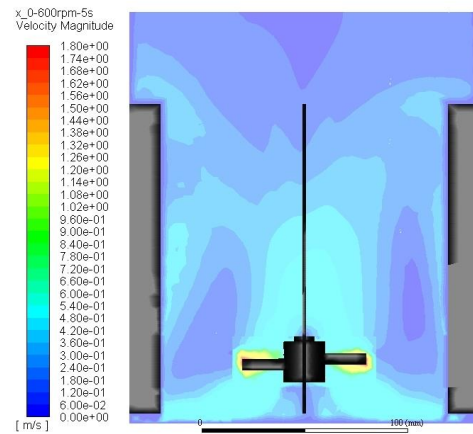


Figure 67: Cylindrical mean vel. X=0

A particular area of focus was at the bottom of the tank, since the bottom of the tank is flat, it was expected the bottom corners of the rectangular tank will show weak velocity magnitudes as seen in the experiment. It is clear from **Figure 67** that bottom corner of the cylindrical tank also displays a region of weak velocity near the bottom walls.

To investigate the mean velocity in the bottom corners of the rectangular tank further, a horizontal surface was created with a one millimeter offset from the bottom. It can clearly be seen from **Figure 68**, that the mean velocity were weak in the corners and in fair agreement with the experimental results.

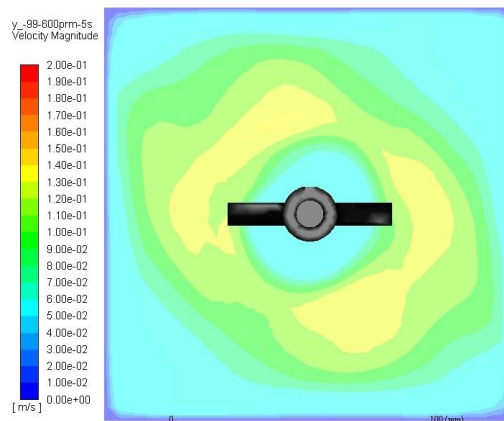


Figure 68: Rectangular mean vel. Y=-99

## 6.2.2 Axial velocity

Axial upflow velocities are an important aspect in the suspension of solids. It is the main means of transporting the packed granular phase into the secondary phase. Therefore, higher upflow velocities are generally desired for improving solid suspension.

The red-yellow regions indicate the highest up flow velocities. The blue-green area near the impeller indicates the highest down pumping velocities. The fluid circulates in loops from the axial down-pumping impeller to the bottom of the tank into the up flow stream, which loops again depending on the length of the circulation loops forming and ultimately flowing back towards the impeller. Larger circulation loops allow for better solid suspension in the mixing tanks.

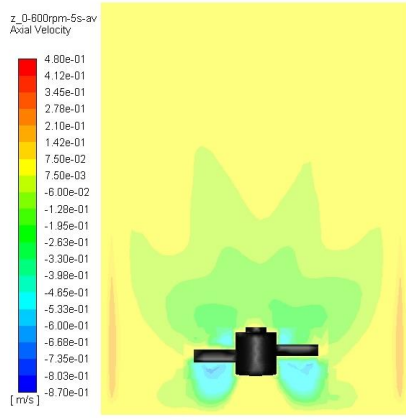


Figure 69: Rectangular axial vel. Z=0

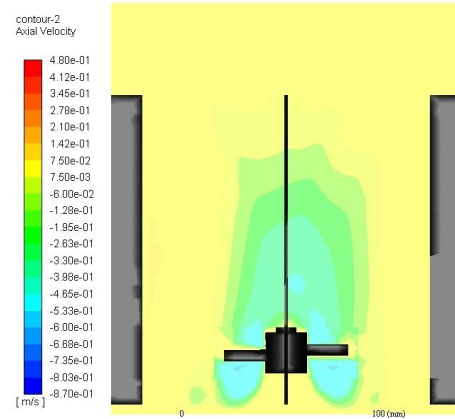


Figure 70: Cylindrical axial vel. X=0

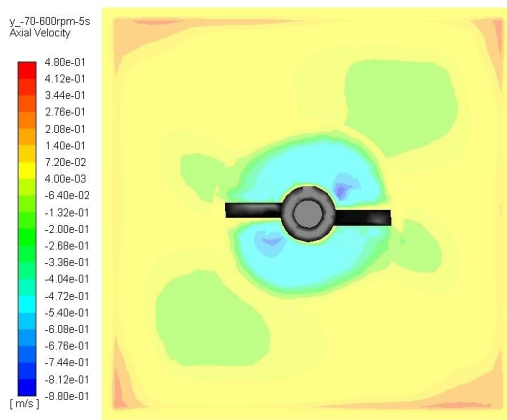


Figure 71: Rectangular axial vel. Y=-70

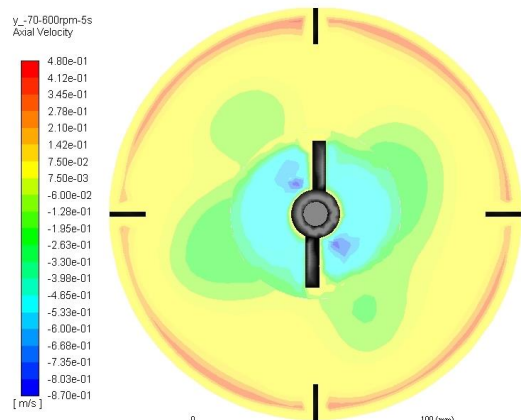


Figure 72: Cylindrical axial vel. Y=-70

It can be seen in the figures above that as expected the corners of the rectangular tank reached the maximum upflow velocity, whereas the upflow velocity in the cylindrical tank was much more evenly distributed on the walls between the baffling. It was also seen that the corners of the tank do act as baffling but are not as effective as baffling in converting the energy provided by the impeller into axial velocity. The maximum up and down velocities are shown in **Table 9** below.

	Direction	Max. Axial vel. (m/s)
Rectangular tank	Y +	0.48
Rectangular tank	Y -	0.87
Cylindrical tank	Y +	0.38
Cylindrical tank	Y -	0.88

Table 9: Axial velocities

### 6.2.3 Radial velocity

Moderate radial velocities were seen in the figures below. As one would expect the radial velocities in the two mixing tanks are similar for a given impeller angular velocity. This phenomenon is not unexpected since the highest radial velocities are projected from the impeller region. However, since the rectangular tank's corners are further away from the impeller tip, slightly higher radial velocities were predicted in the cylindrical tank. This is a result of the cylindrical tank wall being closer to the impeller at a distance of 84.65 millimetres to the centre and the corners of the rectangular tank further away at approximately 106 millimetres from the centre.

The highest radial velocities were seen where the axial downward flow of the PBT is deflected by the bottom wall, creating the necessary circulation loops for solid suspension. The circulation loops in the cylindrical tank appear larger and more homogenous in **Figure 74** below. This may be a result of the rotational swirl being more effectively contained by the baffles.

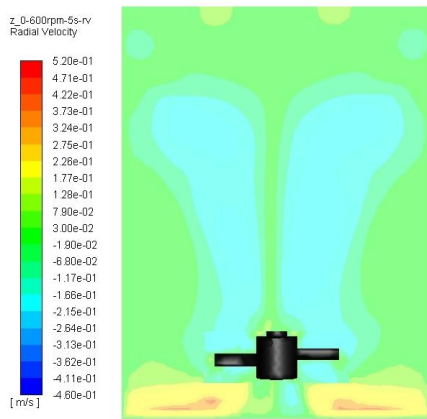


Figure 73: Rectangular radial vel. X=0

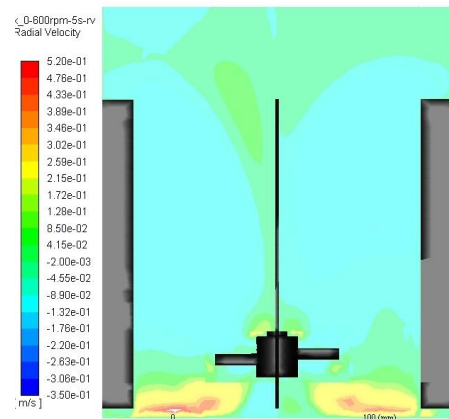


Figure 74: Cylindrical radial vel. Z=0

	Max. radial vel. (m/s)
Rectangular tank	0.52
Cylindrical tank	0.56

Table 10: Axial velocities

## 6.2.4 Tangential velocity

It is shown that the baffles break the swirling flow and cause wakes behind the baffle surface. In the rectangular mixing tanks, layers of stronger swirling flow are seen. However, the values at these regions are negligible and indicate that rotating swirl is not the dominant flow field. As expected the highest velocities were at the impeller, with tangential velocities increasing with the impeller speed. Regions of very low tangential velocity and or reverse flow were seen at the baffles and the corners. This confirms that the corners of the rectangular tank and the baffles are effective in preventing rotational swirl. The highest tangential velocities were seen right below the impeller, the contours of tangential velocity are shown in **Figure 75** and **Figure 76** below.

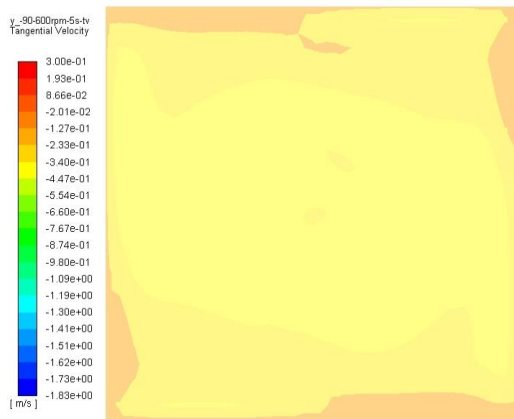


Figure 75: Rectangular tangential vel. Y=-90

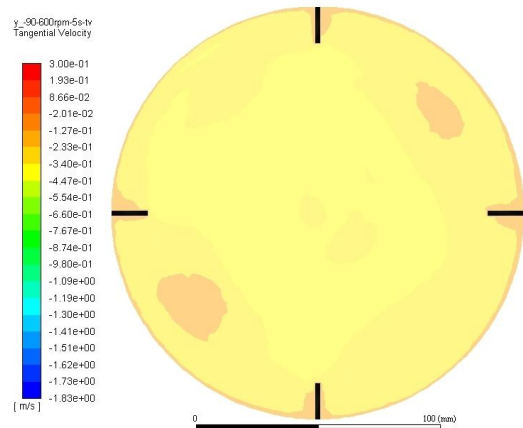


Figure 76: Cylindrical tangential vel. Y=-90

## 6.2.5 Velocity vectors

Clear recirculation zones are seen at the bottom of the mixing tanks in **Figure 77** and **Figure 78**, below. These recirculation zones increased in size as the impeller velocities were increased in both mixing tanks.

It is shown that the highest velocities for each scenario are at the bottom of the impeller in a downward direction which indicates that the fluid was predominantly axially discharged from the impeller as expected from a PBT. The fluid is forced downwards by the impeller and reflected by the bottom of the tank into upward currents along the side walls of the tanks. The velocity of the fluid was greatest at the tip of the impeller and gradually dissipates along the walls of the tanks.

The length of the circulation loops was more homogenous in the cylindrical tank. It is seen from the velocity vectors in **Figure 77** and **Figure 78**, that the flow is more turbulent at the top of the rectangular tank and that the flow is no longer predominantly axial. The same phenomenon applies to the cylindrical tank, but to a lesser extent.

In **Figure 77** and **Figure 78** below “dead spots” are seen below the baffles, in these “dead spots” the fluid motion is minimal and very weak velocity vectors are observed. This stationary fluid zone is unwanted since it allows the solids to settle and agglomerate in this region. The weak flows were seen in the bottom corners of both tanks, suggesting that a domed or tapered bottom could have greatly improved the transport of the granular phase. In the three dimensional illustration shown in **Figure 79** and **Figure 80** below, the weak flow region are clearly seen in the corners of the rectangular tank as well as the complete outer diameter of the bottom on the cylindrical tank.

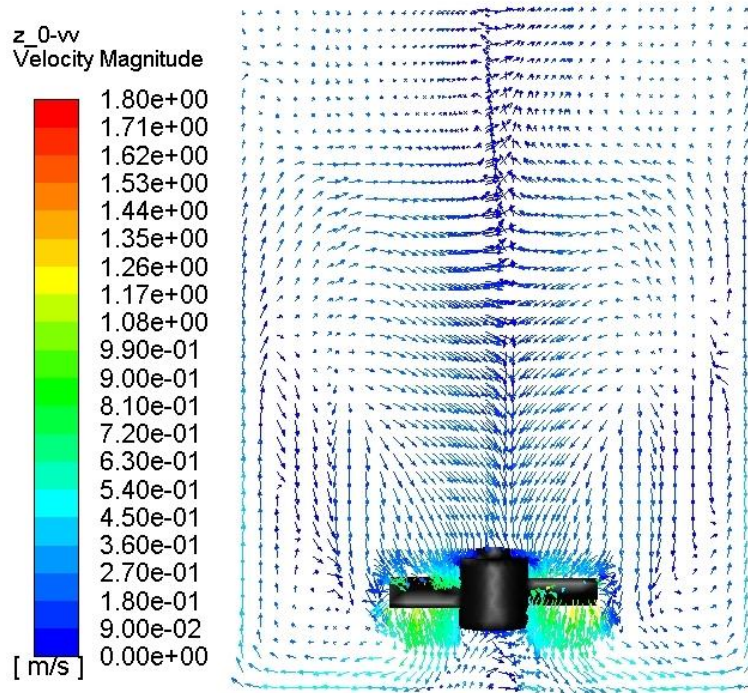


Figure 77: Rectangular tank mean vel. vectors

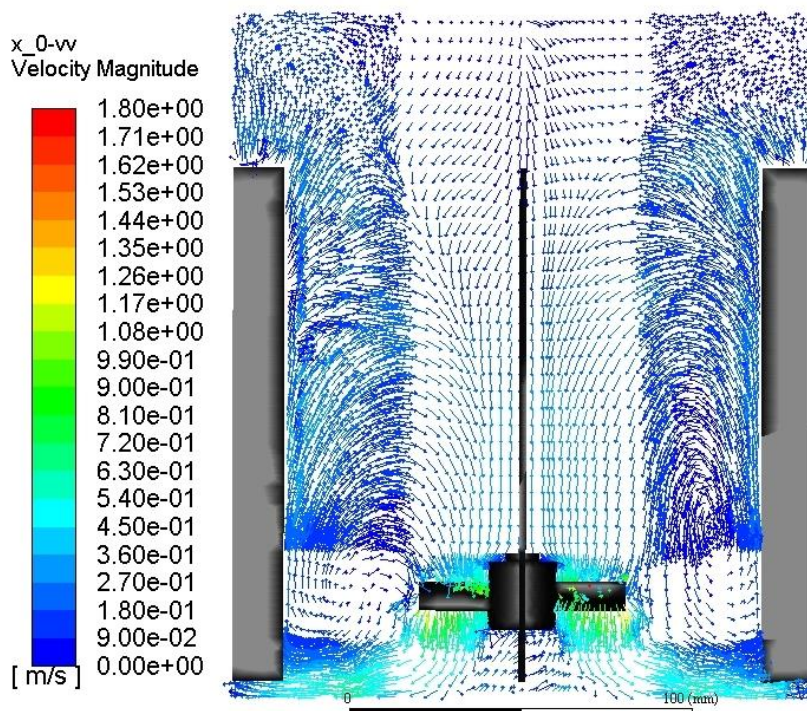
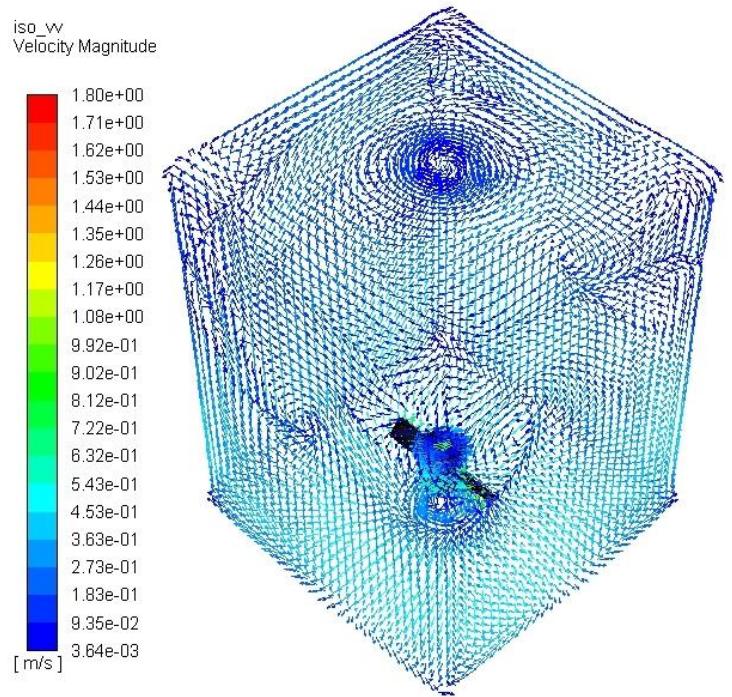
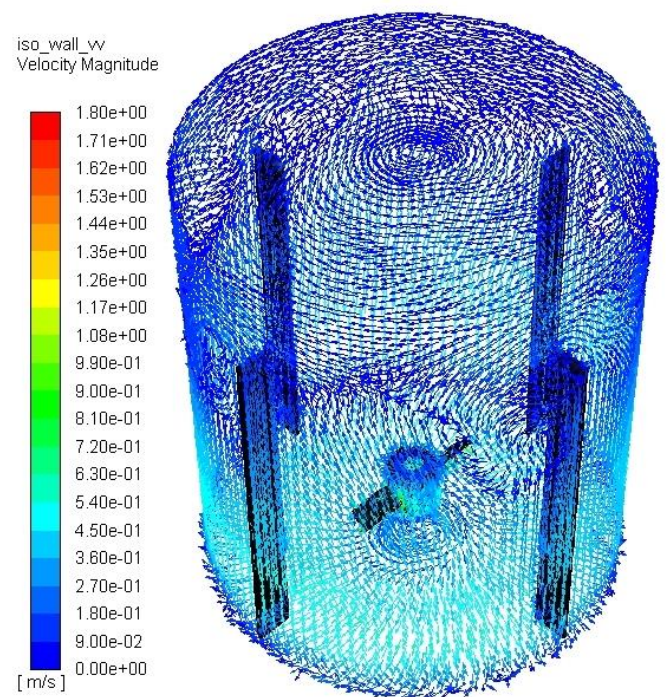


Figure 78: Cylindrical tank mean velocity vectors



**Figure 79: Rectangular tank mean velocity vectors at walls**



**Figure 80: Cylindrical tank mean velocity vectors at walls**

## 6.3 Contours of turbulence

### 6.3.1 Turbulent kinetic energy (K)

Turbulent kinetic energy is a measure of the mean turbulent kinetic energy per unit mass of eddies introduced by the impeller. The kinetic energy is transferred from the impeller to the fluid by convection and diffusion. The turbulent kinetic energy produced by the system is at a maximum around the impeller. The area below the impeller also indicates a region of elevated turbulent kinetic energy. It is a consequence of the downwards flow produced by the PBT being deflected of the tank bottom.

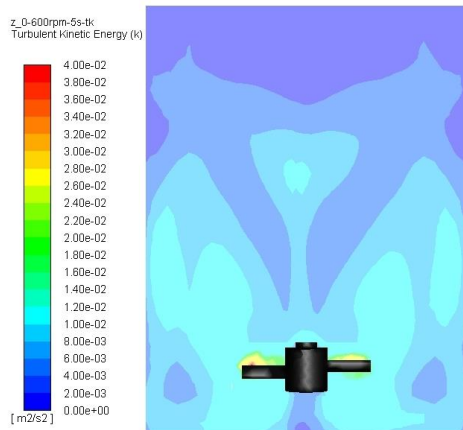


Figure 81: Rectangular turbulent kinetic energy

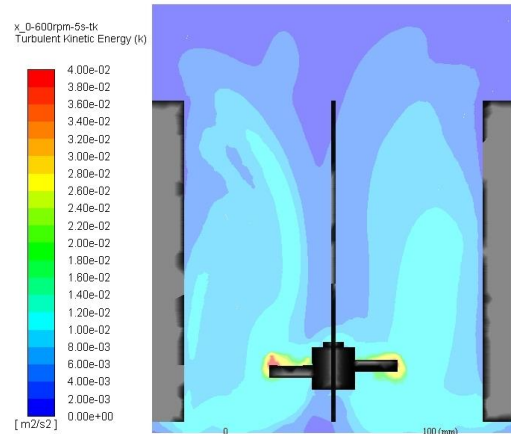


Figure 82: Cylindrical turbulent kinetic energy actual

### 6.3.2 Turbulent energy dissipation rate ( $\epsilon$ )

The highest energy dissipation was seen in the wake of the impeller blade. There was a small amount of energy dissipation at the baffles and none between the impellers and the baffles. In the rectangular tank, the energy dissipation was mainly at the impeller as a result of the absence of baffles. The energy dissipation rate was clearly higher in the wake of the blade than on the impeller tip side.

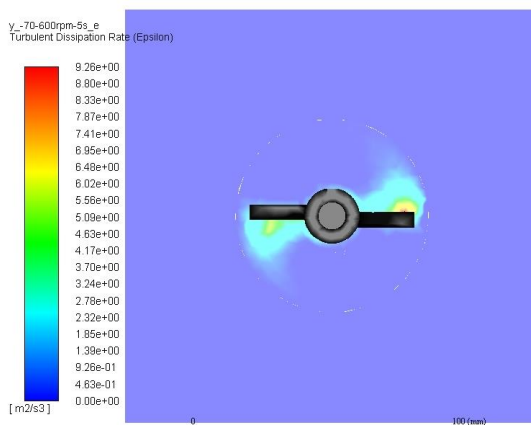


Figure 83: Rectangular turbulent energy dissipation rate

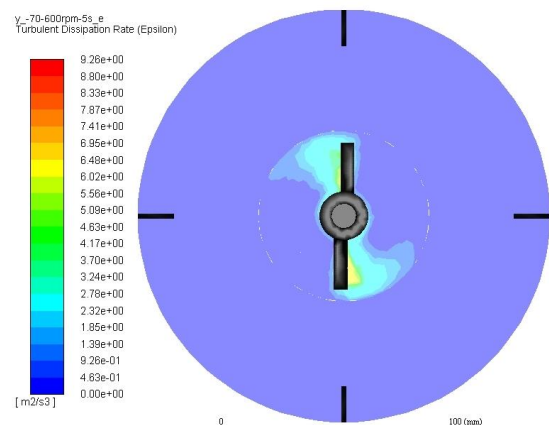


Figure 84: Cylindrical turbulent energy dissipation rate

### 6.3.3 Turbulent viscosity (eddy viscosity)

It can be seen below that the turbulent viscosities were not homogeneous. It varies in space. It is however, assumed isotropic, which is normally valid except where we have strong separation flows and high swirl. In the baffled mixing tanks, areas of high molecular diffusion were seen at the top of the vessel, which aligns with the velocity vectors shown above.

The red areas shown in the figures below indicate regions where the eddy current strength is at maximum. The regions above the impeller shows areas of increased turbulent eddy action. In the rectangular tank the eddy viscosity is weaker above the impeller compared to the cylindrical tank. It is expected since, the rotational swirl is less in the cylindrical tank leading to larger circulation loops resulting in higher eddy current presence.

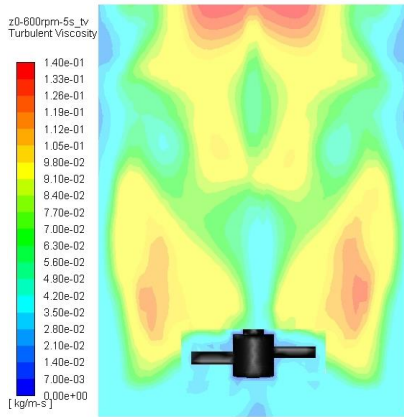


Figure 85: Rectangular turbulent viscosity

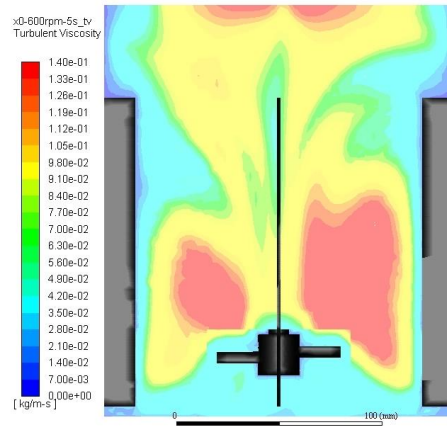


Figure 86: Cylindrical turbulent viscosity



## 6.4 Solids suspension

From the experimental setup, it was seen that the agitator should be operated between 600 - 750 rpm for sufficient solid suspension. In the simulation the tanks were compared at 600 rpm, with 5 seconds of simulation time.

A distinct interface was seen between the clear liquid at the top of the tank and the murky bottom region with a smaller intermediate region in between the two phases. It is noticeable that the solids were more uniformly distributed in the cylindrical tank. As suggested by previous researchers the turbulent dispersion and turbulent interaction forces were included in the model with a noticeable effect on the suspension of the secondary phase.

Using the Wen-Yu drag model with the Simonin turbulent interaction models on mono-sized, 150  $\mu\text{m}$  particles, where the eddy currents are fairly large within a low viscosity fluid, there is negligible difference between the continuous phase and the solid phase. This phenomenon is an indication that the solid phase was transported by the continuous phase without any slip as also stated by Bakker (2002).

	Rotational Vel. (RPM)	Cloud height (mm)
Cylindrical tank	600	200
Rectangular tank	600	170-172

Table 11: Solid suspension

Referring to **Table 11** above and the figures below, it is clear that the solids were not suspended entirely off-bottom in the rectangular tank when operated at 600 rpm. In the cylindrical tank, the solids are complete suspension.

Higher, more uniformly distributed solid suspension was achieved in the cylindrical tank as seen in **Figure 88** below.

The degree of solid suspension agrees well with the calculated velocity and turbulence contours. Directed upflow currents improved the turbulent kinetic energy in the mixture resulting in better solid suspension in the cylindrical tank.

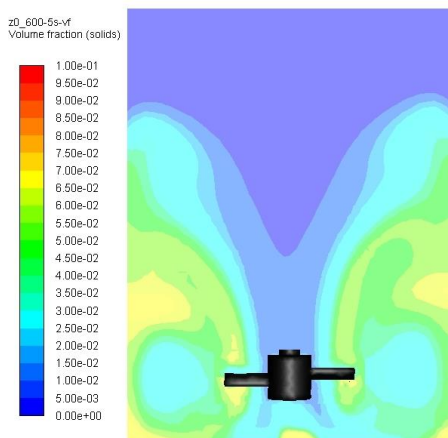


Figure 87: Rectangular solid suspension  
Z=0

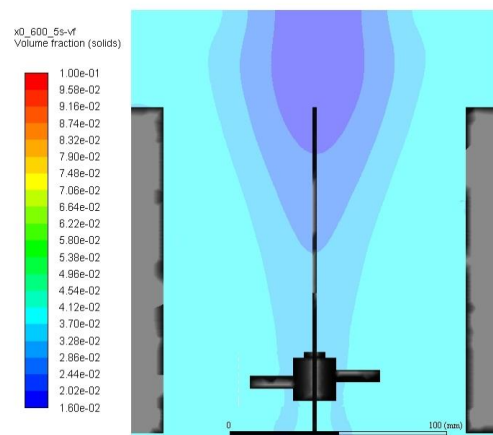
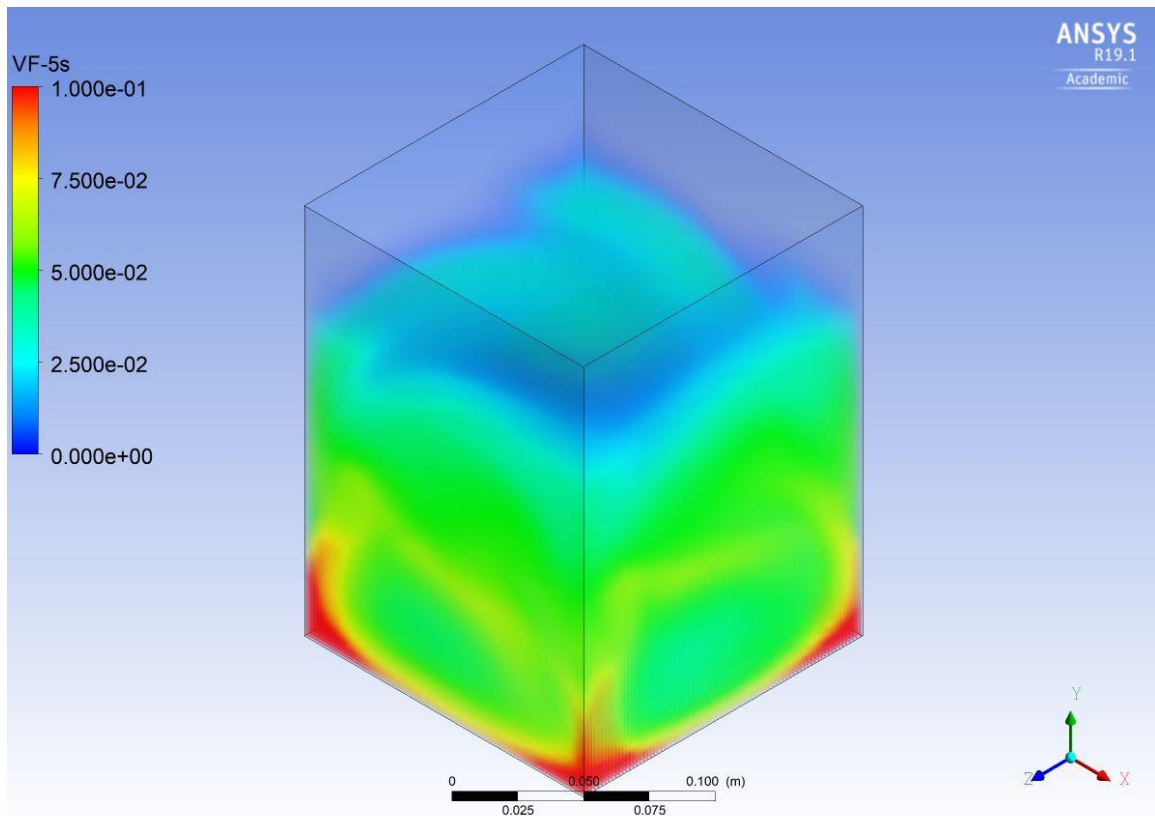


Figure 88: Cylindrical solid suspension  
X=0

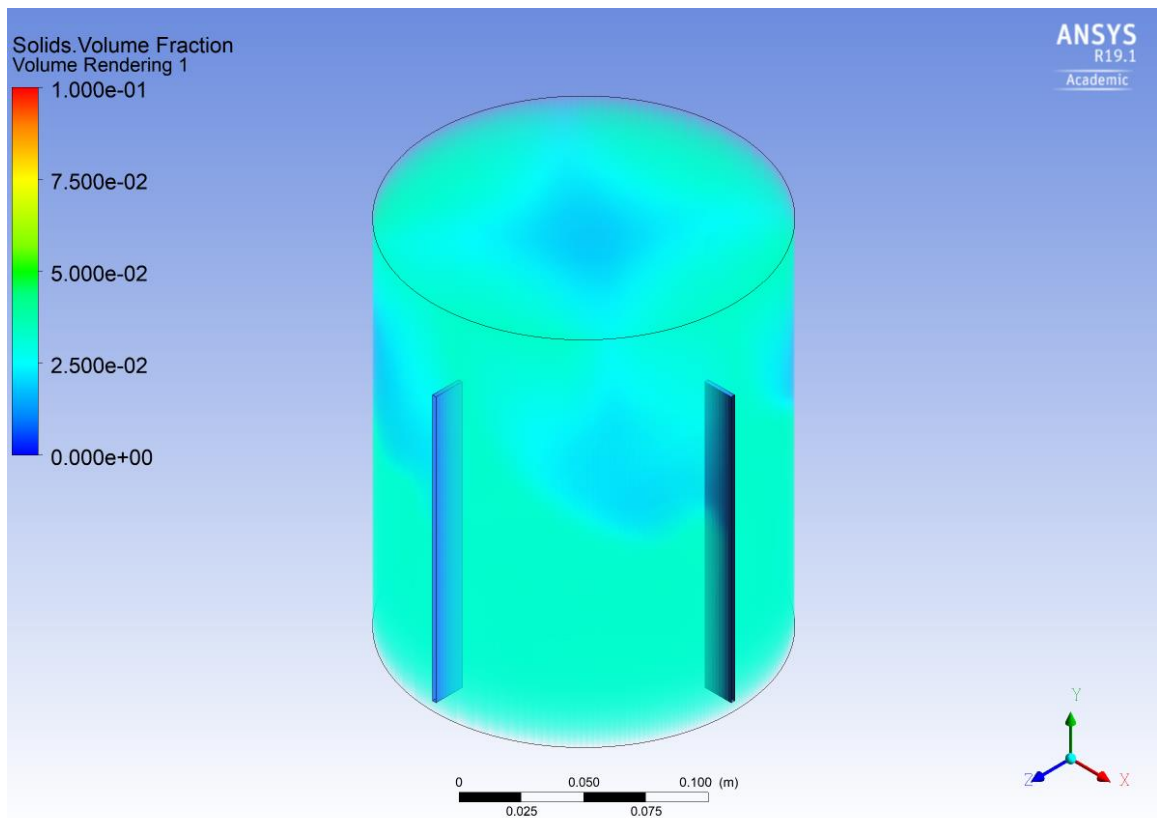
### 6.4.1 Solids distribution volume render

Three-dimensional representations of the suspension of solids is shown below for the different tanks. Areas of high solid loadings were seen at the corners of the rectangular mixing tanks in **Figure 89**. The solids concentration at the corners of the cylindrical tank in **Figure 90** is considerably less. It should be noted that the agglomeration of solids only occurred at the bottom corners of the rectangular mixing tanks. It would suggest that if the bottom of the tank was for e.g. conical, the absence of the 90° sharp corners would not have created “dead spots” and the solids would instead have been caught in an upward current and have been suspended more effectively.

It is clear from the figures above and below that the solids were suspended more efficient in the cylindrical mixing tank. Areas of very high solid concentration distribution were seen at the edge of the bottom and the wall in the rectangular mixing tanks. A more homogenous solids distribution was achieved in the cylindrical tanks. Concentrated solids up flow paths were seen near the baffle in **Figure 90**, this agrees well with increased up flow velocity patterns seen earlier in the baffle region.



**Figure 89: Solids distribution at 600 RPM Rect. – 5s**



**Figure 90: Solids distribution at 600 RPM Cyl. - 5s**

## CHAPTER 7: Conclusion

CFD analyses were performed on the suspension of CaCO<sub>3</sub> crystals within a mechanically agitated crystallizer tank. The performance of the rectangular crystallizer tank was compared to a cylindrical tank with baffling. It was experimentally shown that the tanks should be operated between 600 to 750 rpm. Performing the CFD simulation at 600 rpm with a corresponding simulation time of 5 seconds greatly reduced the computational expense while providing useful results.

After an extensive investigation, suitable CFD models were selected to simulate the flow fields in the crystallizer tank. The flow fields were computed using the RNG k- $\epsilon$  model. The suspension of solids was computed using the Eulerian-Granular multiphase technique.

It was important to select a suitable method for simulating the rotation of the impeller. Two-Dimensional methods were not suitable since the D/T ratio (Impeller Diameter/Tank diameter) changed with respect to time. Therefore, the computationally expensive three-dimensional sliding mesh (SM) technique was selected to simulate the impeller rotation.

The following aspects proved to be key for realistic simulations:

- The geometry must be divided into smaller compartments to better control the meshing
- Mesh quality: in areas where the flows are strong the elements should preferably be aligned. If not possible, the cells should be of similar size.
- Specific attention should be applied to the grid interface separating the rotating zone from the stationary zone to ensure cell sizes are not too different.
- When using the transient 3D sliding mesh method. Time step size should be computed from the respective angular velocity and a single time step size should not exceed the element size of the stationary interface.
- When mesh size is altered the time step should be adapted accordingly.
- The selection of appropriate drag formulation, turbulent interaction and turbulent dispersion were crucial.
- First order upwind schemes proved insufficient for the transient simulation.
- Different higher order discretization schemes had minimal effect on the flow regimes, however, it proved vital for accurate solid suspension predictions.

Based on the results of this study the following conclusion could be drawn:

### 7.1 Flow fields

Higher axial velocities were reached in the cylindrical mixing tanks as a result of the baffles directing the flow. The velocities around the impeller were alike for the rectangular and cylindrical tank as expected. Vortex formations in the experiment caused by highly turbulent flows at the top of the rectangular tank resulted in smaller circulation loops. The turbulent kinetic energy generated in the fluid by the impeller was slightly higher in the cylindrical mixing tanks. The higher kinetic energy was a result of the baffles directing the flow predominantly into an axial direction. The larger circulation loops and overall higher kinetic energy in the cylindrical mixing tanks allowed for better micromixing in the cylindrical tank. Subsequently, the turbulent dissipation was slightly less in the un-baffled mixing tanks. It was seen that, in the absence of baffling the flows were highly turbulent in the rectangular tank.

In both cases, domed or tapered tank bottoms could have greatly improved the suspension of solids and could also have reduced the turbulence in the corners by allowing for more gradual flow patterns. The bottom corners of the rectangular tank as well as the bottom wall around

the diameter of the cylindrical tank proved to be areas of weak flows that increased the accumulation of solids, decreasing the efficiency of the tank's overall design.

## **7.2 Off-bottom suspension and cloud height**

### **7.2.1 Experimental results**

The particle suspension of the experiment agreed well with the off-bottom suspension in the CFD simulation. During the initial stages of the calculation the dispersion of the packed bed were over predicted, at 10 seconds the gradients align and in the final stages the dispersion of the solids were slightly under predicted.

The cloud height was predicted with high accuracy regardless of the following difficulties:

- The particles in the experiment were not uniform, smaller particles were also contained in the mixture
- In the CFD the particles were of uniform density and size.
- The shape of the cloud matched the simulation results.
  
- The simulations were in good agreeance with reality until 15 seconds.
- After 15 seconds of simulation, the flow is dominated by swirl in the rectangular tank generating misleading results as a consequence of the chosen solvers inability to capture rotating swirl effectively.

### **7.2.2 CFD results**

The cylindrical tank had the same height as the rectangular tank. Considering the nature of a square versus a round shape of the same volume. The distance from the impeller tip to the wall in a circular shape will always be less than the distance to the square shape's corner. The constant smaller distance allowed the impeller to have a larger influence on the wall allowing for more uniform flow patterns and thus having the advantage over the square tank. It could be seen from the CFD results that energy in the corners were gradually dissipating towards the corner of the tank and an area where solids accumulation was evident at 600 rpm.

Consequently, more energy is required to achieve the same degree of suspension in terms of cloud height, when compared to a cylindrical tank. In the rectangular mixing tanks, it was seen that the corners acted as baffling to an extent and the main location for generating upward flow.

However, solid suspension were adversely affected by highly turbulent flow patterns near the top of the tank, as indicated by the turbulent viscosity and velocity vectors in the simulations. In the cylindrical tank the baffle wall produced the highest upflow currents and created longer circulation loops. The circulation loops were disrupted in the rectangular tanks by rotational swirl. It was seen that the cylindrical mixing tank developed a much more uniform flow field in general, which also resulted in a more uniform solids concentration distribution.

Flat bottomed tanks should also be avoided as the sharp corners have a negative impact on the flow patterns. The solids accumulated in the corners at low rotational velocity in the rectangular as well as the cylindrical tank. The efficiency of the system can be greatly improved by using cylindrical tanks with domed bottoms.

## **7.3 Overall performance**

### **7.3.1 Advantages of a rectangular mixing tank**

- I. The rectangular tanks were less expensive to manufacture, since slightly more complex geometries such as baffles and domed bottoms could be avoided. Standard bend up metal sheets could be used for the tank walls and the tapered bottoms.
- II. The stainless steel construction allowed for the in- and outlet connections to be designed and placed to precisely to interact properly with the system.
- III. The stainless steel was more robust, compared to other materials such as glass.
- IV. Corners acted as baffles to a reasonable extend in the CFD modelling as well as in the experimental apparatus at moderately low rotational velocities.

### **7.3.2 Disadvantages of a rectangular mixing tank**

- I. Slightly higher kinetic energy dissipation was reached in the cylindrical tanks, which is important for micromixing.
- II. Higher up-flow velocity and turbulent kinetic energy were obtained in the cylindrical tanks, indicating more gradual flow patterns which aid crystallization.
- III. Rotating swirl was likely to occur at increased velocities in the rectangular tanks.
- IV. More homogenous solids suspension was achieved in the cylindrical mixing tanks in the CFD modelling.
- V. Higher cloud heights were produced for the cylindrical tank in the CFD modeling.
- VI. The stainless steel was not insulated on the outside of the jacketed tanks, resulting in unwanted heat loss through the tank walls and an overall reduction in the efficiency of the system.
- VII. The distance from the impeller tip to the corners of the rectangular tank is more than the distance to the wall of a cylindrical tank and therefore, less energy is converted into up flow currents in the corners.

## **CHAPTER 8: Recommendations**

Areas interesting for future research are to compare the mixing tanks numerically with conical/round instead of flat bottoms. In this work single mineral mono-sized particles were used in the simulations, the effect of non-uniform and coalescing particles can be further investigated.

High radial velocities were seen at the impeller tip, which is unwanted since it induces crystal breakage by shear stress. However, by installing a concentric draft tube it is likely that lower impeller rotational velocities will be required for complete suspension and thus reduce shear stress breakages. The draft tube will further enable more uniform flow fields and eliminate the non-uniform flow fields seen particularly in the top of the cylindrical mixing tanks.

As reported by other researchers the impeller clearance has an effect on the 'just suspension' speed. Therefore, the effect of different impeller-to-base clearance heights can be investigated to study the effect on cloud height in the two tanks.

## CHAPTER 9: References

1. Anderson, J.D. 2009. *Governing Equations of Fluid Mechanics*: Springer-Verlag
2. Ansys Fluent inc. 2009. *Ansys Fluent 12.0 theory guide*, ANSYS, Inc.
3. Armenante, P., Nagamine, E. 1998. *Effect of low off-bottom impeller clearance on the minimum agitation speed for complete suspension of solids in stirred tanks*, Chem. Eng. Sci. 53(9) 1757–1775.
4. Aubin J., Fletcher D.F. and Xuereb C. 2004. *Modeling Turbulent Flow in Stirred Tanks with CFD: The Influence of the Modeling Approach, Turbulence Model and Numerical Scheme*, Experimental, Thermal and Fluid Science, 28, 431-445.
5. Bakker, A. and Oshinowo, L. 2002. *CFD modeling of solids suspensions in stirred tanks*. [www.bakker.org/cfm/tms2001.pdf](http://www.bakker.org/cfm/tms2001.pdf)
6. Boubakri, A., Hafiane, A. & Bouguecha, S. 2014. *Direct contact membrane distillation: Capability to desalt raw water*. Arabian Journal of Chemistry. <http://dx.doi.org/10.1016/j.arabjc.2014.02.010>
7. Cokljat, M., Slack, M., Vasquez, S., Bakker, A., Montante, G. 2006. *Reynolds-Stress Model for Eulerian Multiphase*. [www.bakker.org/cfm/publications/Cokljatetal2006.pdf](http://www.bakker.org/cfm/publications/Cokljatetal2006.pdf)
8. Dow water and process solutions., (n.d.) *RO technical manual*. <http://www.dowwaterandprocess.com>
9. Dow, N., Zhang, J., Duke, M., Li, J., Gray, S.R., Ostarcevic, E. 2008. *Membrane distillation of brine wastes*. Water Quality Research Australia Limited.
10. EFC separations., *Eutectic Freeze Crystallization – The process*. 2012. <http://www.efc.nl/the-efc-process/>. (24 August 2016)
11. Genck, J. 2003. *Optimizing crystallizer scale up*. Genck International, [www.genckintl.com/articles.html](http://www.genckintl.com/articles.html)
12. Gohel, S., Joshi, S., Azhar, M., Horner M. & Padron, G. 2012. *CFD modeling of solids suspension in a stirred tank, effect of drag models and turbulent dispersion on cloud height*. [www.hindawi.com/journals/ijce/2012/956975/](http://www.hindawi.com/journals/ijce/2012/956975/)
13. Guida, A., Nienow, A.W. & Barigou, M. 2010. *PEPT measurements of solid-liquid flow field and spatial phase distribution in concentrated monodisperse stirred suspensions*. Chem. Eng. Sci., 65(6), 1905-1914.
14. Himmelsbach, W., Houlton, D., Keller, W. & Lovallo, M. 2006. *Mixing systems: Design and scale up*. Ekato mixing technology. [www.ekato.com/fileadmin/user\\_upload/.../2006\\_04\\_CoverStory.pdf](http://www.ekato.com/fileadmin/user_upload/.../2006_04_CoverStory.pdf)
15. Hsu, S.T., Cheng, K.T. and Chiou, J.S. 2002. *Desalination*. 143, p.279.
16. Ibrahim, S., Jasnin, S. N., Wong, S.D. and Baker, I.F. 2012. *Zwietering's Equation for the Suspension of Porous Particles and the Use of Curved Blade Impellers*. International Journal of Chemical engineering, Vol 2012 (2012), Article ID 749760, 13 pages. <http://dx.doi.org/10.1155/2012/749760>
17. Jonsson, A., Wimmerstedt, R., & Harryson A. 1985. *Desalination*. 56, p.237
18. Kubicki, D., Lo. S., Analysis of Kubicki et al. 2012. Researcher at the department of Chemical Engineering at Vaal university of Technology. *CFD predictions of solids distribution in stirred vessel*. [http://www.cd-adapco.com/conference\\_proceeding/cfd-predictions-solids-distribution-stirred-vessel](http://www.cd-adapco.com/conference_proceeding/cfd-predictions-solids-distribution-stirred-vessel)
19. Kubota, A., Ohta, K., Hayana, I., Hirai, M., Kikuchi, K and Murayama, Y. 1988. "Desalination", 69, p.19.
20. Martinez-Diaz, L., & Florida-Diaz, F.J. 2001. *Desalination*. 137, p.267.
21. Mahdi, M., Shirazi, A., Kargari, A., Tabatabaei, M. 2004. *Evaluation of commercial PTFE membranes in desalination by direct contact membrane distillation*. Chemical Engineering and Processing: Process Intensification, Volume 76, February 2014, Pages 16-25, ISSN



- 0255-2701, <http://dx.doi.org/10.1016/j.cep.2013.11.010>.  
<http://www.sciencedirect.com/science/article/pii/S0255270113002742>)
22. Montante, G. and Magelli, F. 2003. *CFD predictions of solid concentration distributions in baffled and unbaffled vessels agitated with multiple A310 Impellers*. Proceedings of the Sixth Italian Conference on Chemical and Process Engineering, June, Pisa, Italy, pp.1481–1486.
  23. Morillo, J., Usero, J., Rosado, D., Bakouri, H., Riaza, A., Bernaola. 2014. *Comparative study of brine management technologies for desalination plants*. Department of chemical and environmental engineering. Spain.  
[http://atominfo.ru/files/brine/Brine%20from%20desalination%20plants\\_11.pdf](http://atominfo.ru/files/brine/Brine%20from%20desalination%20plants_11.pdf))
  24. Myers, K., Reeder, M., Fasano, J. 2002. *Optimizing a mixer by using the proper baffles*. CEP. <http://people.clarkson.edu/~wwilcox/Design/mixopt.pdf>
  25. Nathoo, J. 2014. Interview in January 2014. Cape Town
  26. Ochieng, A., Onyango, M., Analysis of Ochieng et al., 2010. *CFD simulation of solids suspension in stirred tanks*. <http://www.doiserbia.nb.rs/img/doi/0367-598X/2010/0367-598X1000051O.pdf>
  27. Ochieng, A., Lewis, A. 2006. *CFD simulation of nickel solids concentration distribution in a stirred tank*. *Min. Eng.* 19. 180–189.
  28. Paul, E., Atiemo Obeng, V., Kresta, S. 2004. *Handbook of industrial mixing, science and practice*: Wiley.
  29. Pianko-oprych, P., Nienow, A. & Barigou, M. 2009. *Positron emission particle tracking (PEPT) compared to particle image velocimetry (PIV) for studying the flow generated by a pitched-blade turbine in single phase and multi-phase systems*, *Chem. Eng. Sci.*, 64(23), 4955-4968.
  30. Pinelli, D., Nocentini, M. and Magelli, F. 2001. *Solids distribution in stirred slurry reactors: influence of some mixer configurations and limits to the applicability of a simple model for predictions*. *Chem. Eng. Comm.*, Vol. 118, pp.91–107.
  31. Samant, K & O'Young, L. 2006. *Understanding crystallization and crystallizers*. Clear Water Bay technology inc.
  32. Sarti, G.C., Gostoli, C. and Matulli, S. 1985. *Desalination*, 56, p.277.
  33. Sardeshpande, M. V. 2009. *Solid Suspension and Liquid Phase Mixing in Solid-Liquid Stirred Tanks*. *Industrial & Engineering Chemistry Research*, 48(21), 9713-9713
  34. Shah, M. 2009. *Process Engineering: Agitation & Mixing*. Dharamsinh Desai University India, Short course material, [www.dduanchor.org/site/.../Process-Engineering-Agitation-Mixing.pdf](http://www.dduanchor.org/site/.../Process-Engineering-Agitation-Mixing.pdf)
  35. Sharma, R., Shaik, A. 2003. *Solids suspension in stirred tanks with pitched blade turbines*. *Chem. Eng. Sci.* 58, 2123–2140.
  36. Vakili, M.H., Esfahany, M. 2008. *CFD analysis in a baffled stirred tanks, a three-compartment model*. [www.elsevier.com/locate/ces](http://www.elsevier.com/locate/ces)
  37. Wadnerkar, D., Utikar, R., Tade, M., Pareek, V. Analysis of Wadnerkar et al., 2011. the citation of web-based information resources by Curtin University Perth researchers. *CFD simulations of solid-liquid stirred tanks*.  
[www.conference.net.au/chemeca2011/papers/571.pdf](http://www.conference.net.au/chemeca2011/papers/571.pdf)
  38. Wadnerkar, D., Utikar, R., Tade, M., Pareek, V. Analysis of Wadnerkar et al., 2012. the citation of web-based information resources by Curtin University Perth researchers. “*Simulation of solid-liquid flow in stirred tanks at high solid loading*”.  
[http://www.cfd.com.au/cfd\\_conf12/PDFs/084WAD.pdf](http://www.cfd.com.au/cfd_conf12/PDFs/084WAD.pdf)
  39. Yang, X., Yu, H., Wang, R & Fane, A, 2012. *Analysis of the effect of turbulence promoters in hollow fibre membrane distillation modules by computational fluid dynamic (CFD) simulations*. *Journal of membrane science*.
  40. Yamazaki, H. 1986. *Concentration profiles of solids suspended in a stirred tank*. *Powder Technol.*, 48(3), 205-216.
  41. Zwietering, T. 1958. *Suspending of solids particle in liquid by agitators*. *Chem. Eng. Sci.* 8. 244–253.

## APPENDIX A – PLC Selection

- Programmable Logic controller (PLC) selection

The following points were taken into consideration when the PLC was selected.

- Modular
- Economical
- Easy to set up
- Easy to use
- Functionality
- Logging capability
- Display - Presentation of data
- Cosmetically attractive

It was decided that the best system for this specific application is the fully automated system, easing the operating, eliminating human error and last but not least it presents the data clearly.

In order to select brand for this application the following manufacturers were taken into consideration.

### ➤ **LSIS**

- PLC, digital in- and outputs, RS 232, RS 485, Ethernet
- HMI
- Analogue in and output expansions
- DP Switch
- Ethernet expansion module
- SCADA license
- SQL server
- Ladder programming software

### ➤ **Rockwell automation**

- PLC, digital in- and outputs, RS 232, RS 485, Ethernet
- HMI
- Analogue in and output expansions
- DP Switch
- Ethernet expansion module
- SCADA license
- SQL server
- Rockwell propriety programming software

### ➤ **Unitronics**

- PLC, digital in- and outputs, RS 232, RS 485, Ethernet integrated HMI
- Analogue in and output expansions
- Ethernet expansion module
- SQL server
- Download to SD card
- Export to Excel

- Built in logging capability

Ladder programming software

Unitronics was selected because of its relatively inexpensive price, no annual licenses required, built in logging capability and a HMI with an integrated PLC increasing simplicity and minimizing wiring.

The programmable logic controller with digital and analogue inputs and outputs are fitted to control the setup.

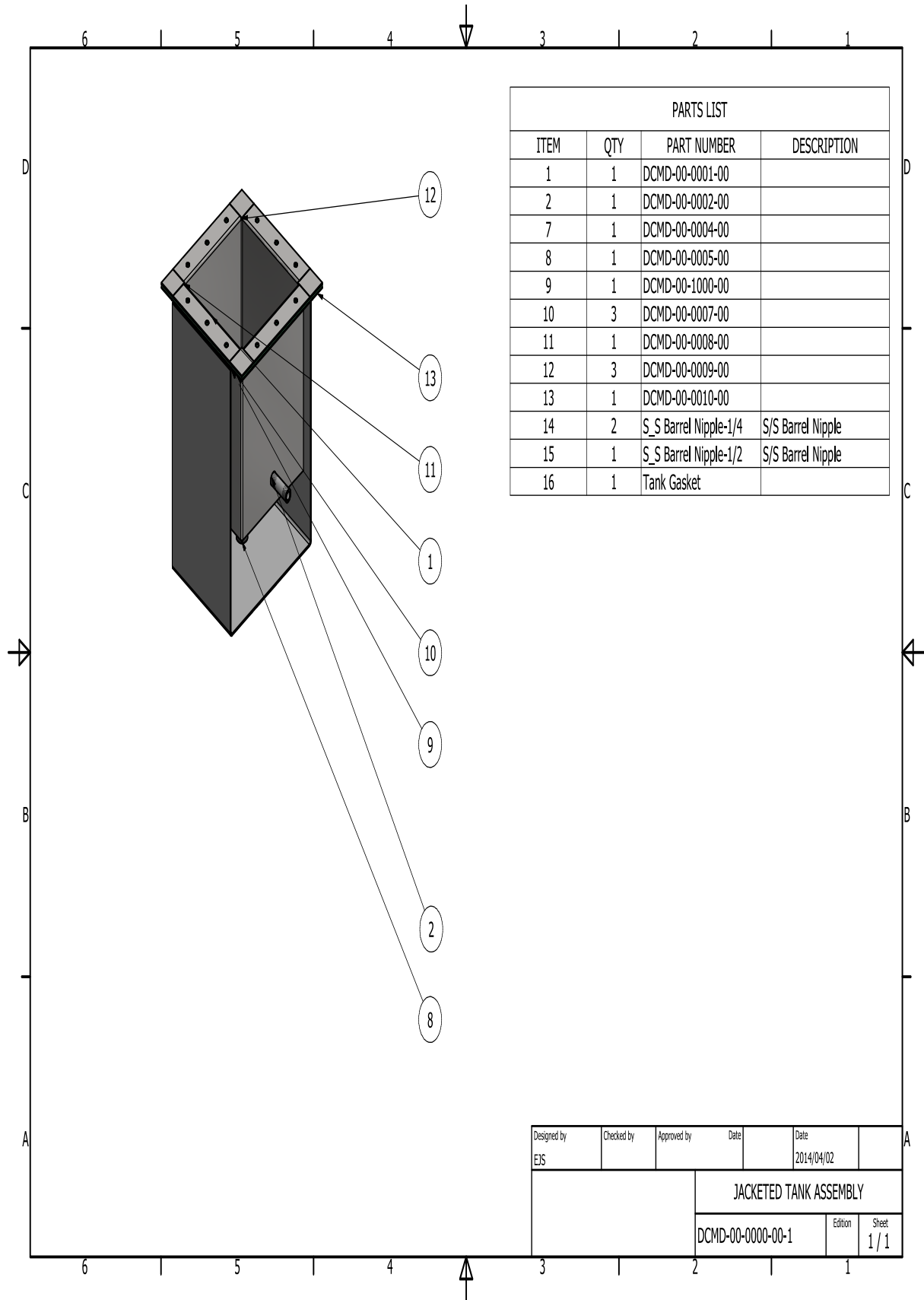
➤ **Analogue inputs.**

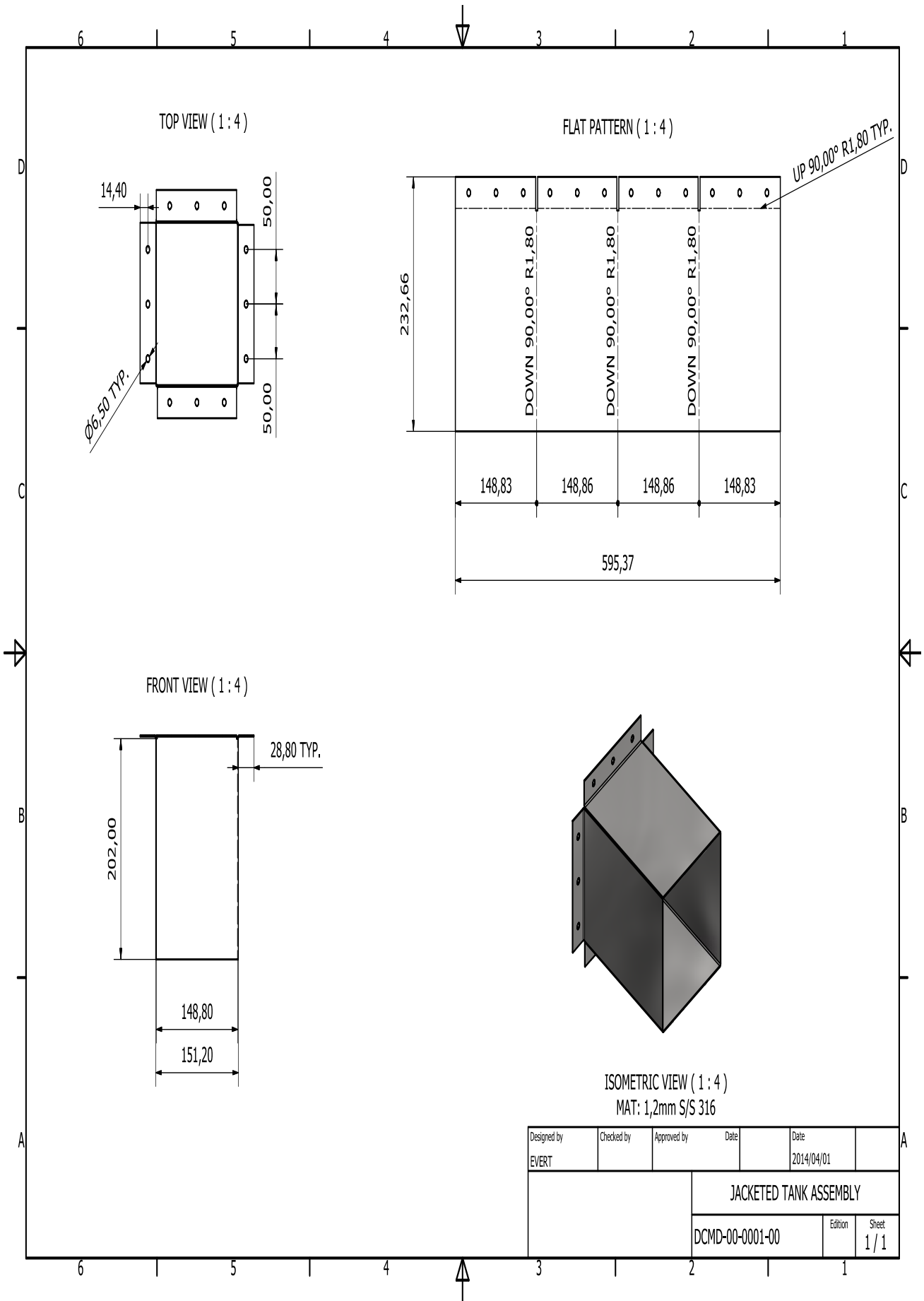
- 4-20 mA pressure transmitters, with a range of 0 to 4 bar.
- 4-20 mA PT 100 temperature transmitters.
- 4-20 mA Conductivity controllers & cells
- 4-20 mA pH controllers & probes

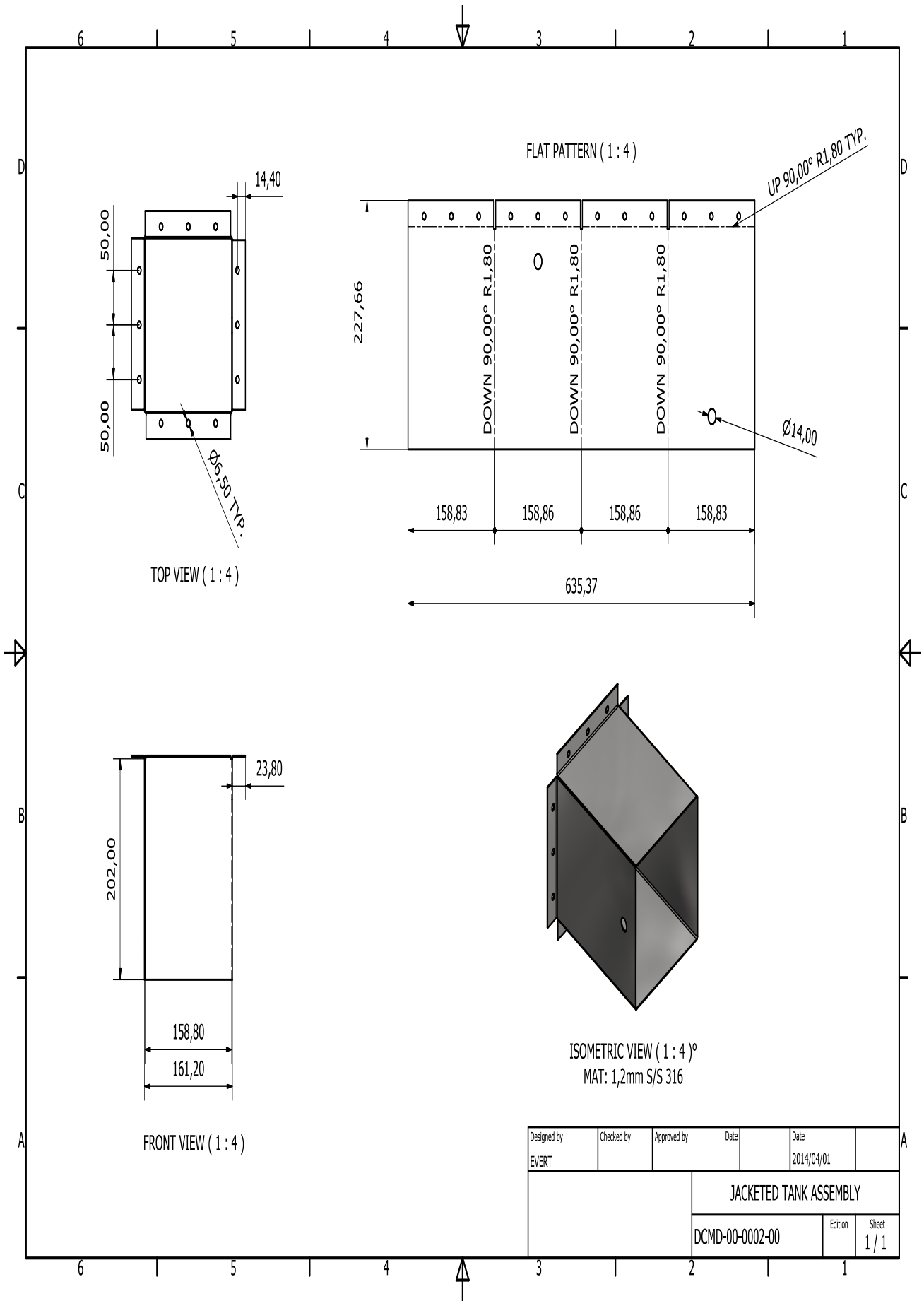
➤ **Digital outputs.**

- Start and stop control of pumps
- Start and stop control of chillers

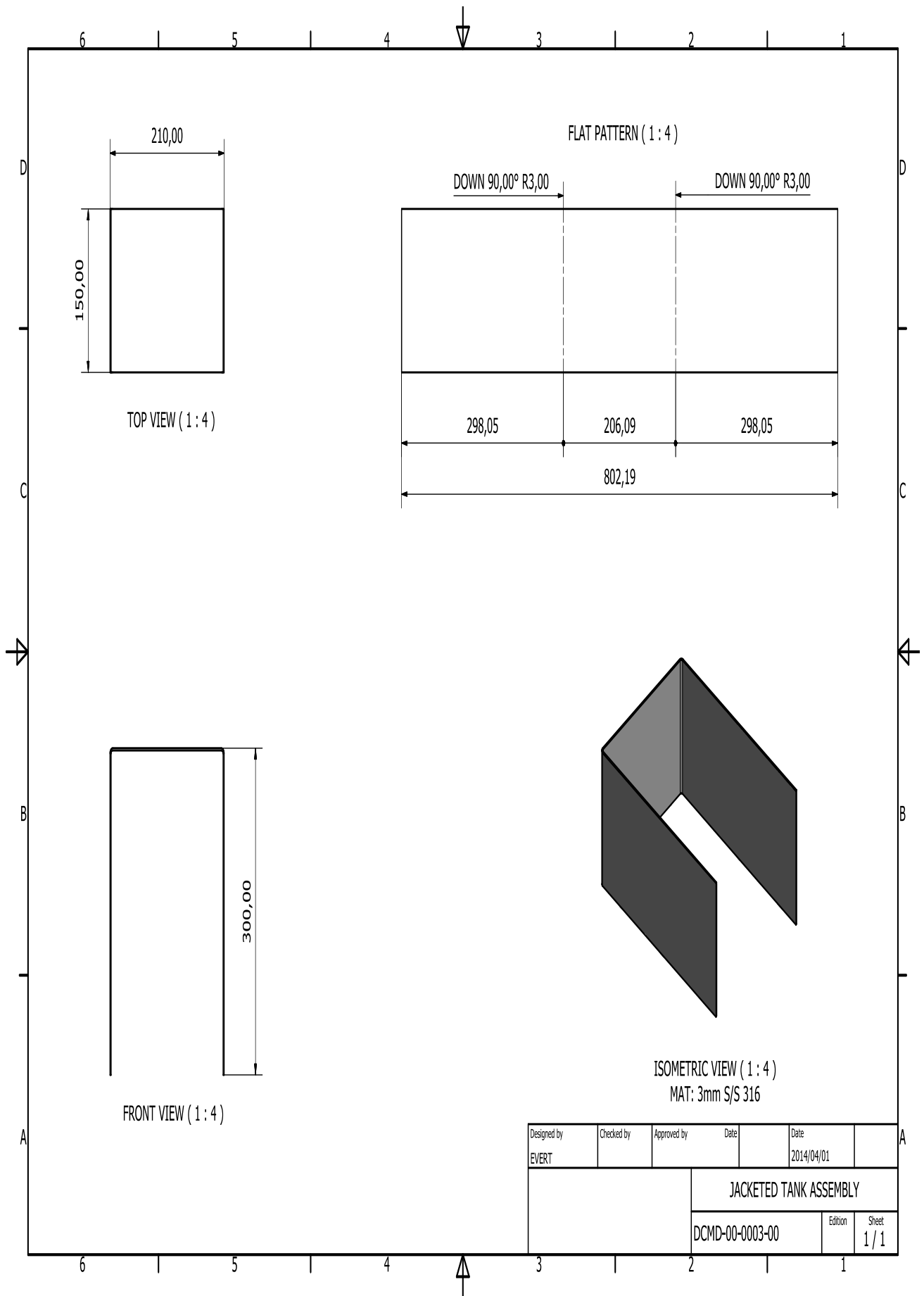
## APPENDIX B – Manufacturing drawings

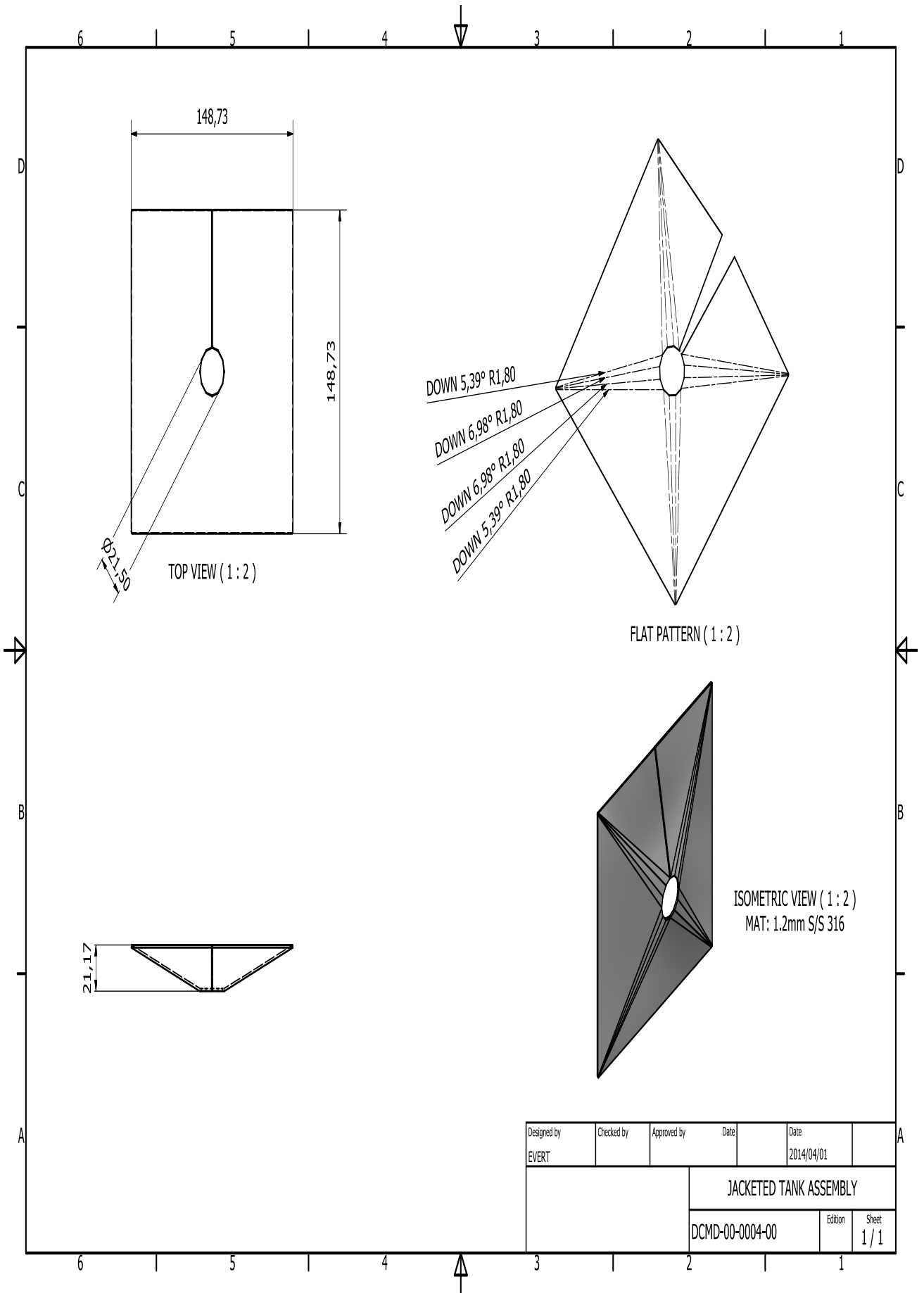




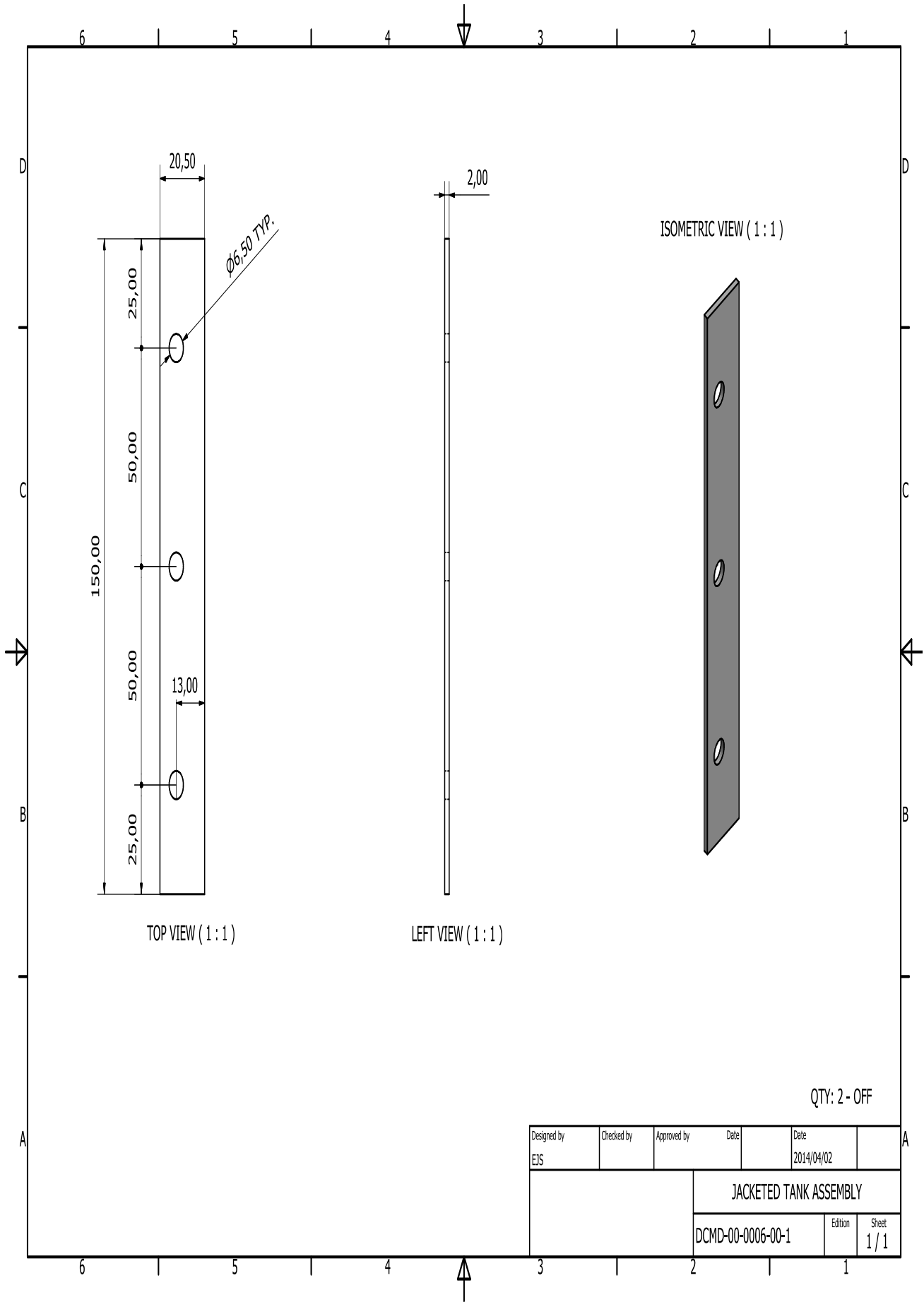


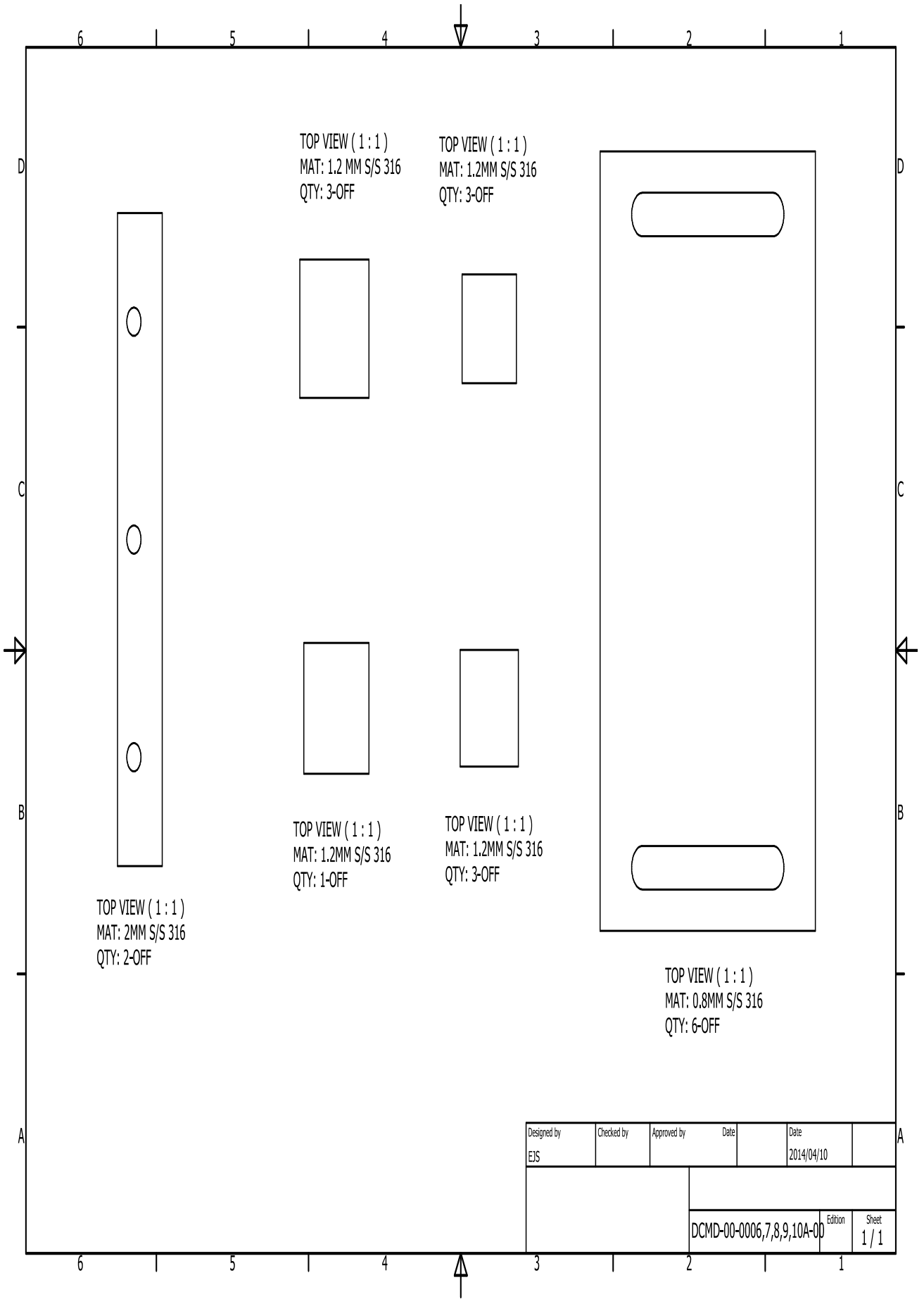
Designed by EVERT	Checked by	Approved by	Date	Date 2014/04/01
			JACKETED TANK ASSEMBLY	
			DCMD-00-0002-00	Edition 1 / 1

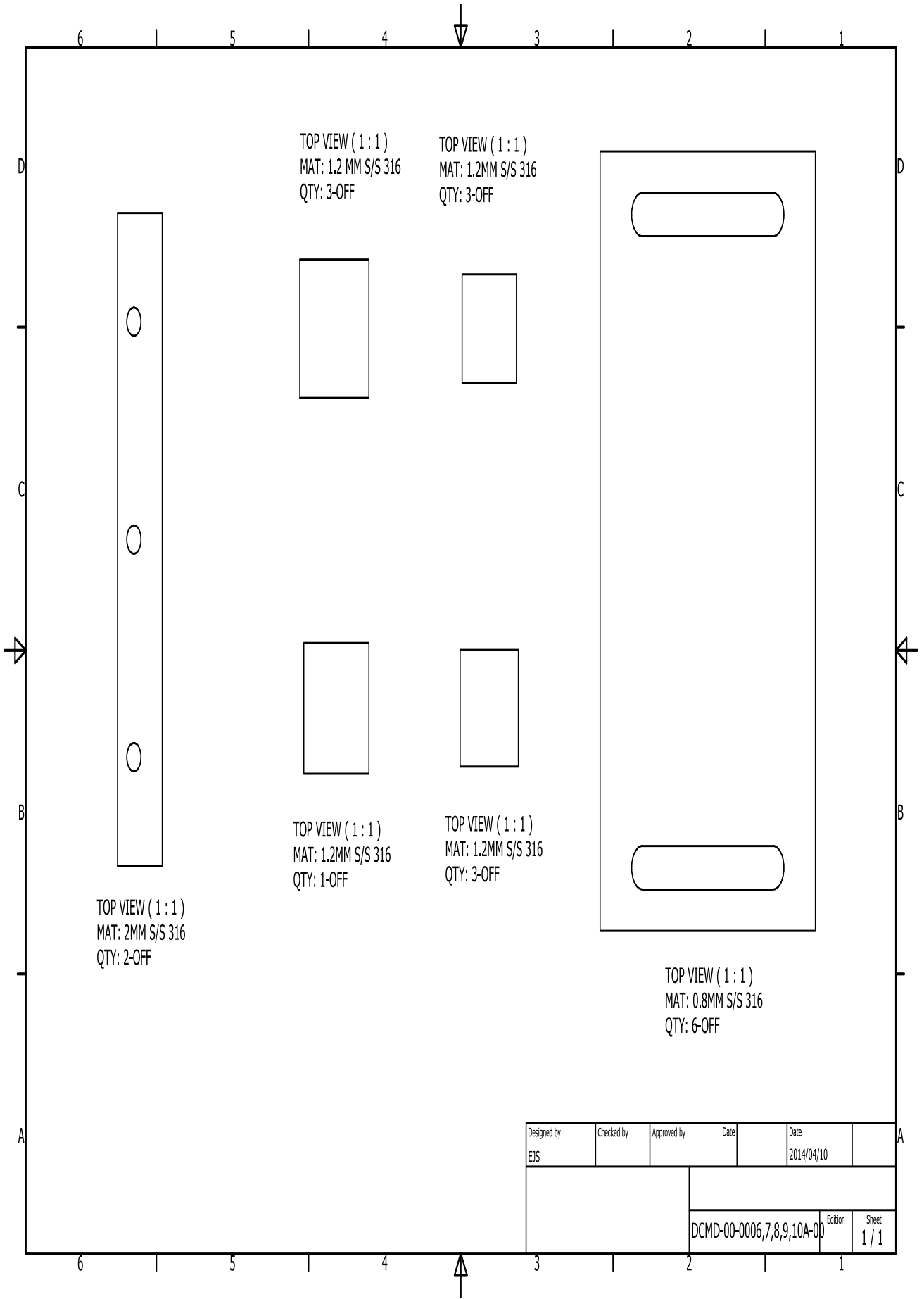


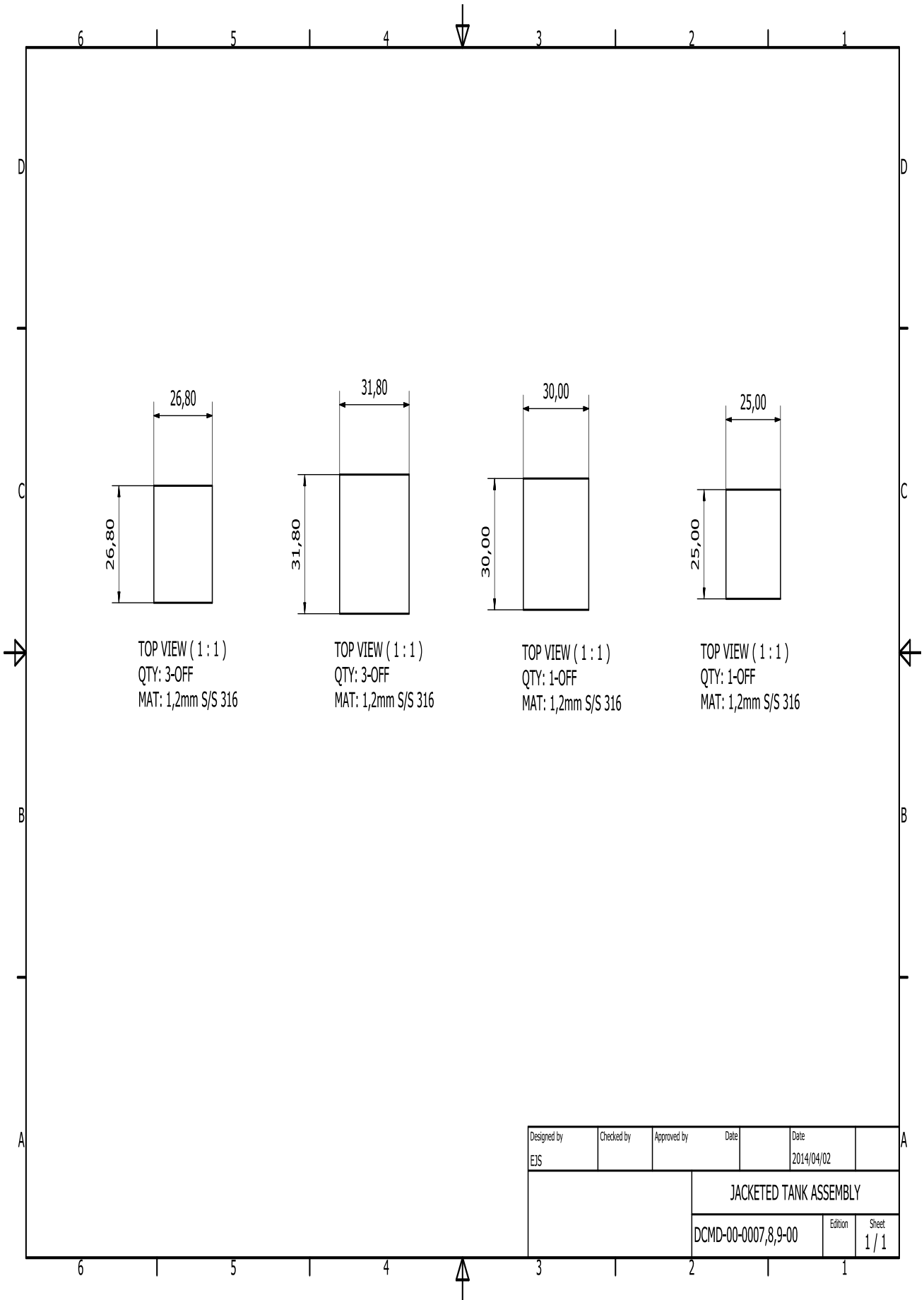


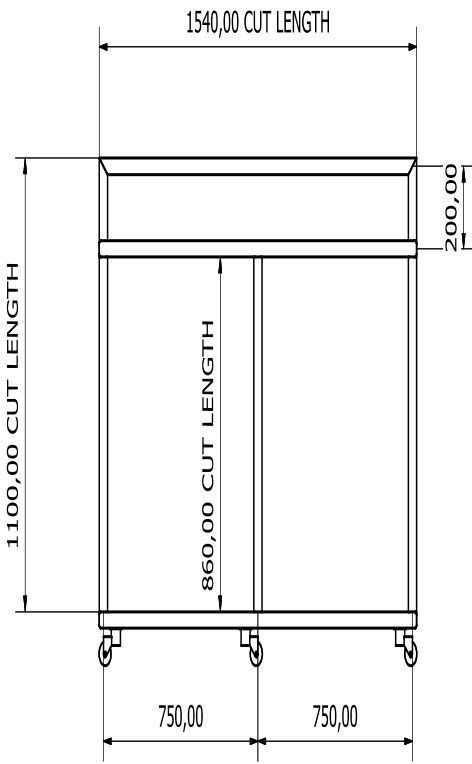
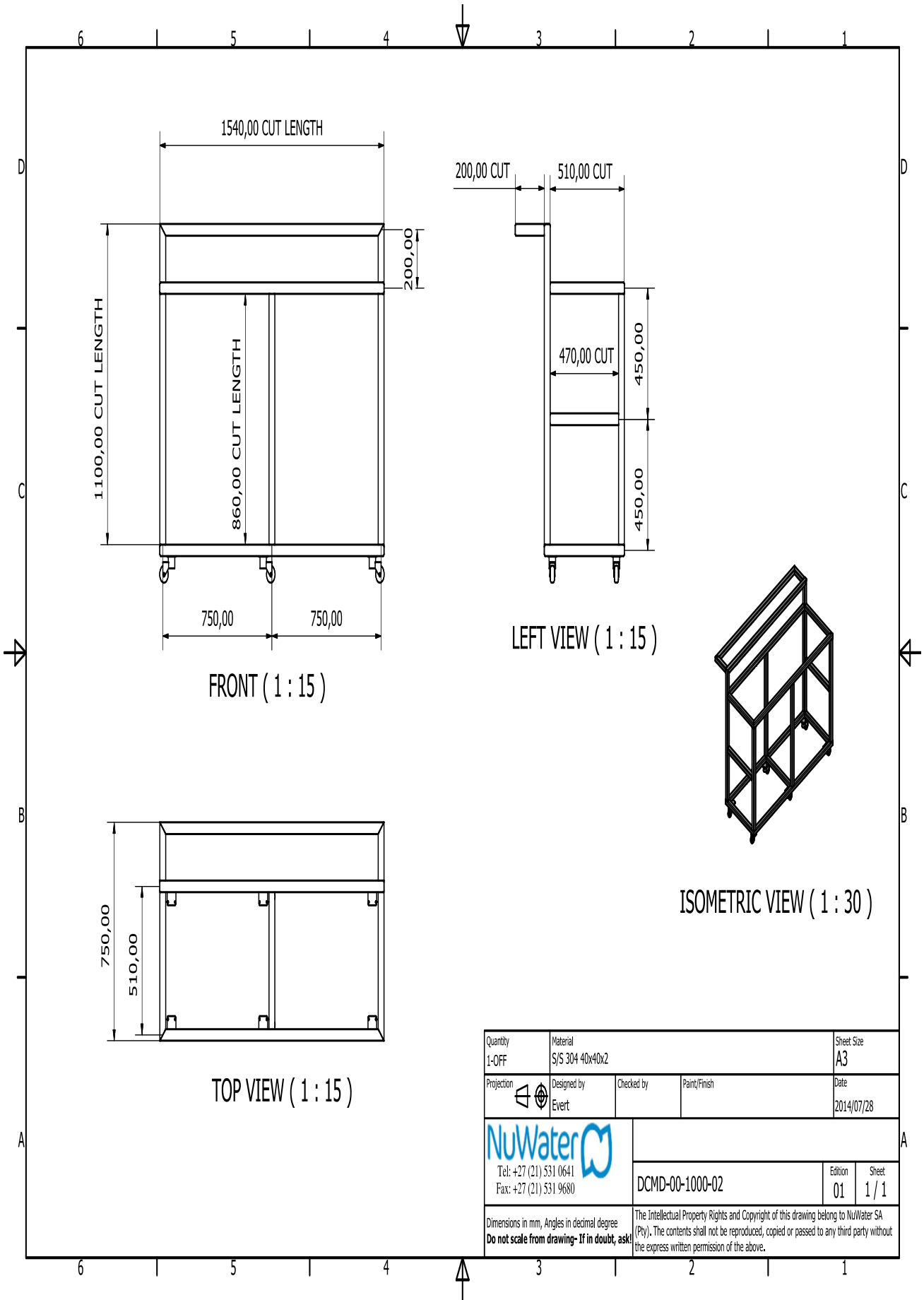




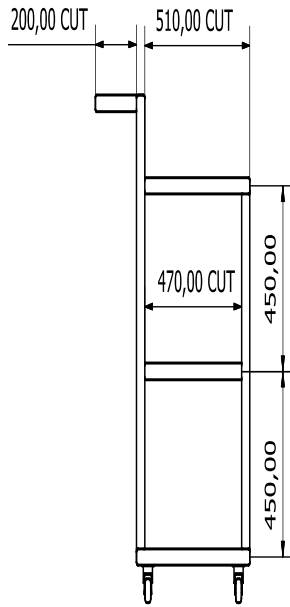




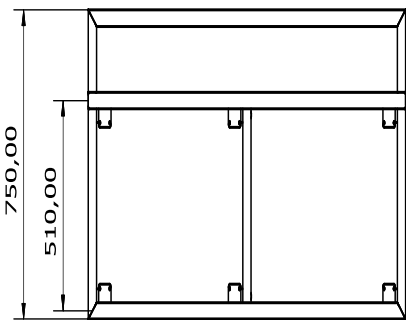




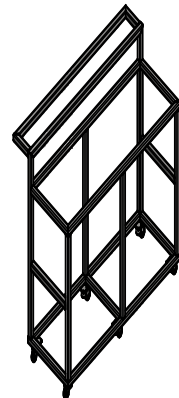
FRONT ( 1 : 15 )




LEFT VIEW ( 1 : 15 )

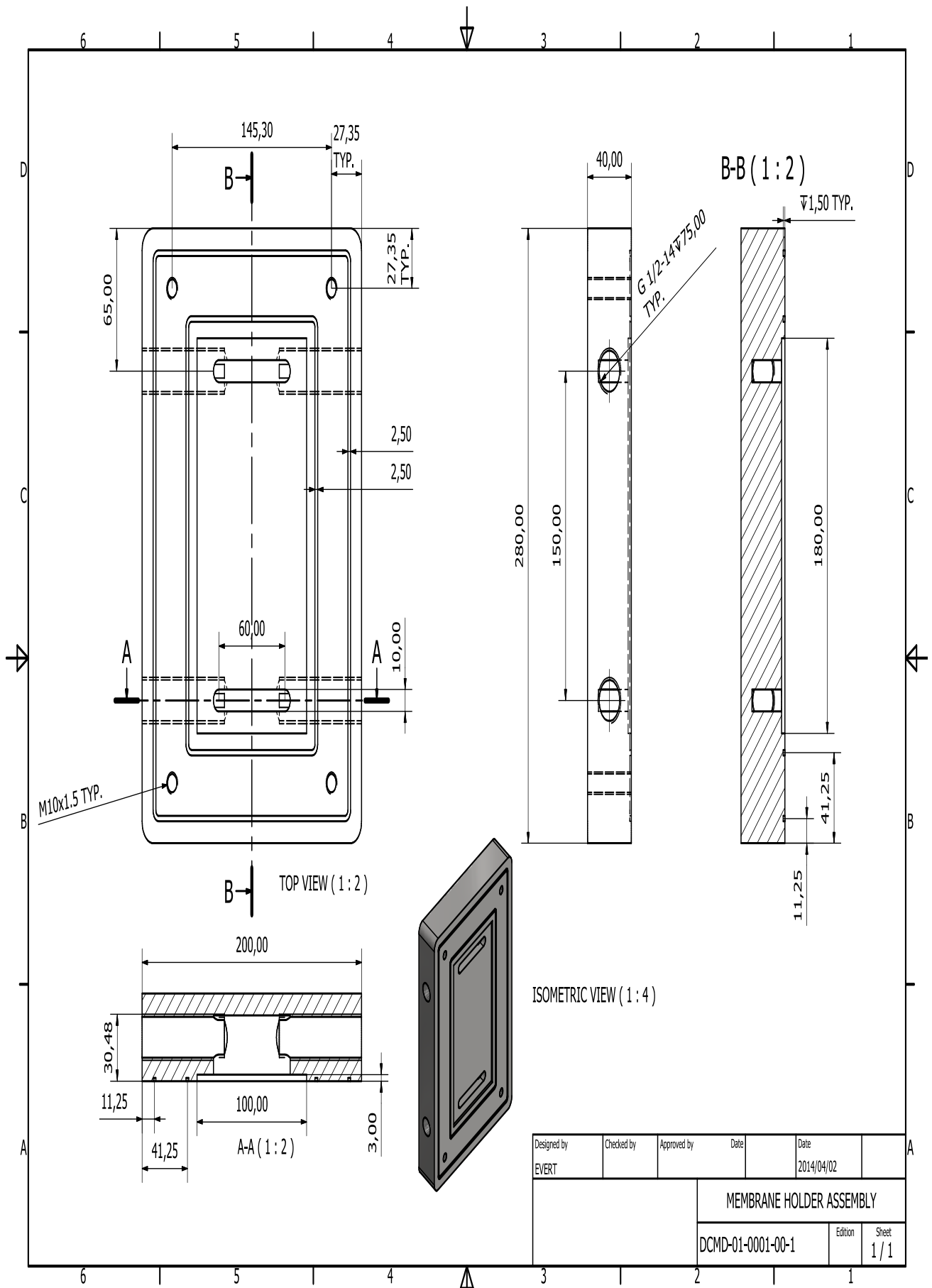


TOP VIEW ( 1 : 15 )

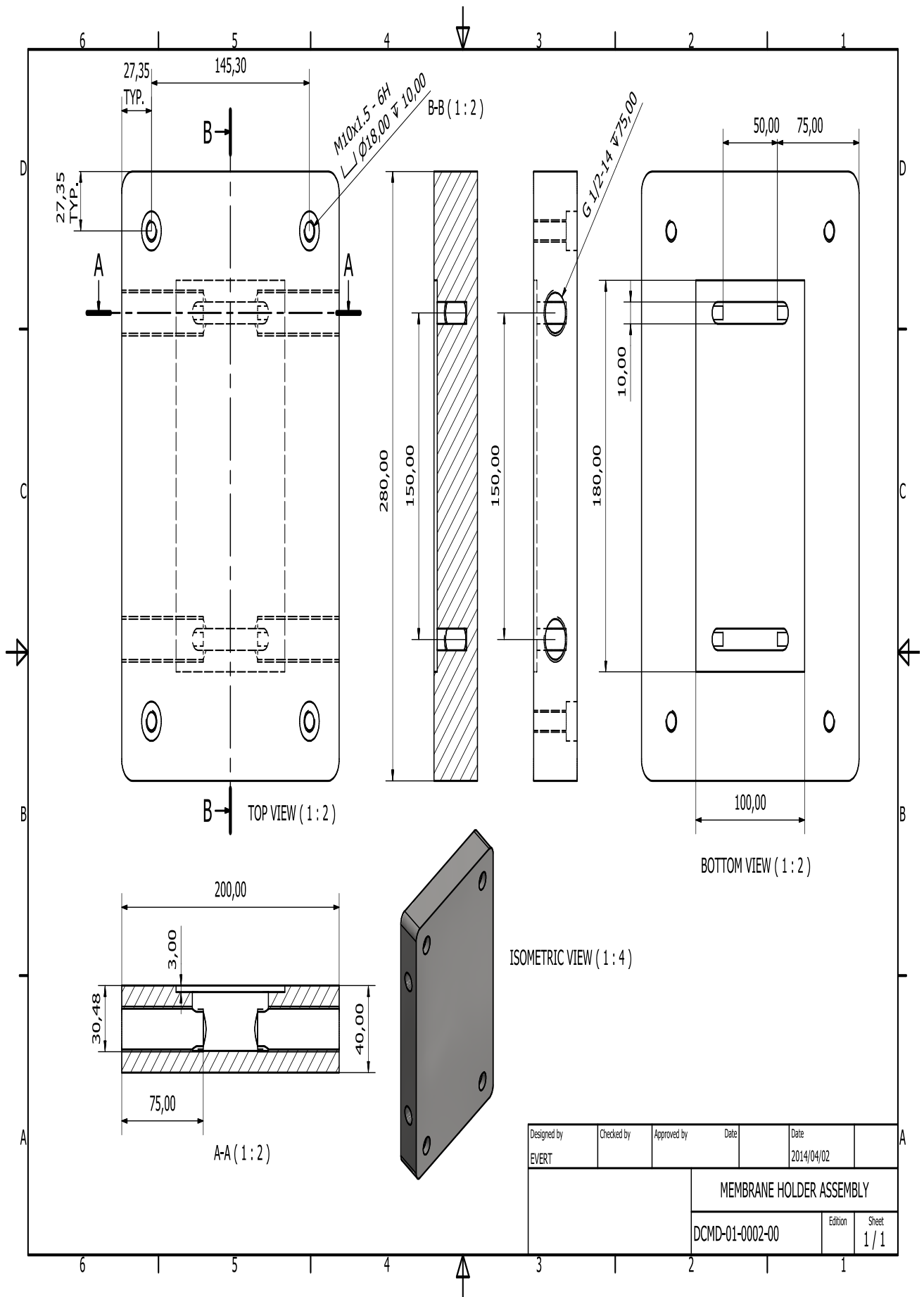


ISOMETRIC VIEW ( 1 : 30 )

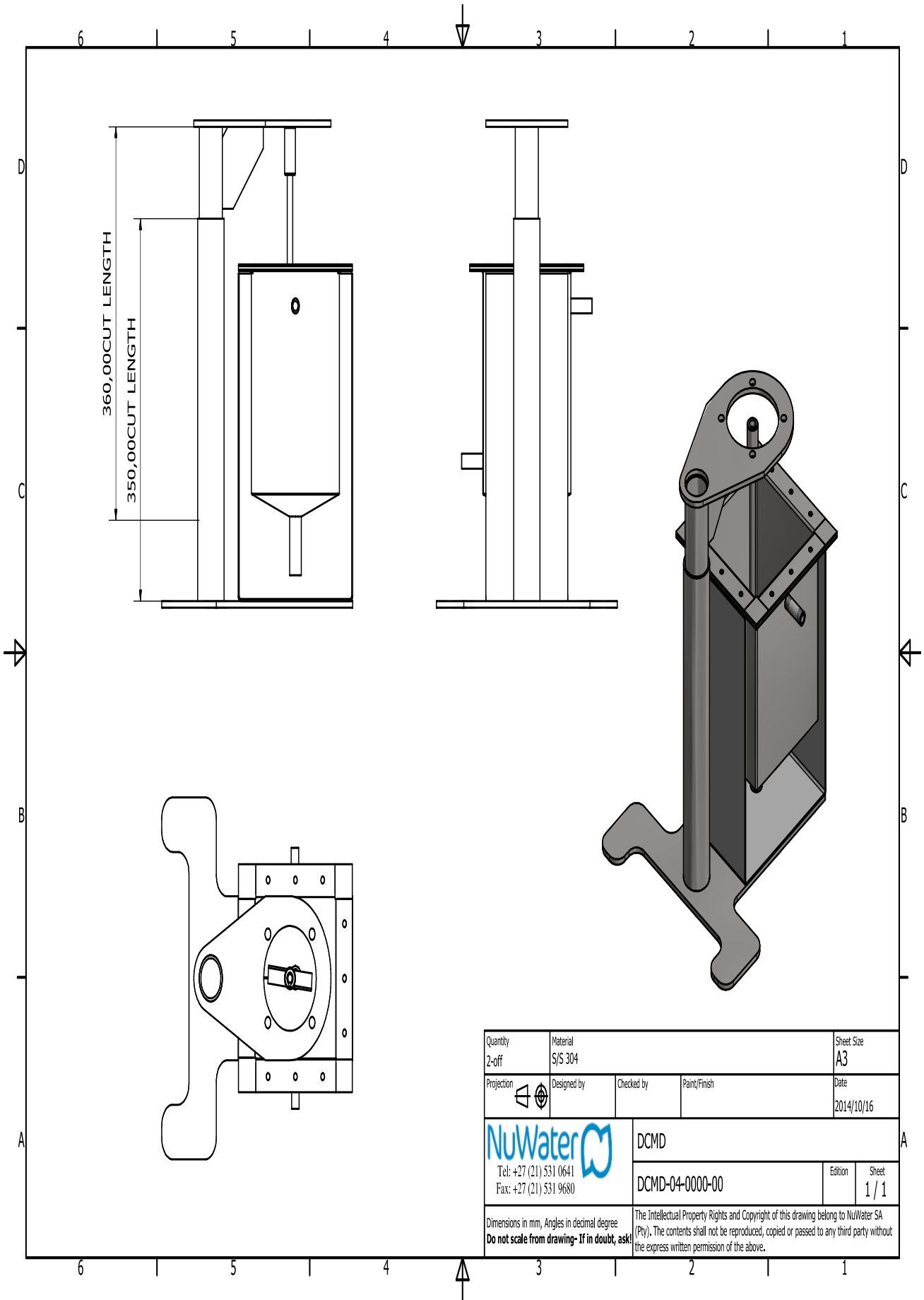
Quantity 1-OFF	Material SJS 304 40x40x2	Sheet Size A3	
Projection ⊕	Designed by Evert	Checked by	Paint/Finish
 Tel: +27 (21) 531 0641 Fax: +27 (21) 531 9680		DCMD-00-1000-02	Edition 01
Dimensions in mm, Angles in decimal degree <b>Do not scale from drawing- If in doubt, ask!</b>		Sheet 1 / 1	
The Intellectual Property Rights and Copyright of this drawing belong to NuWater SA (Pty). The contents shall not be reproduced, copied or passed to any third party without the express written permission of the above.			



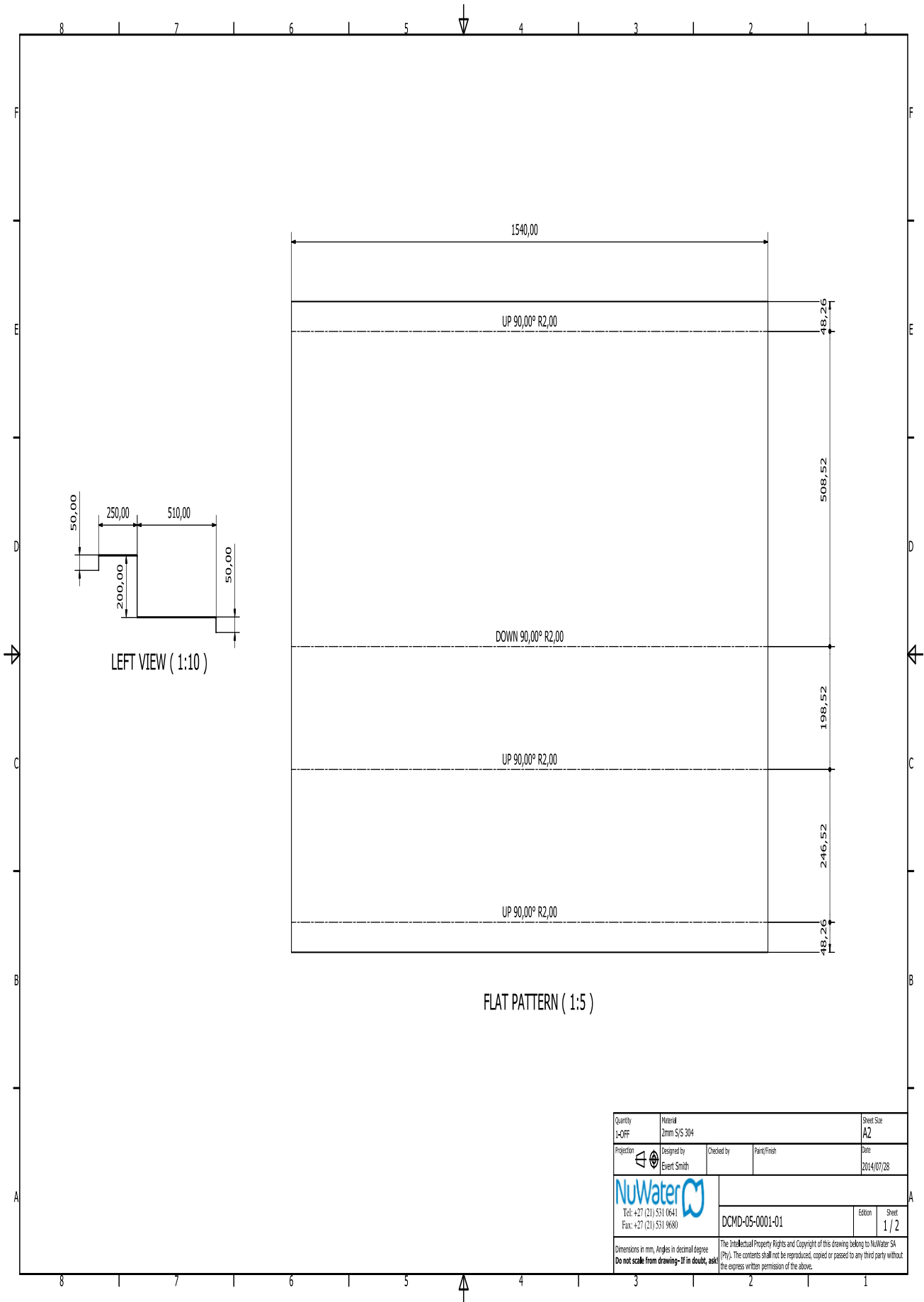
Designed by	Checked by	Approved by	Date	Date
EVERT				2014/04/02
<b>MEMBRANE HOLDER ASSEMBLY</b>				
DCMD-01-0001-00-1			Edition	Sheet
				1 / 1



Designed by EVERT	Checked by	Approved by	Date	Date 2014/04/02
MEMBRANE HOLDER ASSEMBLY			Edition	Sheet
			DCMD-01-0002-00	1 / 1




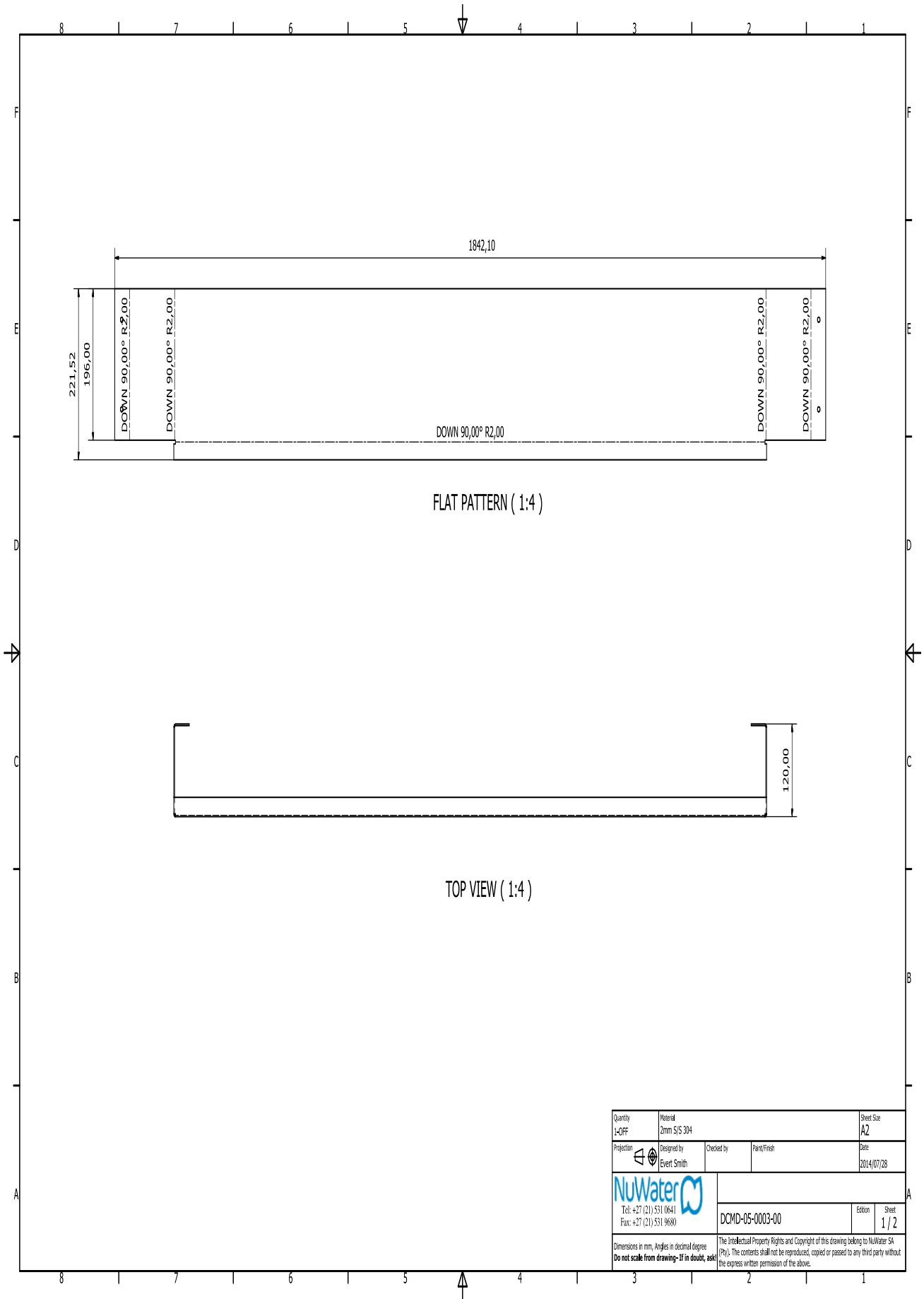




LEFT VIEW (1:10)


FLAT PATTERN (1:5)

Quantity 1-OFF	Material 2mm S/S 304		Sheet Size A2
Projection 1st Angle	Designed by Evert Smith	Checked by	Date 2014/07/28
 Tel: +27 (21) 531 0641 Fax: +27 (21) 531 9600		DCMD-05-0001-01	Edition 1 Sheet 1/2
Dimensions in mm, Angles in decimal degree <b>Do not scale from drawing- If in doubt, ask</b>		The Intellectual Property Rights and Copyright of this drawing belong to NuWater SA (Pty). The contents shall not be reproduced, copied or passed to any third party without the express written permission of the above.	

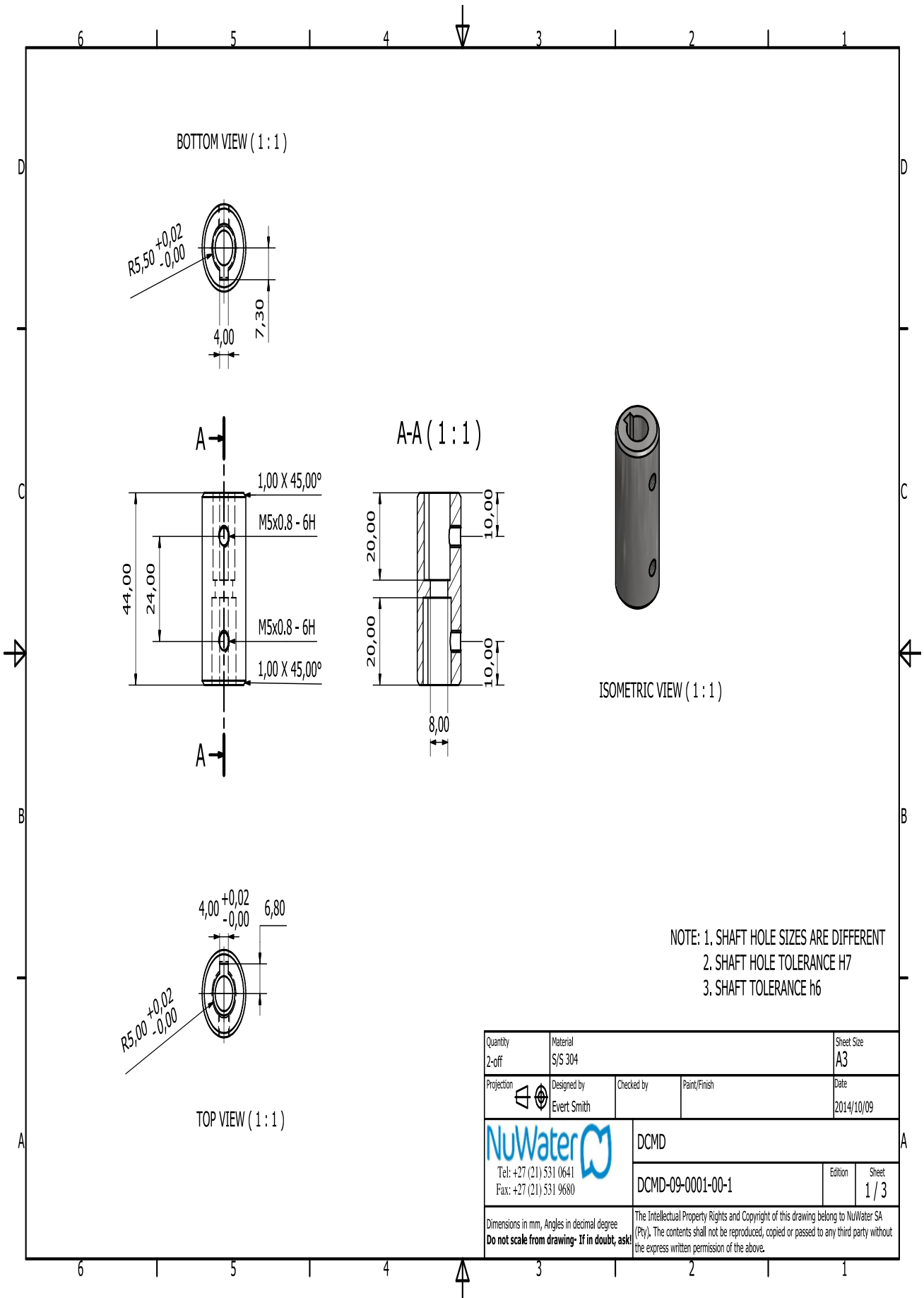


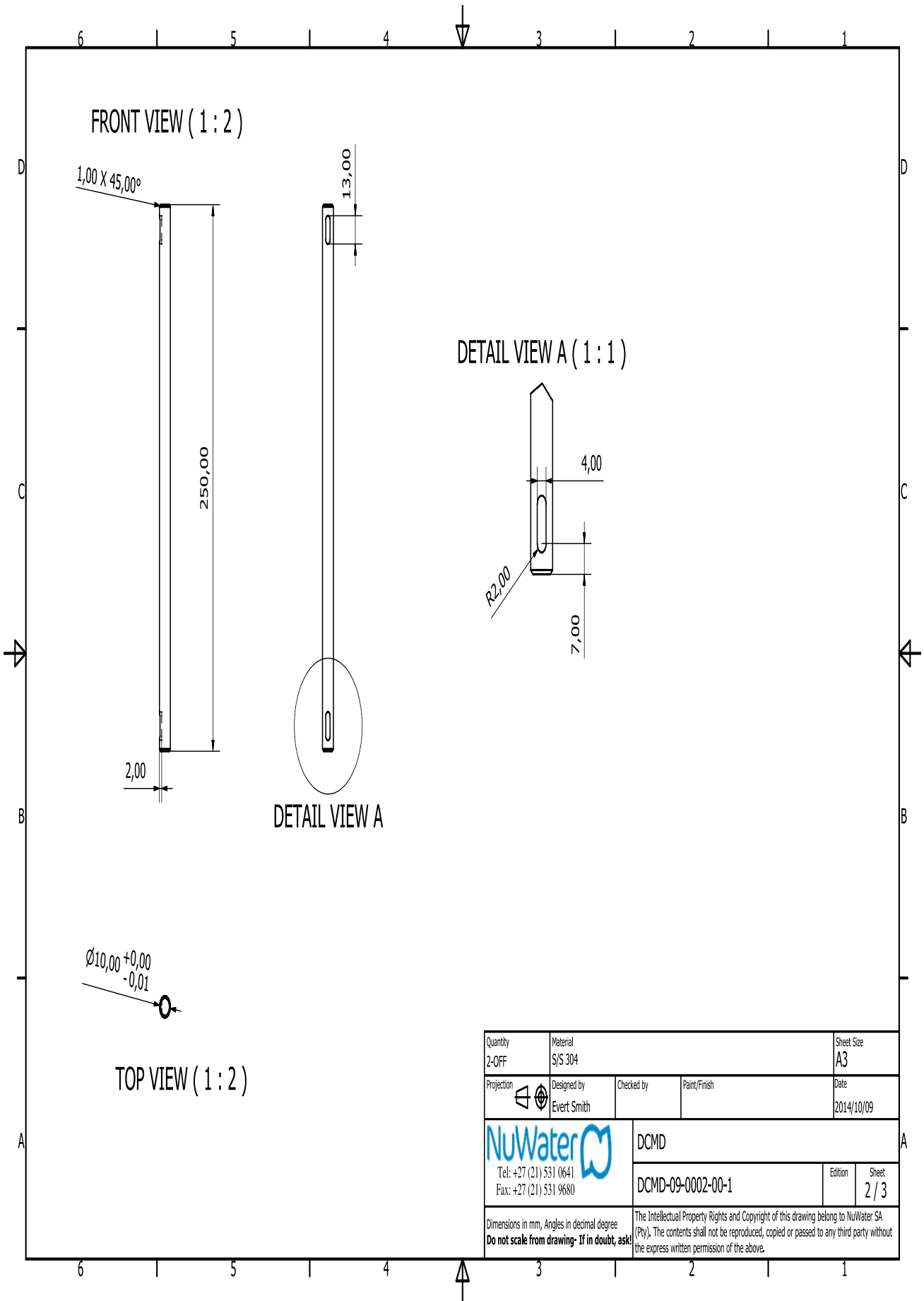
FLAT PATTERN ( 1:4 )



TOP VIEW ( 1:4 )

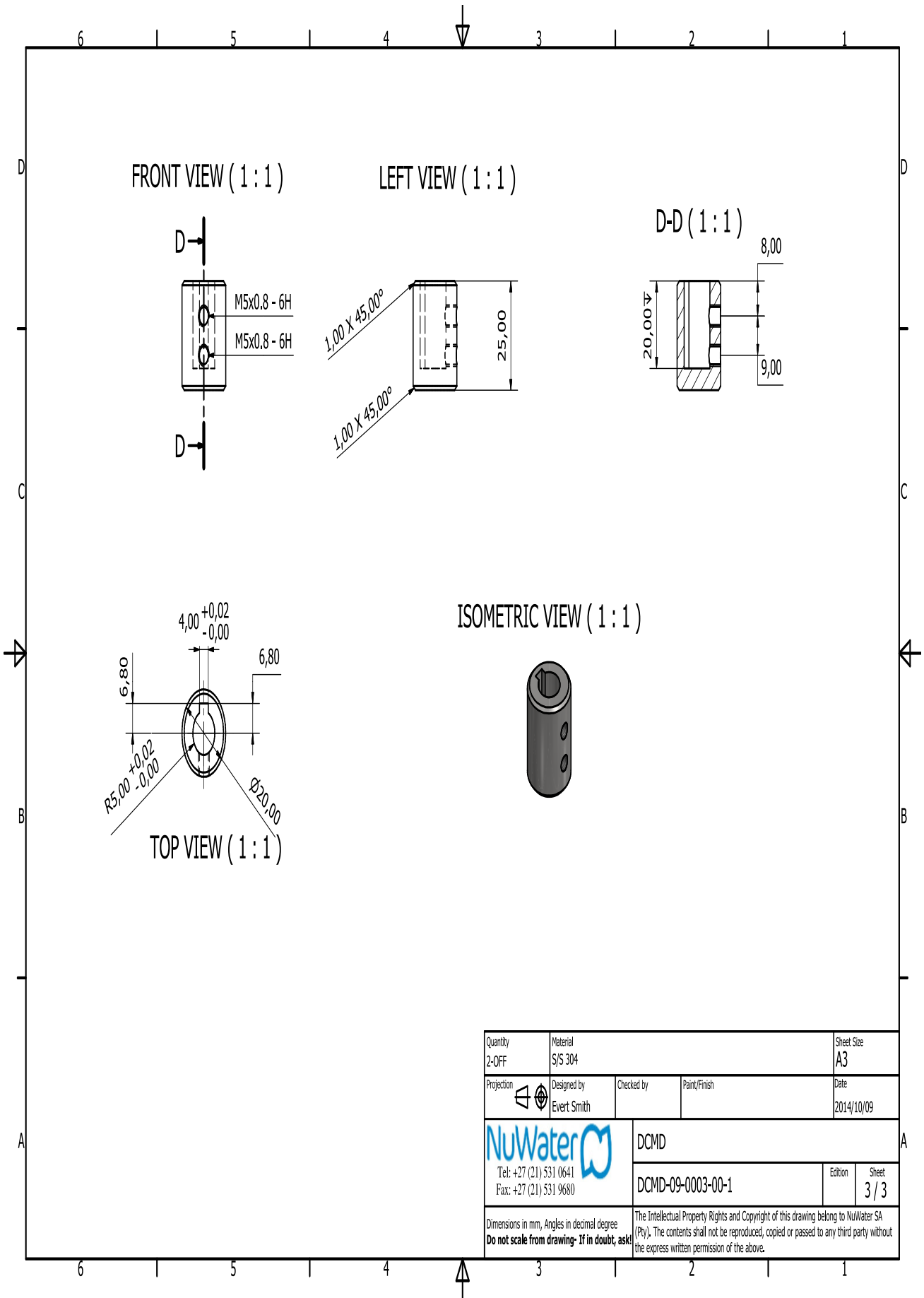
Quantity 1-OFF	Material 2mm S/S 304	Sheet Size A2	
Projection 1st Angle	Designed by Evert Smith	Checked by	Date 2014/07/28
 Tel: +27 (21) 531 0641 Fax: +27 (21) 531 9600		DCMD-05-0003-00	Edition 1 / 2 Sheet 1 / 2
Dimensions in mm, Angles in decimal degree. <b>Do not scale from drawing- If in doubt, ask</b>		The Intellectual Property Rights and Copyright of this drawing belong to NuWater SA (Pty). The contents shall not be reproduced, copied or passed to any third party without the express written permission of the above.	



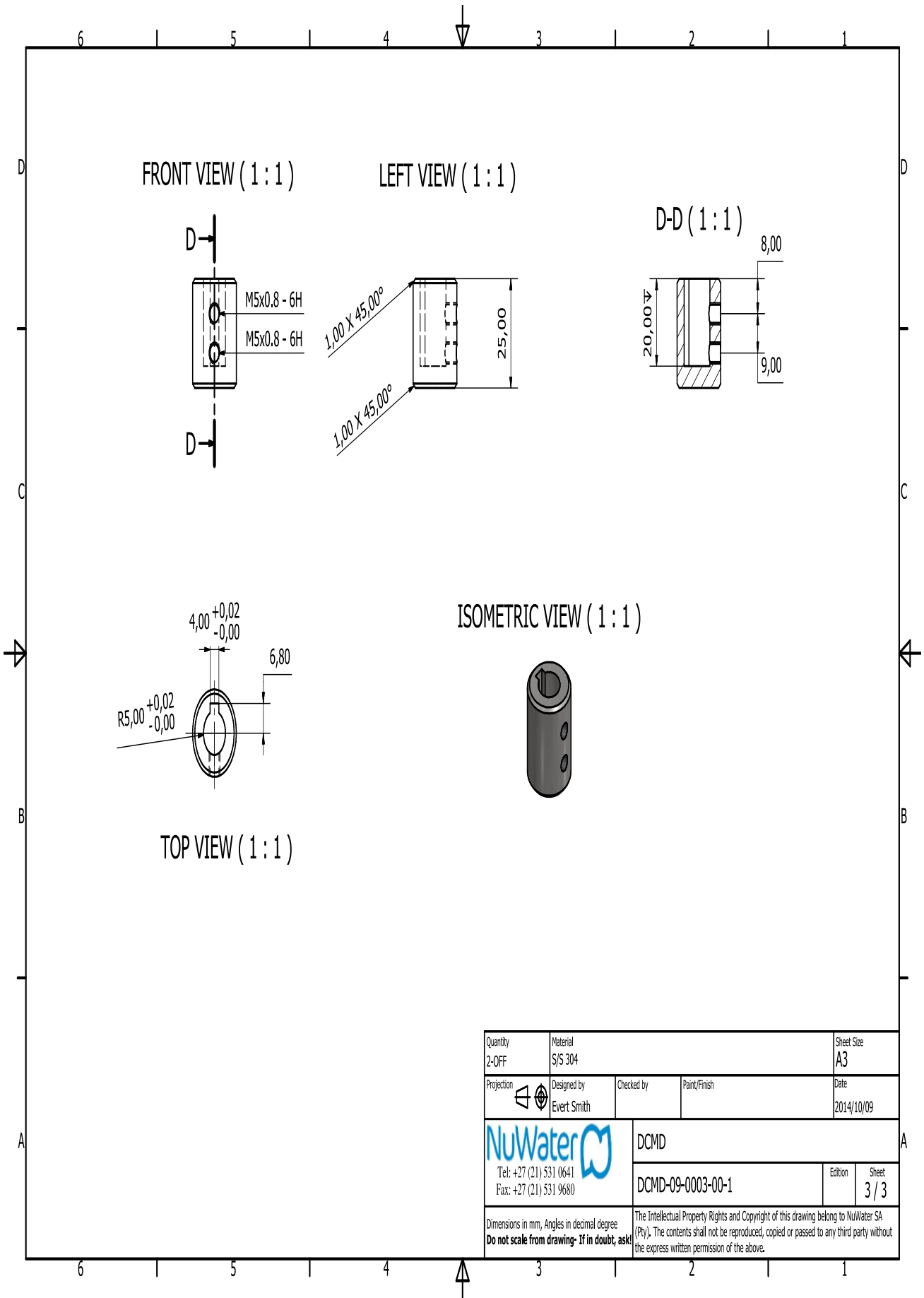




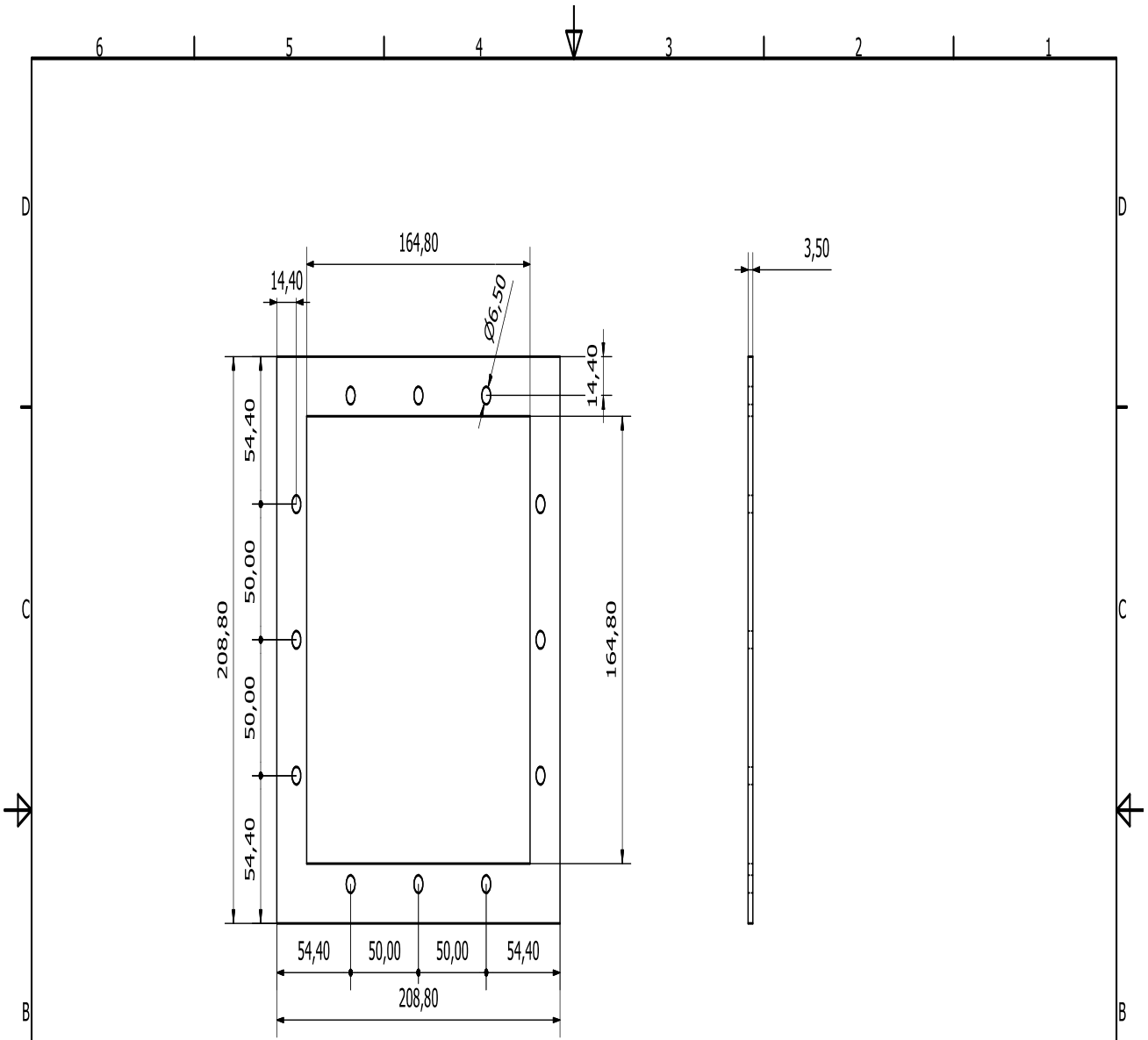
Quantity 2-OFF	Material SJS 304	Sheet Size A3	
Projection 	Designed by Evert Smith	Checked by	Paint/Finish
 Tel: +27 (21) 531 0641 Fax: +27 (21) 531 9680		DCMD	Date 2014/10/09
		DCMD-09-0002-00-1	Edition Sheet 2 / 3
Dimensions in mm, Angles in decimal degree <b>Do not scale from drawing- If in doubt, ask!</b>		The Intellectual Property Rights and Copyright of this drawing belong to NuWater SA (Pty). The contents shall not be reproduced, copied or passed to any third party without the express written permission of the above.	





Quantity 2-OFF	Material S/S 304	Sheet Size A3	
Projection 	Designed by Evert Smith	Checked by	Paint/Finish
 Tel: +27 (21) 531 0641 Fax: +27 (21) 531 9680		DCMD	Date 2014/10/09
Dimensions in mm, Angles in decimal degree <b>Do not scale from drawing- If in doubt, ask!</b>		DCMD-09-0003-00-1	Edition 3 / 3
The Intellectual Property Rights and Copyright of this drawing belong to NuWater SA (Pty). The contents shall not be reproduced, copied or passed to any third party without the express written permission of the above.			



Quantity 2-OFF	Material SJS 304	Sheet Size A3	
Projection 	Designed by Evert Smith	Checked by	Paint/Finish
 Tel: +27 (21) 531 0641 Fax: +27 (21) 531 9680		DCMD	Date 2014/10/09
DCMD-09-0003-00-1		Edition	Sheet 3 / 3
Dimensions in mm, Angles in decimal degree <b>Do not scale from drawing- If in doubt, ask</b>		The Intellectual Property Rights and Copyright of this drawing belong to NuWater SA (Pty). The contents shall not be reproduced, copied or passed to any third party without the express written permission of the above.	



TOP VIEW (1 : 2)

Quantity 2-OFF	Material 3.5mm Klinger gasket	Sheet Size A3	
Projection 	Designed by Evert Smith	Checked by	Paint/Finish
 Tel: +27 (21) 531 0641 Fax: +27 (21) 531 9680		DCMD Jacketed Tank Gasket	
Dimensions in mm, Angles in decimal degree <b>Do not scale from drawing- If in doubt, ask!</b>		Edition 001	Sheet 1 / 1
The Intellectual Property Rights and Copyright of this drawing belong to NuWater SA (Pty). The contents shall not be reproduced, copied or passed to any third party without the express written permission of the above.			



## APPENDIX C – Experimental data

